Universidad de Alcalá
Polytechnic School

DEGREE IN INDUSTRIAL ELECTRONICS
AND AUTOMATION ENGINEERING

Degree Final Project

Design and characterization of a solar concentration thermo-electric generator

Author: Francisco Salas Gómez
Supervisor: Efrén Díez Jiménez
Co-supervisor: Ignacio Valiente Blanco

September, 2021

UNIVERSIDAD DE ALCALÁ

POLYTECHNIC SCHOOL

Degree in Industrial Electronics and Automation Engineering

DEGREE FINAL PROJECT

"Design and characterization of a solar concentration thermo-electric generator"

Author: Francisco Salas Gómez

Supervisor: Efrén Díez Jiménez

Co-supervisor: Ignacio Valiente Blanco

EXAMINATION BOARD:

Chairperson: Pablo Díaz Villar

Assistant No.1: Roberto Gómez García

Assistant No.2: Efrén Díez Jiménez

GRADE: ….....

DATE: .....

A mis padres, Francisco y Ana,

porque todo lo bueno que pueda haber en mí
es mérito suyo.

Table of Contents

List of Figures

Chapter 1

Chapter 2

Chapter 3

Chapter 4

ANNEXES

List of Tables

Chapter 2

Chapter 3

Chapter 4

Chapter 5

ACKNOWLEDGEMENTS

Porque habéis hecho posible este trabajo y los que vendrán después, que estas líneas sirvan de agradecimiento.

A mi tutor, Ignacio Valiente Blanco. Tu confianza, tu experiencia, tu comprensión, y tu dedicación me han motivado para realizar este proyecto. Echo la vista atrás y sin duda este ha sido un año lleno de experiencias muy gratificantes. Y todo gracias a ti.
Gracias a Diego y a Efrén. Valoro mucho todos vuestros consejos, vuestro interés, vuestra disponibilidad, y el buen trato que me habéis brindado en estos meses.

Gracias a mi familia. Que me acompaña en cada paso que doy. Vuestro apoyo es incalculable, y vuestro amor, incondicional. Os quiero con todo mi ser.
Este viaje lo hemos recorrido juntos. No podía ser de otra forma.

Quiero concluir esta carta con un fragmento de la maravillosa *Elegía* de Miguel Hernández que dice así:

> *"Se me ha muerto como del rayo mi amigo Ramón Sijé,*
> *con quien tanto quería"*

En alguna ocasión he leído que la curiosa redacción de este fragmento se debió a un error y que nuestro ilustre poeta quiso decir «a quien tanto quería». Pero yo no estoy de acuerdo con esa interpretación.
Creo más bien que Miguel Hernández nos expresaba su admiración por alguien con quien compartió risas y tristezas, sueños y realidades, esperanzas y proyectos. Recordaba a un amigo y todo lo que había construido con él.

Lo que quiero decir es que mi paso por la Universidad de Alcalá es un inolvidable periodo de aprendizaje, pero no lo he vivido solo.
La casualidad quiso que fuera a una despedida en Azuqueca de Henares allá por 2018, que asistiera a un evento de la escuela de emprendimiento, o que comenzara en el debate académico. La casualidad quiso que entrara a un grupo de amigos muy reales que han convertido mi vida universitaria en un viaje que no te quieres perder.
Soy afortunado por haber conocido a tantas personas que admiro.

Con quienes tanto quiero.

A todos y cada uno de vosotros,
Muchas gracias

Francisco Salas Gómez
Alcalá de Henares, 2021

ABSTRACT

This project presents the design and evaluation of a solar concentration thermoelectric generator(TEG) for harvesting energy directly from solar radiation.

With the aim of assessing the improved performance obtained by the concentration system, a test campaign at different irradiances and environmental conditions has been carried out. Additionally, results are compared to a larger TEG without the mentioned concentration mechanism. The maximum power generation was 1.6mW at 1050W/m^2, 4 times the production of the non-concentrating TEG.

Finally, scalability analysis is carried out in order to assess the feasibility of supplying auxiliary equipment in photovoltaic energy harvesting farms.

RESUMEN

Este proyecto aborda el diseño de un generador termoeléctrico de concentración solar para la conversión directa de radiación solar en electricidad.

El sistema se ha sometido a una serie de ensayos a diferentes irradiancias y condiciones exteriores para evaluar las mejoras del concentrador. Además, su desempeño se compara con un TEG más grande sin el mencionado mecanismo de concentración. La generación máxima alcanzada es de 1,6mW a 1050W/m^2, cuatro veces la producción del prototipo sin concentrador.

Finalmente, se realiza un análisis de escalabilidad para evaluar la viabilidad del prototipo para suministrar equipos auxiliares en campos de energía fotovoltaica.

KEYWORDS

Thermoelectric generator, Seebeck effect, Fresnel lens, Energy harvesting, DC-DC Converter

SUMMARY

This project addresses the design and experimental evaluation of a low-power electrical supply based on thermoelectric devices and a solar concentration mechanism as passive heat source.

The developed system consists of a thermoelectric generator module that delivers electrical power based on the so-called Seebeck effect, and an optical concentration mechanism named Fresnel lens.
The overall dimensions of the concentrating TEG system are 60x60 mm^2. A cylindrical Fresnel lens of 50.8 mm in diameter is used and a TEG cell with a 11.2x11.2 mm^2 surface. The prototype is equipped with a 3DOF positioning mechanism which enhances the input radiation from the sun. In order to improve heat evacuation on the TEG module, a commercial heat sink is also integrated in the prototype. The DC-DC power converter is designed with an optimized input impedance, similar to the matched-load of the TEG module, which maximizes the power output of the system. The electronic system is also responsible of stabilizing the power output and not dependent on the output power oscillations generated by the TEG. Finally, the power generated is stored in a battery for a later use in other systems.
The following figure shows a scheme of the whole system:

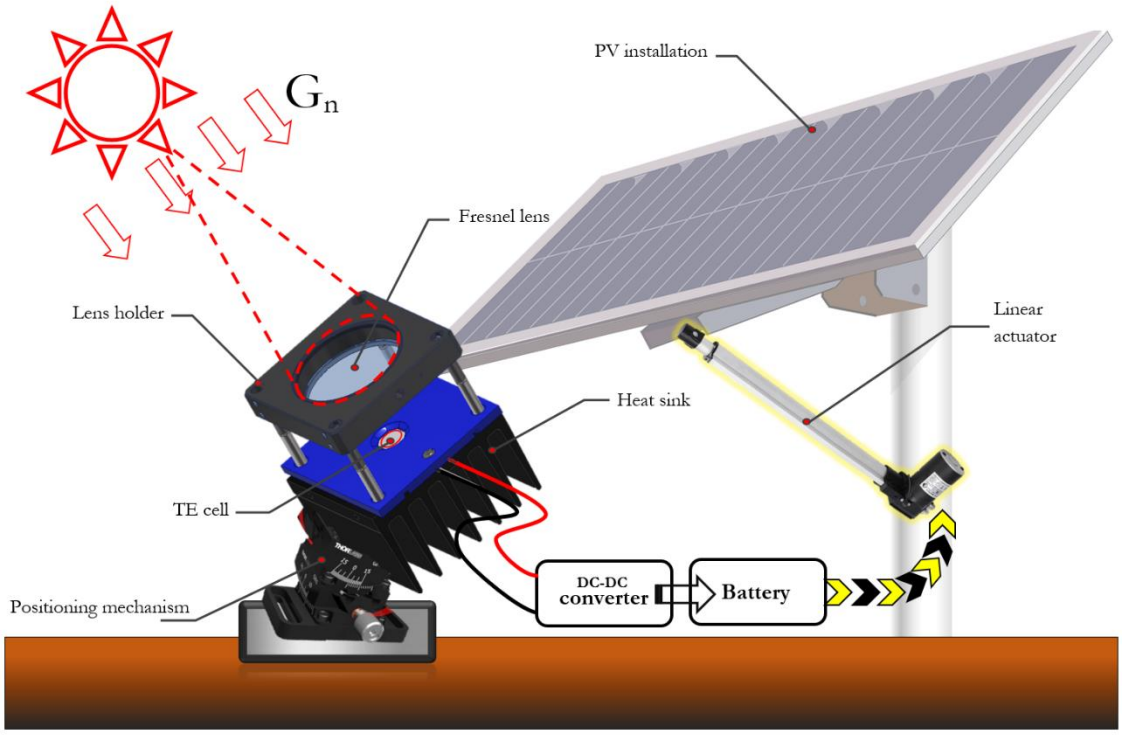

The justification for the use of an optical concentration system lies in the fact that in TEG-only solar systems a low temperature gradient is generated, even in the summer season.

In order to maximize the power generation and efficiency of a TEG, a larger temperature gradient would be desired.
This increase in the temperature gradient is obtained by concentrating the solar radiation in a smaller TEG. This approach presents three major advantages: firstly, the efficiency and power generation of the TEG are boosted due to the larger temperature gradient. Secondly, more heat is available in the TEG for energy harvesting, since heat convection losses are reduced due to the lower TEG exposed area to the environment. Finally, the lower size of the TEG would reduce the cost of the overall system, since TEG materials are frequently the costliest part of the design.

In order to evaluate the performance of the concentrating TEG, two set of test campaigns were conducted under controlled laboratory conditions and at outdoor actual conditions.

In a first stage, the performance of the TEG modules that will be used in the outdoor tests is investigated at different environmental and operational conditions. A heat isolated housing is design and manufactured for this evaluation.
After that, and thanks to the knowledge obtained, a concentrating TEG prototype is designed and manufactured. Two Fresnel lenses with different focal lengths (f=32mm and 51mm) were investigated. The former lens brought a power output less sensitive to the angle misalignment referred to the sun position. The latter offered a 35.8% higher peak output power when exposed perpendicularly to the sun (no angle misalignment). In order to maximize the power generation, the lens of f=51mm was selected.

Such prototype is iteratively improved for maximizing power generation. Firstly, by applying a thin black paint cover on the exposed surface of the TEG. An improvement in a factor about 15 in the power generation is observed. Secondly, by protecting the exposed surface from the wind, power generation can be also improved up to a 30%.

A final prototype is tested in outdoor conditions in July 2021 in Alcalá de Henares, Spain. The maximum power output observed is 1.634 mW for a sun irradiance level of 1050 W/m^2.
When comparing the power generation of the concentrating TEG prototype with a non-concentrating TEG with an envelope of 62x62 mm^2, it was observed that power generation can be improved by a factor about 4, depending on the sun irradiance.

The scalability of the developed system and its compatibility with other heat sources favours its development as power supply for auxiliary systems at a photovoltaic installation.

NOMENCLATURE

Acronyms

CPC	Compound Parabolic Concentrator
CPV	Concentration Photovoltaic System
DAQ	Data Acquisition System
DC	Direct Current
DOF	Degrees of Freedom
LTG	Low Temperature Gradient
MPP	Maximum Power Point
MPPT	Maximum Power Point Tracking
CPV	Concentrated Photovoltaic
PV	Photovoltaic
PWM	Pulse Width Modulation
SC	Solar Concentration Mechanism
STC	Standard Testing Condition
TE	Thermoelectric
TEG	Thermoelectric Generator

Subscripts

c	Cold side of the TEG
cond	Conduction Heat
conv	Convection Heat
F	Fresnel lens
h	Hot side of the TEG
heatsink	Heatsink
in	Incoming direction to the TEG
j	Thermal junction
J	Joule Effect
load	Electrical load
max	Maximum value
min	Minimum value
n	N-type semiconductor

OC	Open Circuit
off	Open switch
on	Closed switch
out	Outgoing direction from the TEG
p	P-type semiconductor
rad	Radiant heat
S	Sun / Solar
sw	Switching
T	Solar tracker
TEG	Thermoelectric Generator

Superscripts

11.2x11.2	TE module MGM250-17-10-16
62x62	TE module GM200-49-45-25

Symbols		Unit
A	Surface	$[\,\mathrm{m}^2]$
C	Concentration ratio	[suns]
D	Duty cycle	
f	Focal length	$[\,\mathrm{mm}\,]$
G	Solar irradiance	$[\mathrm{W/m}^2]$
h	Thermal convection coefficient	$[\mathrm{W/m}^2 \cdot \mathrm{K}]$
K	Thermal conductance coefficient	$[\mathrm{W/m}^2 \cdot \mathrm{K}]$
L	Distance between the TE cell plates	[m]
q	Heat flux	$[\mathrm{W/m}^2]$
Q	Transferred heat	[W]
r	Electrical internal resistance	[Ω]
R	Electrical resistance	[Ω]
	or Thermal resistance	[K/W]
S	Cartesian reference system	
t	Time	$[\,\mathrm{s}\,]$
T	Absolute temperature	$[\,\mathrm{K}\,]$
ZT	Thermoelectric Figure of Merit	

Greek symbols

α	Seebeck coefficient or spectral absorption component	$[\mu V/K]$
β	Elevation angle above the horizon	$[\text{degrees}]$
γ	Azimuth angle	$[\text{degrees}]$
ϵ	TEG matched ratio or Emissivity	
η	Efficiency	
θ	Incident angle	$[\text{degrees}]$
	Tracking rotation angle	$[\text{degrees}]$
κ	Thermal conductivity	$[W/m \cdot K]$
λ	Wavelength	$[m]$
ρ	Electrical resistivity	$[\Omega \cdot m]$
σ	Electrical conductivity	$[S/m]$
	or Stefan-Boltzmann constant	$[W/m^2 \cdot K^4]$

PREFACE

Chapter 1 introduces the thesis statement and the objectives pursued in this project.

Chapter 2 deals with the state-of-the-art of concentration mechanisms, and covers the theoretical basics of thermoelectric technology. In addition, power converters and PV installations are introduced. Finally, a brief study of the patents related to the project is carried out.

Chapter 3 addresses the design of the solar concentration TEG system and develops an improved second prototype. For the simulation of the TEG module, a program is created in MATLAB App Builder. The power converter is selected and assembled, and a battery stage is designed. Finally, the data acquisition systems for both the laboratory and outdoor tests are created.

Chapter 4 covers the assembly of the setups for the laboratory tests and outdoor tests. The obtained results from all the experiments are discussed from a practical application-oriented perspective, analyzing the feasibility of the implementation of the proposed system.

Chapter 5 quantifies the budget of the project, taken into account manpower, goods, and software expenses.

Chapter 6 summarizes the development of the project and proposes the future venues of research.

REPORT

Chapter 1

Introduction and Objectives

You never get a second chance
to make a first impression.

Oscar Wilde

1.1. Introduction

One of the greatest challenges of our society is coping with the increasing worldwide energy demand. Nowadays, most of the energy generated at global scale comes from fossil fuels. The environmental impact associated with their use, and the fact that the reserve of fossil fuels is limited, have brought into sharp focus the necessity of developing alternative energy sources [1]–[3].

In this scenario, solar energy stands out for being a renewable, abundant, and inexpensive source that is set to be the solution for reducing fossil fuels dependency [4]. Concentrated solar irradiation as a passive heat source has led to the development in this field of another promising yet still low efficient technology: the thermoelectric devices.

Currently, the main problem of available TEG systems is the low efficiency in the energy harvesting from a heat source, which rarely exceeds 5%. Heat losses due to heat convection and heat radiation play a relevant role. It has to be mentioned that in all TEG systems, the higher the temperature gradient between the hot and cold interfaces, the higher the output generation [5].

This project addresses the design and empirical evaluation of a low-power supply based on thermoelectric devices. For improving the overall performance of the TEG module, a solar concentration mechanism is incorporated into the system.

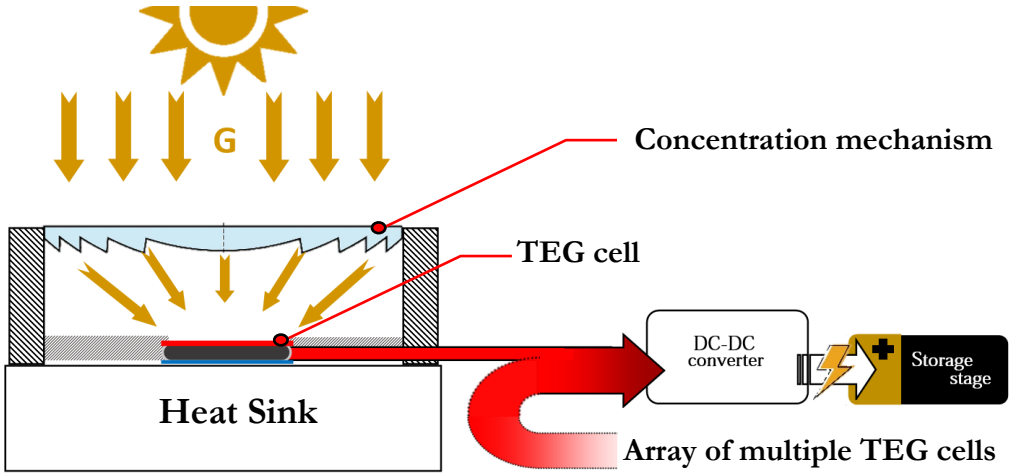

Figure 1.1 Diagram of the TEG-based system developed in this project

The design of a hybrid system comprised of thermoelectric generators and concentration structures can potentially overcome the problem of thermal losses at the same time as it directly harvests solar the energy in a more efficient way thanks to the improved temperature gradient. To demonstrate this hypothesis, both systems (TEG+SC and TEG-only) are assembled and tested in the same conditions.

Firstly, this project addresses the design of the system from scratch, starting with the selection of the components, the preliminary design of an outdoor prototype, and the design of the power converter stage in order to supply a continuous and stable voltage at a desired level.
Secondly, the design is tested, firstly, under laboratory-controlled conditions and then tested outdoor. By doing so, the performance of the system is characterized and the feasibility of its practical application in photovoltaic installations is studied.

Figure 1.2 Solar concentration TEG at the facility of SolarG project

Figure 1.2 shows the outdoor installation of SolarG, a research project regarding the design of a geothermal cooling system for PV modules. The developed system will be evaluated in these installations and the feasibility of powering auxiliary devices of the PV panel is analyzed.

1.2. Objectives

The aim of this project is to design an optimized autonomous power supply system, based on a concentrating thermoelectric generator, that directly harvests energy from solar irradiation.

In order to maximize the power generation, a sun concentration mechanism based on a Fresnel lens will be used to increase the temperature gradient through the TEG and minimize heat losses and, therefore, optimize the power generation.

The aim outlined above compounds the following specific objectives:

- To design, optimize, and experimentally evaluate a solar concentration thermoelectric generator.

- To demonstrate the improvement of a concentrating TEG compared to a non-concentrating TEG operating in similar conditions.

- To design, implement, and evaluate the power electronics suitable for the thermoelectric generator to optimally manage the electricity generated.

  This power supply will be provided with the following characteristics:
  1. Continuous and stable output voltage at a desired level.
  2. Storing of the energy in a battery for supplying auxiliary systems.

- To evaluate the feasibility of using the TEG concentration mechanism as a potential power source of auxiliary equipment in typical photovoltaic energy production facilities.

The tasks, milestones, deadlines, and workflow of the project are registered in ANNEX IX Gant chart of the project.

Chapter 2

Analysis of the State-of-the-Art

The limits of my language
mean the limits of my world.

Ludwig Wittgenstein

The sun is a potential clean energy source that can be harnessed through three primary technologies [6].

- Solar thermal systems (ST). These systems collect thermal energy for providing a hot source for thermodynamic systems.

- Photovoltaic systems (PV). The electrons of a PV cell capture the photons of the incident light. As a result, these electrons are induced to travel through an electrical circuit and powering the grid.

- Concentration systems (SC). This technology uses optical devices and mirrors for directing the light from the sun and driving other devices.

a) ST system for heating water

b) PV cell

c) Heliostat field

Figure 2.1 Solar energy harvesting technologies

Hybrid combinations among these technologies do exist. In fact, the hybridization of these technologies allows to improve the overall efficiency of a solar system.

2.1. Sun concentration mechanisms

The objective of sun concentration mechanisms is focusing the received light onto a receptor and their performance is measured with the concentration ratio C_S[suns].

$$C_S = \frac{\text{Concentrator irradiance}[W/m^2]}{\text{Receptorirradiance}[W/m^2]} \quad \textbf{(2.1)}$$

Depending on the concentration ratio, the different mechanisms might be classified as [7]:

- Ultra-High concentrations (>2000 suns)
- High concentration (100 ~ 2000 suns)
- Medium concentration (10 ~ 100 suns)
- Low concentration (<10 suns)

Notwithstanding, a higher concentration ratio means a higher impact of reflection on the mechanism. The Snell law of refraction dictates the path of a ray from a medium of refractive index n_1 to a medium of refractive index n_2 is described as: [8]:

$$n_1 \sin\theta_1 = n_2 \sin\theta_2 \quad \textbf{(2.2)}$$

Where θ_1[rad] is the incidence angle of the ray and θ_2[rad] is the angle of refraction.

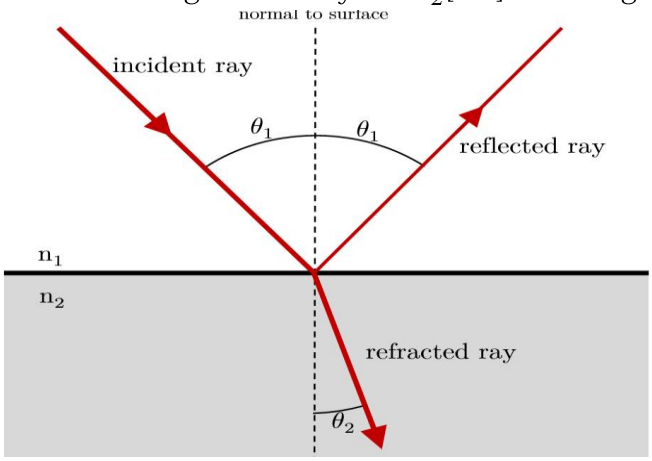

Figure 2.2 Law of refraction

High concentration mechanisms have a large refracted angle, and so, the incidence angle takes a high value too. For avoiding the scattering of light, the surface of both the reflective and the refractive surfaces must be smooth.

Nonetheless, light is always partially or fully refracted, reflected or absorbed when travelling from one medium to another [8].

The main applications of solar concentration mechanisms regard photovoltaic systems (CPV) and thermal solar systems.
Conventional PV modules use a flat concentrator that minimizes the reflection of the solar radiation as it passes through the glass. The rear and side areas of the concentrator are well insulated from the external environment to reduce conduction losses.

In addition, some CPV systems allow to replace solar cells with optical mechanisms that focus the light onto smaller cells, whereas in conventional photovoltaic systems the collection of solar energy and its conversion to electricity is performed by the solar cell itself.

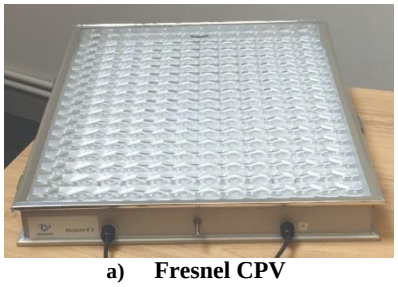

a) **Fresnel CPV**

b) **Spherical High CPV**

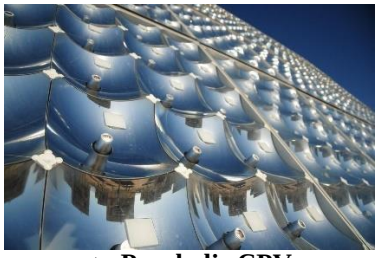

c) **Parabolic CPV**

Figure 2.3 CPV technologies

Different tracking techniques can be chosen depending on the desirable concentration. This concentration ratio limit is imposed by the divergence of light from the Sun [7]:

- Static concentration. Concentration ratio is around 2 suns.
- Single-axis tracking. Concentration ratio achievable of around 200 suns.
- Two-axis tracking. Concentration ratio over 2000 suns.

The CPV system typically includes a cooling system for the thermal management of solar receivers due to the fact that heating up the cells provokes a reduction in their efficiency [9].
On the other hand, the purpose of solar thermal concentrators is to increase the temperature of a thermal load. According to the thermal load, that can be classified as [10], [11]:

- Low temperature collectors (<80ºC)
  They consist of flat plates. Uses: residential use, heating water, etc ...
- Medium-temperature collectors (80ºC ~ 250ºC)
  They consist of flat plates. Uses: heating air or water for commercial and residential use.
- High-temperature collectors (>250ºC)
  They concentrate sunlight by using lenses or mirrors. Uses: Electric power production (e.g. heliostat fields).

When it comes to concentration mechanisms, there is a wide range of alternatives. For instance, the Compound parabolic concentrator (CPC) [7], the Fresnel lens[7], the parabolic dish concentrator [12], hyperbolic concentrator [13], parabolic trough concentrator [14], RX concentrator [15], and RXI concentrator [15].

Compound parabolic concentrator (CPC)

This mechanism consist of two symmetrical parabolic reflecting surfaces. The first reflector surface directs the light onto a second reflector located in the opposite end of the mechanism. Beneath this second reflector there is a homogeniser that conveys the light beam onto the desired spot.

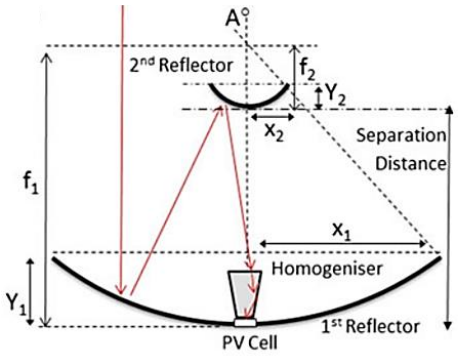

Figure 2.4 Compound parabolic concentrator

Collector concentrators only use direct radiation and not diffuse radiation. For further information regarding the components of the global solar radiation. Furthermore, the material of the concentrator may lose its reflection properties over time and requires periodic maintenance.

Fresnel lenses

Fresnel lenses have their origins in the lighthouses of the 19th century. Instead of concave or convex lenses, its design divides its flat surface into a set of concentric annular sections of different thickness and orientation.

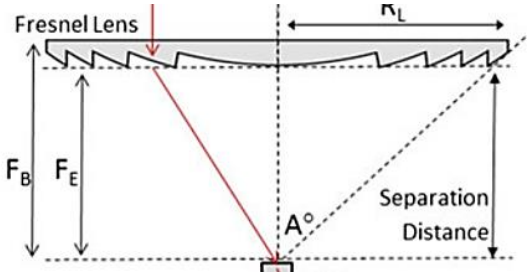

Figure 2.5 Fresnel lens concentrator

The main advantages of Fresnel lenses are their light weight and the low material needed for its manufacture. The downside of Fresnel lenses are the lower optical efficiency

compared to the CPC because of reflection and aberrations problems, the focal length is not stable, and the material is easily scratched and prone to aging [16].

All lenses share a relevant parameter that is discussed in this thesis: the focal length f [mm].

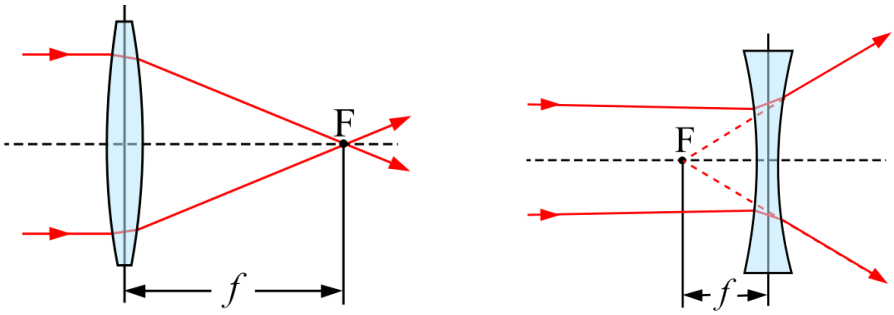

a) Convex lens **b) Concave lens**

Figure 2.6 Focal length

The focal length of a lens is the distance between the optical centre of the lens and the focal point F. For a convex lens (Figure 2.6a), the light converges and the focal length is positive. For a concave lens (Figure 2.6b), the light diverges and the focal length is negative [17]. Fresnel lens is a flat lens but the shape of its grooves emulates the effect of a converging lens.

2.1.1. Diffuse solar irradiation

Diffuse irradiation is the phenomenon generated in the atmosphere when solar radiation reaches its surface. As a result, about 25% of the incident radiation is scattered from its original direction by the molecules present in the atmosphere. Moreover, only two-thirds of the scattered radiation reaches the earth as diffuse radiation. The diffuse irradiation has four components [18]:

- the circumsolar diffuse irradiation.
- the isotropic diffuse irradiation.
- the horizon diffuse irradiation.
- the ground reflected irradiation or albedo

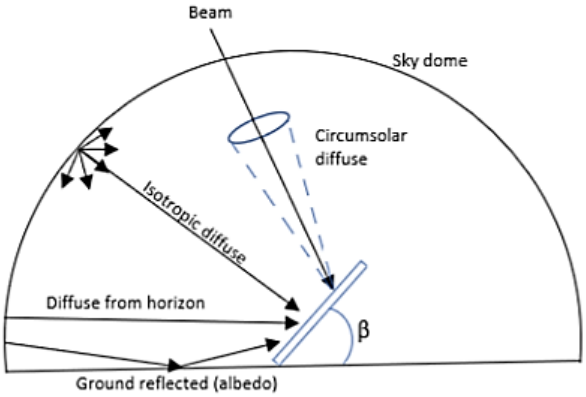

Figure 2.7 Solar irradiation components [18]

The SI unit of irradiance is W/m^2. The solar energy industry uses Wh/m^2. Their relation is:

$$1[\mathrm{kW/m^2}] \times 24[\mathrm{h/day}] = 24[\mathrm{kWh/m^2}] \quad \textbf{(2.3)}$$

$$24[\mathrm{kWh/m^2}] \times 365[\mathrm{days/year}] = 8{,}760[\mathrm{kWh/m^2/year}] \quad \textbf{(2.4)}$$

Concentrated solar irradiation as a passive heat source has led the SC systems to its hybridization with another promising yet still low efficient technology: the thermoelectric devices.

2.2. Seebeck effect and thermoelectric generators (TEGs)

Thermoelectric conversion is defined as the process by which heat is converted into electricity, and vice versa. There exist three different effects that belong to the thermoelectric conversion [19]–[22]:

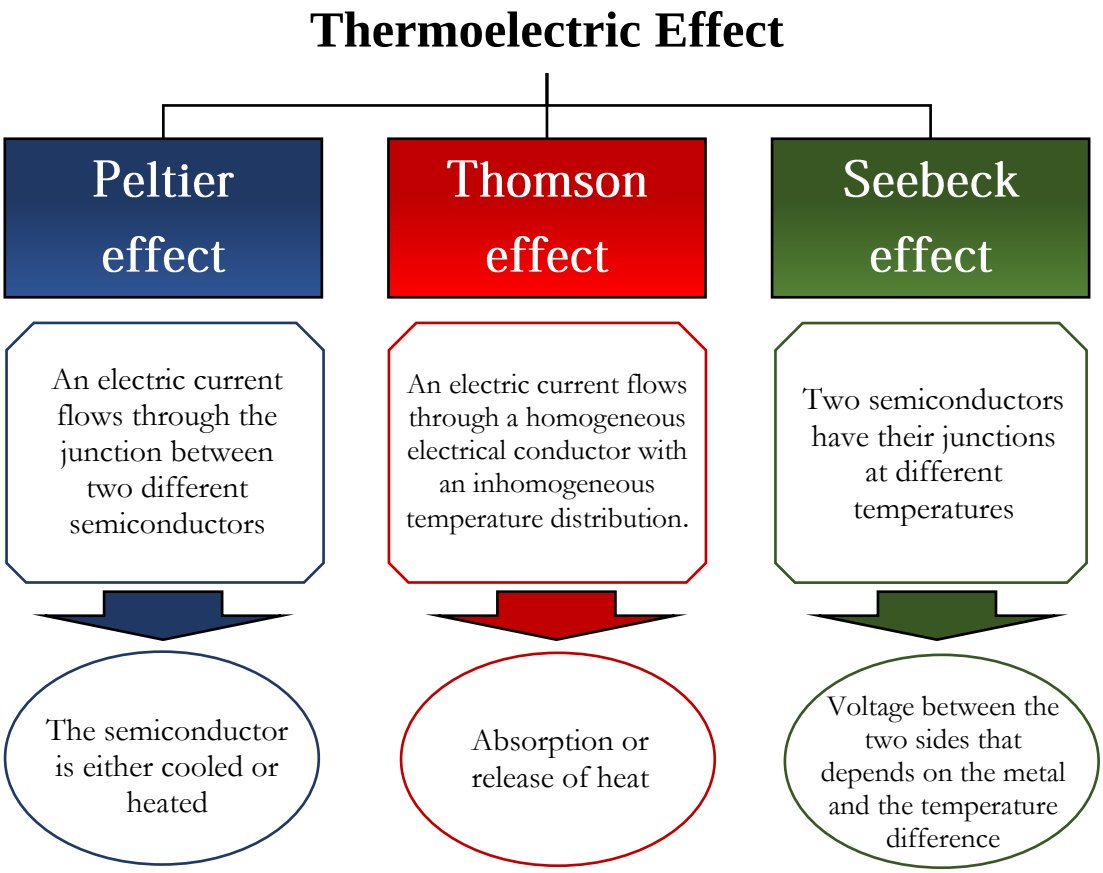

Thomson relations

There are three thermoelectric coefficients (Thomson, Peltier, and Seebeck). All of them are mutually related as follows [23]:

$$\mathcal{K} = \frac{d\Pi}{dT} = -\alpha \qquad \textbf{(2.5)}$$

Where $\mathcal{K}$ is the Thomson coefficient, Π is the Peltier coefficient, T is the absolute temperature, and α is the Seebeck coefficient.

This relation expresses that Thomson effect is the continuous application over temperature of the Peltier effect. Secondly:

$$\Pi = \mathrm{T} \cdot \alpha \tag{2.6}$$

The second equation of Thomson relations highlights the fact that there is a direct connection between the Seebeck and Peltier effects. However, this equation is not valid if the material in question is either magnetic or is placed in a magnetic field.

From (2.5) and (2.6):

$$\mathcal{K} = \mathrm{T}\,\frac{\mathrm{d}\alpha}{\mathrm{dT}} \tag{2.7}$$

Thomson coefficient can be directly measured from a material in contrast to the Peltier and Seebeck coefficients hence the Thomson relations plays a preponderant role when it comes to determine the thermoelectric coefficients of the materials.

This report addresses the Seebeck effect in more detail, as it is the principle behind the thermoelectric power generation [22].

2.2.1. The Seebeck effect

The Seebeck effect is the generation of an electric voltage between two semiconductors subjected to a temperature gradient. As a result of this temperature gradient, the charge carriers of the semiconductor have more kinetic energy, hence they travel from the heated region towards the cold region (Hole flow).

The cold side of the p-type leg is positively charged, and so, a migration of electrons in the n-type leg is produced. Eventually, one of the sides will have a higher charge carriers concentration (electrons in the case of n-type semiconductor and holes in the p-type). The semiconductor will therefore be electrically charged [22], [24].

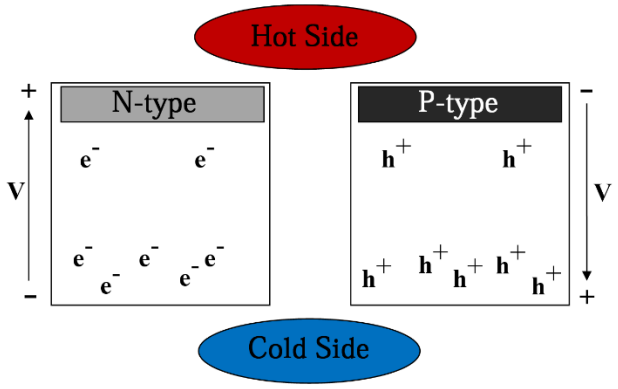

Figure 2.8 Charge carriers displacement under Seebeck Effect

If there is no load connected to the joints of the semiconductor, the thermocouple is in open circuit:

$$V_{OC} = \alpha \Delta T \quad \textbf{(2.8)}$$

Where α [μV/K] stands for the Seebeck coefficient and ΔT (K) is the thermal gradient between the hot side and the cold side of the thermocouple. The Seebeck coefficient can be either positive or negative depending on the charge carriers and the material type.

2.2.2. Thermoelectric Generators (TEGs)

The Thermoelectric (TE) energy harvester is a solid-state device. When an incoming heat is converted into an output electric power, this device works as a generator (TEG) based on the previously mentioned Seebeck effect.

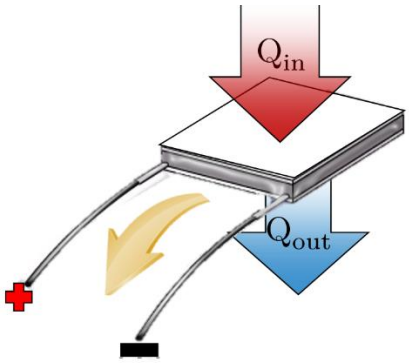

Figure 2.9 Thermoelectric generator - energy harvesting

However, TEG modules have a low conversion efficiency (around 3%~ 5%) and they require relatively large temperature gradients to operate efficiently. Hence optimising the heat flux is crucial for improving the power generation [25].

A TEG cell consists of semiconductor thermocouples connected thermally in parallel and electrically in series. This circuit is housed between two thermally conductive plates.

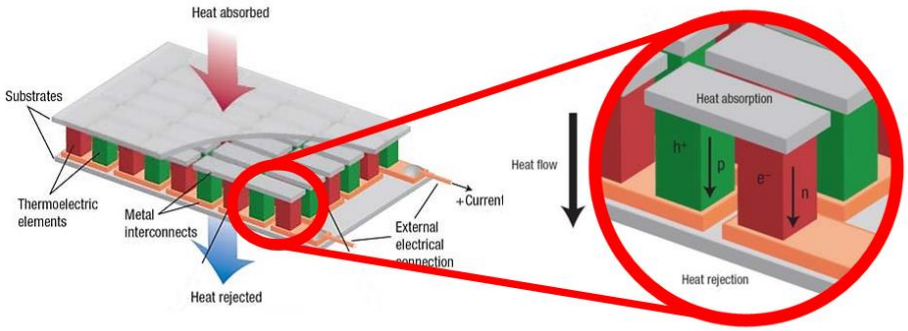

Figure 2.10 Overview of the semiconductor connection in a TE module

The TEG technology has multiple advantages. For instance TEG devices have a long lifetime, small dimensions, are easily scalable, non-polluting, silent, and require low maintenance. Among the main drawbacks, it can be mentioned its low efficiency, the output power is not constant, and relatively high costs. Nevertheless, the advantages make the TEGs an attractive solution for both domestic and industrial applications.

Thermal analysis of a TEG

First and foremost, some theoretical basics regarding thermal engineering are introduced. There are three principal mechanisms of heat transfer: heat conduction, heat convection, and thermal radiation.
The Fourier Law of heat conduction is [26]:

$$q = \frac{Q_{cond}}{A} = -\kappa \frac{\Delta T}{\Delta x} \tag{2.9}$$

Thermal conductivity κ is a property of a material by virtue of which it conducts heat From this equation, the thermal conductivity κ is equal to:

$$\kappa = \left(\frac{\Delta T}{\Delta x} \cdot A\right)^{-1} \cdot Q_{cond} \tag{2.10}$$

If $A = \Delta T / \Delta x = 1$:

$$\kappa = Q_{cond} \tag{2.11}$$

Thus, the thermal conductivity is defined as the transferred heat through a cross-section surface of unitary area for a unitary temperature gradient $\Delta T / \Delta x$.
In addition, the thermal resistance R refers to the ability of a system to resist the heat transfer. The thermal resistance of a material is [26]:

$$R = \frac{\Delta T}{Q_{cond}} = \frac{dx}{\kappa A} \tag{2.12}$$

Thus, R is the resistance exerted by a material against the flow of heat through it. On the other hand, the thermal conductance K is the inverse of the thermal resistance [26]:

$$K = R^{-1} = \kappa \frac{A}{dx} \tag{2.13}$$

Therefore, the thermal conductance is the easiness with which heat flows through a cross-section.
The second mechanism of heat transfer is the heat convection. The Newton Law of cooling is [26]:

$$Q_{conv} = h \cdot A(T - T_a) \tag{2.14}$$

Where h is the thermal convection coefficient [W/m^{2}K], and T_a[K] is the ambient temperature.
The last mechanism of heat transfer is the thermal radiation. The Stefan-Boltzmann Law is [26]:

$$Q_{rad} = A \cdot \epsilon \, \sigma \, (T^4 - T_a^4) \tag{2.15}$$

Where $\sigma = 5.67 \cdot 10^{-8}$ [W/m^{2}K^4] is the Stefan-Boltzmann constant, and ϵ is the emissivity of the material.

TEG heat budget

This section addresses the heat present at the TE module. It has to be mentioned that the TE module has N couples of semiconductor, each of them with a leg of p-type and n-type material.
The TEG thermal resistance is represented as R_{TEG}. Its value is indeed a function of the electrical current flowing out the module [27].

The incoming and outgoing heats are composed of three terms: Heat conduction, Peltier effect, and Joule effect. Applying (2.6) from the Thomson relations, the Peltier effect depends on the Seebeck coefficient.

$$Q_{in} = \overbrace{(K_p + K_n)\Delta T}^{\text{Conduction}} + \overbrace{(\alpha_p - \alpha_n)T_h I}^{\text{Peltier effect}} - \overbrace{\frac{1}{2}R_{TEG}I^2}^{\text{Joule effect}} \quad \textbf{(2.16)}$$

$$Q_{out} = (K_p + K_n)\Delta T + (\alpha_p - \alpha_n)T_h I + \frac{1}{2}R_{TEG}I^2 \quad \textbf{(2.17)}$$

Q_{in} and Q_{out} [J] stand for the heat absorbed at the hot side and the heat rejected at the cold side, respectively. The thermal gradient $\Delta T = T_h - T_c$.
By letting $\alpha = \alpha_p - \alpha_n$ and $K = K_p + K_n$ equations (2.16) and (2.17) are simplified:

$$Q_{in} = K\Delta T + \alpha T_h I - \frac{1}{2}R_{TEG}I^2 \quad \textbf{(2.18)}$$

$$Q_{out} = K\Delta T + \alpha T_c I + \frac{1}{2}R_{TEG}I^2 \quad \textbf{(2.19)}$$

Heat Conduction

It models the Fourier conduction law at the TE module. The thermal conductance coefficient K is given by [26]:

$$K = \left(k_p \frac{A_p}{L_p} + k_n \frac{A_n}{L_n}\right) \quad \textbf{(2.20)}$$

Where A[m^2] is the cross-sectional area of the TE, L[m] is the length between plates, and κ [$W/m \cdot K$] indicates the thermal conductivity.

Peltier Effect

As the Seebeck effect generates a voltage at the semiconductors (αT), Peltier effect will occur. The magnitude of heat absorbed or released at each junction is proportional to the transmitted current [20].

Joule Effect

The Joule effect occurs when an electric current flowing through a conductor produces heat thermodynamically irreversible that is accounted as a loss [26].

$$P_J = R_{TEG}\ I^2 \quad \textbf{(2.21)}$$

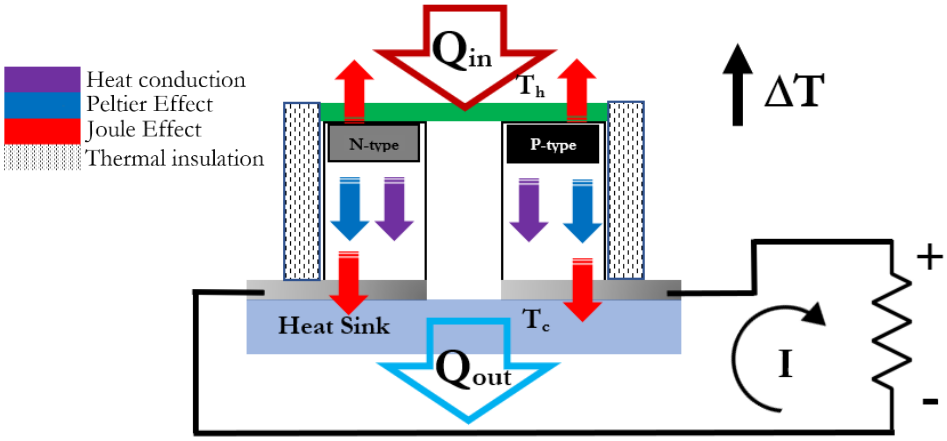

Figure 2.11 Heat budget of a TEG

According to the power balance equations:

$$W = Q_{in} - Q_{out} = \alpha \Delta T I - R_{TEG} I^2 \quad \textbf{(2.22)}$$

Electrical analysis of a TEG

Under the assumption of constant temperature at both sides of the module, the steady-state electrical parameters of the TEG can be simplified to a DC voltage source V_{OC} in series with an internal resistance r_{TEG}. As Figure 2.12 depicts, when a load is connected to the terminals of the TEG, the V_{TEG} is calculated as:

$$V_{TEG} = V_{OC} - I \cdot r_{TEG} \quad \textbf{(2.23)}$$

$$V_{TEG} = I \cdot R_{load} \quad \textbf{(2.24)}$$

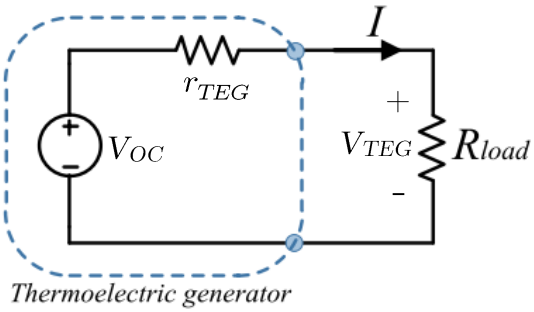

Figure 2.12 TEG closed circuit

Applying (2.8) to (2.23) and (2.24):

$$I = \frac{V_{OC}}{R_{load} + r_{TEG}} = \frac{\alpha \cdot \Delta T}{R_{load} + r_{TEG}} \quad \textbf{(2.25)}$$

Finally, the power delivered by the TEG is equal to:

$$P_{TEG} = V_{TEG} \cdot I = I^2 \cdot R_{load} = \frac{\alpha^2 \cdot \Delta T^2}{(R_{load} + r_{TEG})^2} \cdot R_{load} \quad \textbf{(2.26)}$$

Equation (2.26) is the general expression used for calculating the output power of a TEG. It might be seen that the maximum output power is reached when the load resistance R_{load} is equal to the internal resistance r_{TEG}, i.e. the matched factor $\varepsilon = R_{load} / r_{TEG} = 1$. In this case, it is said that the load is matched.

$$P_{TEG,max} = \frac{\alpha^2 \cdot \Delta T^2}{4 \cdot R_{load}} \quad \textbf{(2.27)}$$

From (2.27) it can be noticed that the Maximum Power Point (MPP) occurs when (2.28) is fulfilled:

$$V_{TEG} = \tfrac{1}{2} V_{OC} \quad I_{TEG} = \tfrac{1}{2} I_{SC} \quad \textbf{(2.28)}$$

Figure of Merit

The figure of merit ZT is the parameter that describes the performance of the TEG materials. It is expressed as it follows:

$$ZT = \frac{\alpha^2 \sigma T}{k} = \frac{\alpha^2 T}{k\rho} \quad \textbf{(2.29)}$$

Where σ [S/m] stands for the electrical conductivity, whereas the electrical resistivity ρ is the inverse of the electrical conductivity. κ [W/m · K] stands for the thermal conductivity, and T[K] is the absolute temperature.

Thus, the efficiency of the TEG can be determined once the ZT has been characterized. Currently, commercial available TEG have a Figure of Merit lower than 1, what accounts for an efficiency up to 6% [28].

Efficiency of TEG

Although promising, TEG technologies have lower generation efficiency compared to conventional thermodynamic systems such as Stirling, PV, or Rankine systems. Figure 2.13 shows a comparison between different thermodynamic engines performance for a constant cold side of 25ºC.

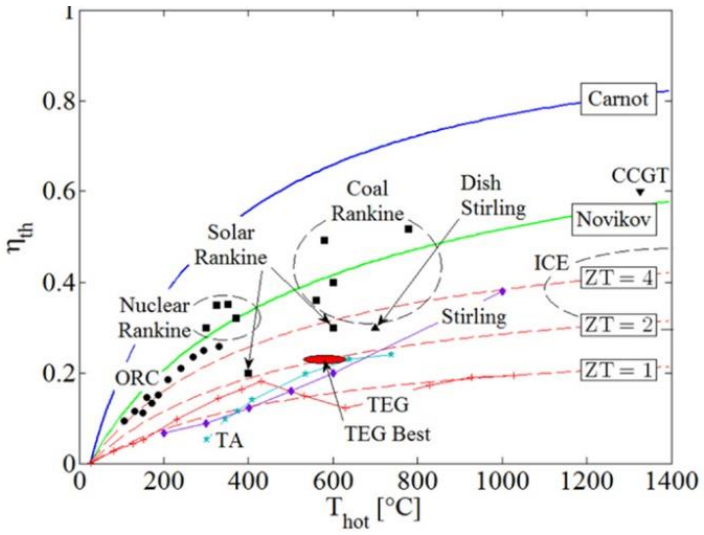

Figure 2.13 Efficiencies of different energy conversion technologies compared to TEG performance for different ZTs [32]

The maximum thermodynamic efficiency is imposed by the Carnot efficiency (blue line) according to $\eta_C = 1 - \frac{T_C}{T_H}$ and the Novikov efficiency (green line) is given by $\eta_{th} = 1 - \frac{T_C}{T_H} \times 0.5$. The TEGs performance (red dashed lines) is given for different figures of merit. It can be noticed how the figure of merit of TEG systems should be as high as possible in order to reach higher efficiencies.

The efficiency formula is:

$$\eta = \frac{P_{TEG}}{Q_i} = \frac{V_{TEG} \cdot I}{Q_i} \tag{2.30}$$

The condition for reaching the highest efficiency of the TEG is:

$$\epsilon = \frac{R_{load}}{r_{TEG}} = \sqrt{1 + ZT} \tag{2.31}$$

$$\eta_{max} = \frac{T_H - T_C}{T_H} \cdot \frac{\sqrt{1+ZT}-1}{\sqrt{1+ZT}+\frac{T_C}{T_H}} \tag{2.32}$$

As previously mentioned, current research venues are focused on improving the TEG efficiency.

TEG performance curves

For illustrative purposes all the following curves correspond to the same TEG module [29]. The cold side remains constant at 100ºC.

It can be noticed from equations (2.24) and (2.25) that output current and voltage are functions of the temperature gradient.

As far as the module works in its temperature operation range, the electrical power production increases along with the temperature.

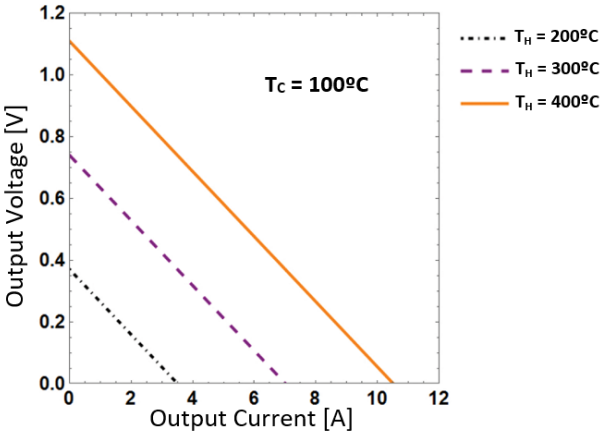

Figure 2.14 VI curve of a TEG

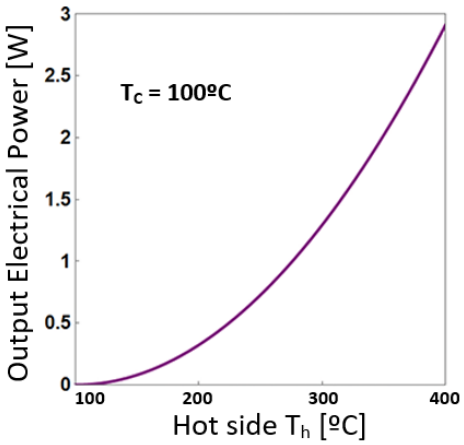

Figure 2.15 Power curve of a TEG vs hot side temperature

Due to the fact that both voltage and current depend on temperature, the MPP is actually a function of the thermal gradient of the TEG module. Figure 2.16 represents the evolution of the MPP for different temperature gradients. The reader can appreciate how the MPP is located according to (2.28).

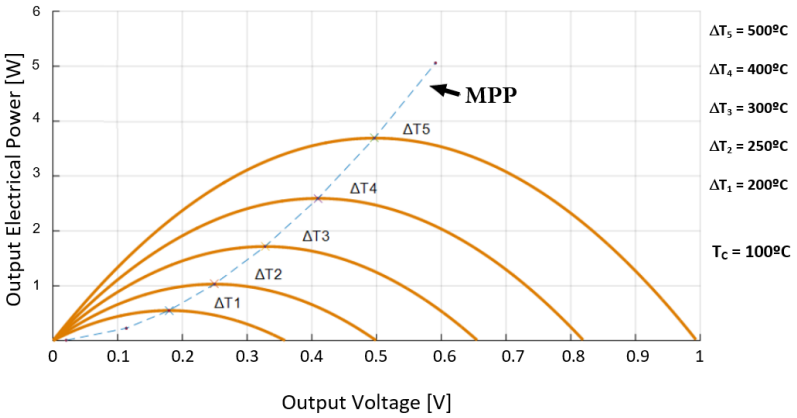

Figure 2.16 TEG MPP curve variation depending on temperature

Figure 2.17 depicts the previously mentioned production efficiency, which is limited according to (2.32) by the Figure of Merit. When it comes to the load, it can be observed where is the matched load of the system, and its utmost importance on power production. The proper estimation of its value is crucial for working in the optimum range.

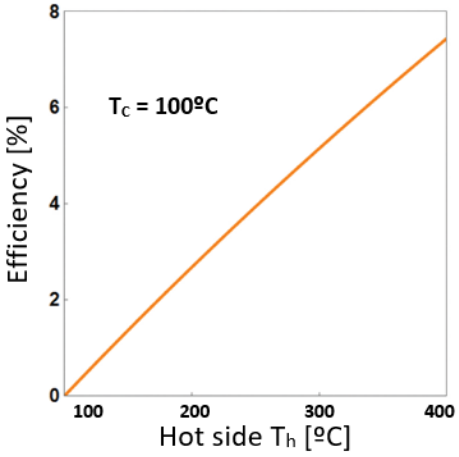

Figure 2.17 Efficiency curve of a TEG

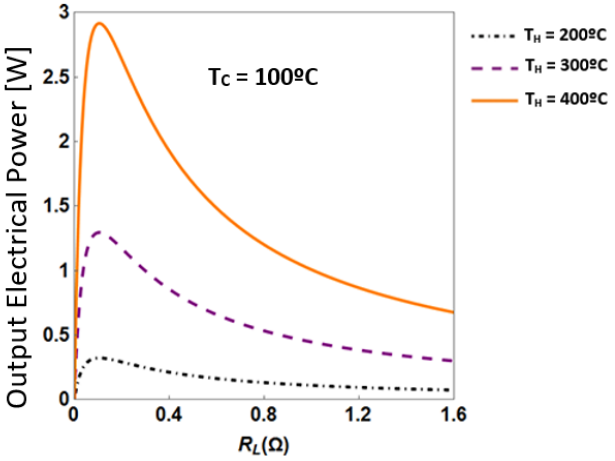

Figure 2.18 Power curve of a TEG vs load resistance

TEG module materials improvement

The current research venues regarding TEG systems are focused on increasing the Figure of Merit. Nowadays, most of TEG modules are made of bismuth telluride Bi_2Te_3 or lead telluride PbTe. The average ZT values are in the range 0.5~0.8 for 400~500 K [28].

The outlook for researching is to reach efficiencies above 10% by developing new materials of ZT >2. Just to mention, alloys of Bi_2Te_3/Sb_2Te_3 have reported ZT up to 2.4 at room-temperature [30], and 700K [31]. However, the interdependency of the TEG parameters makes the enhancement efforts very challenging.

The Seebeck coefficient, the electrical conductivity, and the thermal conductivity have a great importance in terms of increasing the Figure of Merit, as can be noticed from (2.33).

$$ZT = \frac{\alpha^2 \sigma T}{k} \qquad \textbf{(2.33)}$$

Firstly, the factor $\alpha^2\sigma$, known as Power Factor, depends on the Fermi level of the semiconductor. For achieving a high Power Factor, and so, a high efficiency, it is required to dope the semiconductor material to place the Fermi level close to the bottom of the conduction band [32].

As shown in Figure 2.19, the problem lies in the interdependency of these parameters.

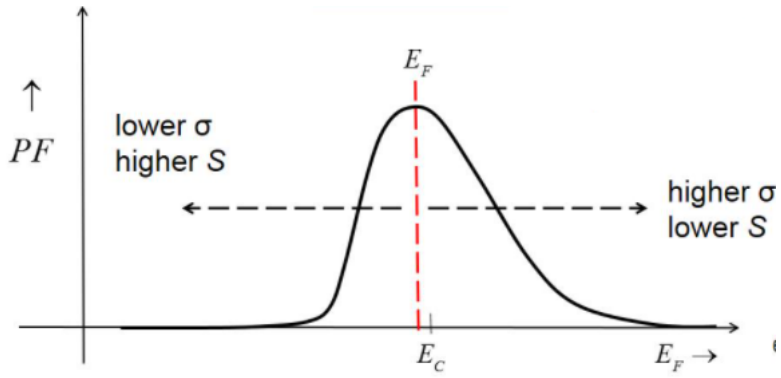

Figure 2.19 Power Factor of the Figure of Merit dependency on Fermi Level [33]

Secondly, the thermal conductivity is proportional to the electrical conductivity of the materials [34] according to:

$$\kappa = \sigma T \cdot L \tag{2.34}$$

Where L is the Lorentz factor for free electrons, $2.4x10^{-8}$ $[J^2/K^2C^2]$.

Nowadays, there are different standpoints for improving TEG efficiency. For instance, Photon scattering at different frequency ranges utilizing methods such as mass fluctuation scattering [35], developing complex crystal structures to reduce thermal conductivity [36]. Perhaps, due to the fact that TEG properties are relatively easier to handle independently at tiny scales, the main approach is focused on the development of nanostructures [37]–[39].

In addition, there is a great deal of interest in certain organic materials that are ideal for low temperature applications [40]. On the other hand, Bi_2Te_3. is limited at 250ºC. The use of new materials that cover a wider range of temperatures would improve the harvesting of wasted heat.
Due to the fact that the Seebeck effect is based on charge carriers displacement, there is an efficiency loss when the terminals of the TEF are connected to wires, since these may electrons that oppose to the voltages produced in the semiconductor. This issue can be overcome by developing a metal able to conduct electricity with positively charge particles instead of electrons.

Applications and Solar TEG systems

TEG modules are able to harness energy from a wide variety of heat sources, at either high, low or ultra-low temperature gradients. Moreover, these devices are able of changing its polarity depending on the sense of the heat flux. This feature is especially interesting for a continuous operation over time.
For instance, TEG modules are used for harnessing heat from industrial processes[41], steam [42], ground [43], and vehicles [44], [45]. They can even generate electricity from the human body heat [46].

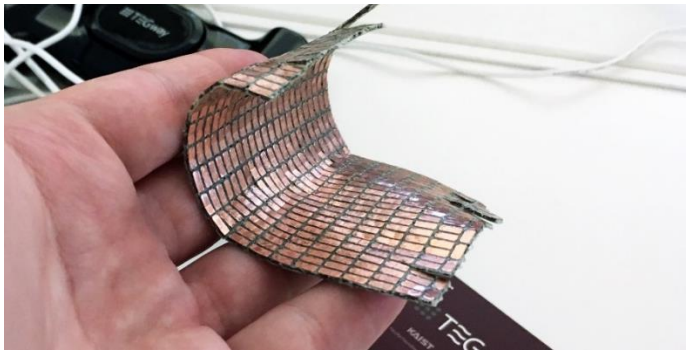

Figure 2.20 TEGWAY© flexible thermoelectric technology for harnessing human heat [47]

Solar TEG modules use the solar irradiation as heat source. These systems required a concentration mechanism in order to increase the incoming radiation. Two different concentration techniques are commonly applied:

- High absorptivity panels. This approach minimizes the radiation heat transfer. By doing so, the incoming solar irradiation is forced through the TE module [48].

- Optical concentration mechanisms. These systems use lenses for directing the sunlight. The use of lenses has reported a 33.5% increase in the TEG efficiency [49].

2.3. DC-DC power converter applied to TEG systems

2.3.1. DC-DC converter

A DC-DC power converter is an electronic circuit that transforms an input voltage into a controlled output voltage. In fact, DC-DC converters allow to control the average output voltage to match a desired level regardless of the fluctuations at the input voltage and the load. These converters are often used as drivers for DC motors or as regulated power supplies. The output of the converter can be either isolated or non-isolated from the input [50].

There are two main topologies of DC-DC power converters: the Step-down (Buck), and the Step-up(Boost). In addition, there exist different combination of these two main topologies such as the Step-down/Step-up (Buck-Boost), the Cuk converter, and the Full-Bridge [51].

Buck converter

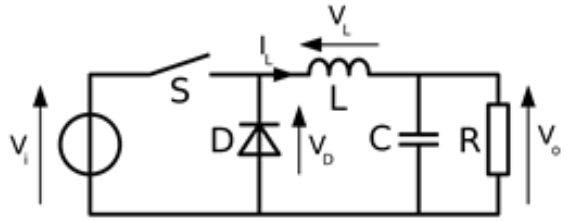

- $V_o < V_i$
- Unidirectional power transfer
- Applications:
  - regulated power supply
  - control of DC motors.

Boost Converter

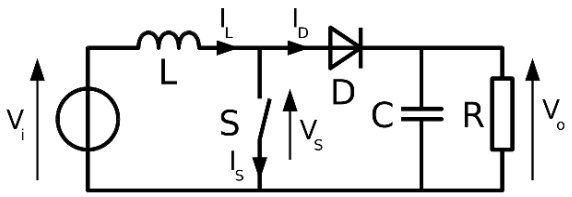

- $V_o > V_i$
- Unidirectional power transfer
- Applications:
  - regulated power supply
  - braking of DC motors

Buck-Boost Converter

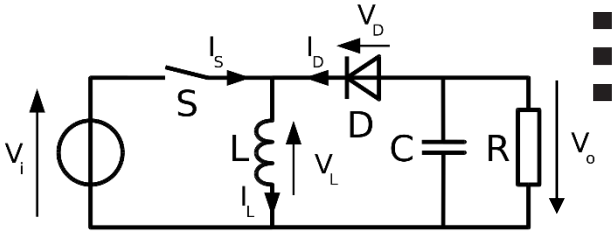

- $V_o \gtrless V_i$
- Unidirectional power transfer
- Applications:
  - regulated power supply with reverse polarisation.

Cuk converter	
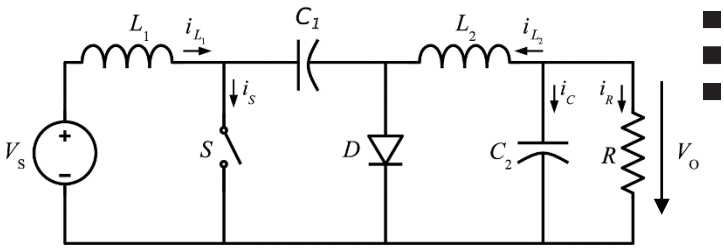	■ $V_o<V_i$ ■ Unidirectional power transfer ■ Applications: - regulated power supply with reverse polarisation.
Full-Bridge	
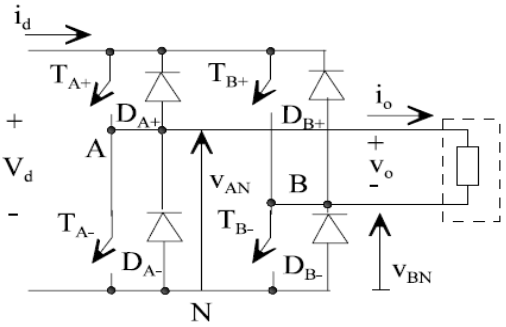	■ $V_o<V_i$ ■ Bidirectional power transfer ■ Applications: - DC motor drivers

Table 2.1 DC-DC converter topologies [51]

Switched-mode DC-DC converters are used to convert an unregulated input into a controlled DC output at a desired voltage level by varying the "on" and "off" times of the switch (t_{on} and t_{off}).

Pulse Width Modulation (PWM) is the most common deterministic technique to control the switching frequency f_{sw}, and so, the average value of output voltage. In this method, a constant frequency is used and the duty cycle D, which is defined as the ratio between the closing time and the switching period, is modified

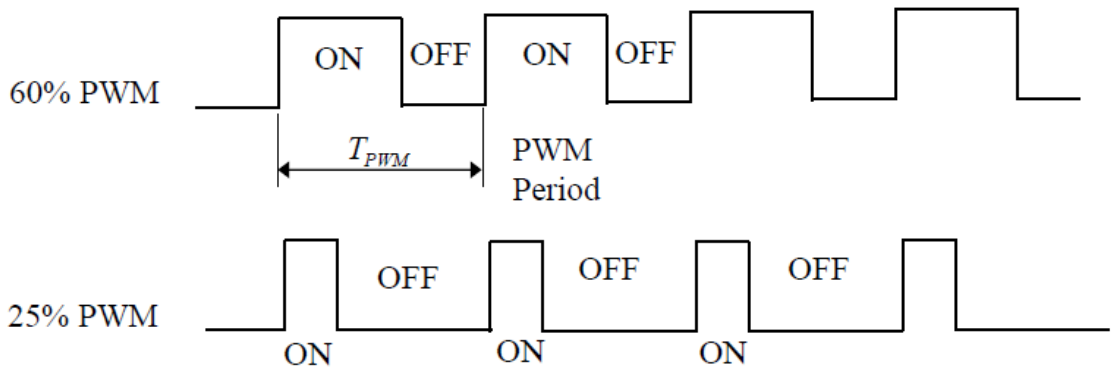

Figure 2.21 Pulse Width Modulation

The DC-DC converters operate at two modes: continuous conduction mode (CCM) and discontinuous conduction mode (DCM). In practice, a converter can work in both modes, which have significantly different characteristics.

2.3.2. Power conversion of TEG-based systems

When using TE modules as power generators, it is mandatory to include a conditioning stage for overcoming the voltage fluctuations and adjust the low voltage generated. Hence, there is a great challenge in designing DC-DC converters with high efficiency and low power consumption.

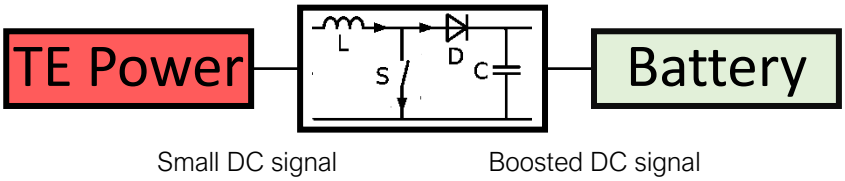

As previously mentioned, the maximum power point of the TE depends on temperature. Thus, a maximum power point tracker (MPPT) is included in a feedback loop and controls the switching frequency of the converter.

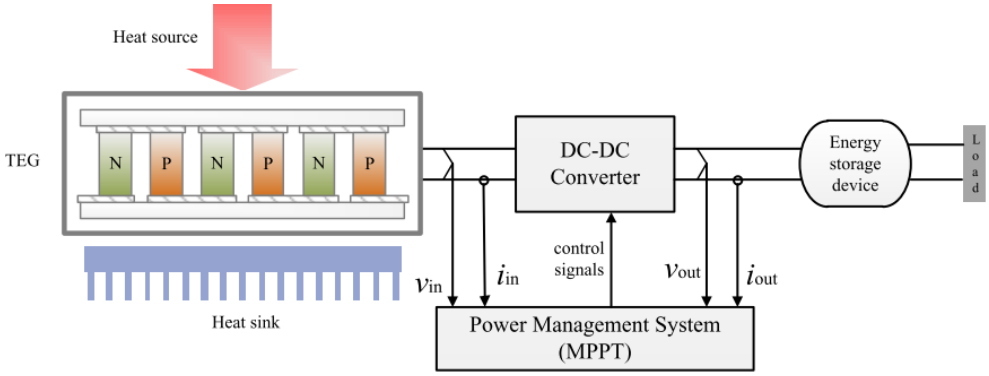

Figure 2.22 Power supply based on TEG with a MPPT system

The MPPT guarantees the optimum power at the operating condition. In terms of control algorithms, there is a large list of options, namely the Perturb&Observe algorithm (P&O) [52], Incremental Conductance [53], Fractional Open-Circuit Voltage and Short-Circuit Current [54], Fuzzy Logic Control [55], and Neural Network control [56].

P&O is the most common algorithm. It makes small changes in the output voltage and tracks the output power until MPP is reached. However, this algorithm has difficulties in rapidly changing conditions. Indeed, it is difficult to accurately identify the MPPT without the existence of TEG simulators.

Current researches address the efficiency improvements from different standpoints. For instance, adjusting the switching times depending on the input voltage [57], [58], topologies with multiplier structure based on voltage doublers [46], and improved MPPT more accurate and reliable [59]–[61].

2.4. **Photovoltaic solar systems and SolarG project**

This section introduces the elements of a typical PV installation with emphasis on those auxiliary elements suitable to be powered by the TEG system developed in this project.

The work developed in this thesis has been experimentally evaluated in the same conditions of the PV installations of the SolarG project [62], and the power consumption estimations are made for its own auxiliary elements.

SolarG project

SolarG is a research project developed at Universidad de Alcalá (Spain). This work proposes a novel PV panel cooling system based on low-power geothermal technology, which will increase the efficiency of photovoltaic solar panel installations. In order to achieve this, a pumped closed water circuit is implemented. This system transfers the heat from the cells to the ground.

The testing prototype is placed in the city of Alcalá de Henares. The PV system is comprised by two PV panels(2x1m) assembled to an one-axis solar tracker equipped with a linear actuator. The installation has a MPPT device, a meteorological station provided with a solar irradiation sensor, an anemometer, and a thermometer. The system in question has an underground water circuit, a centrifugal pump, and a data acquisition board for measuring the different temperatures, and voltages.

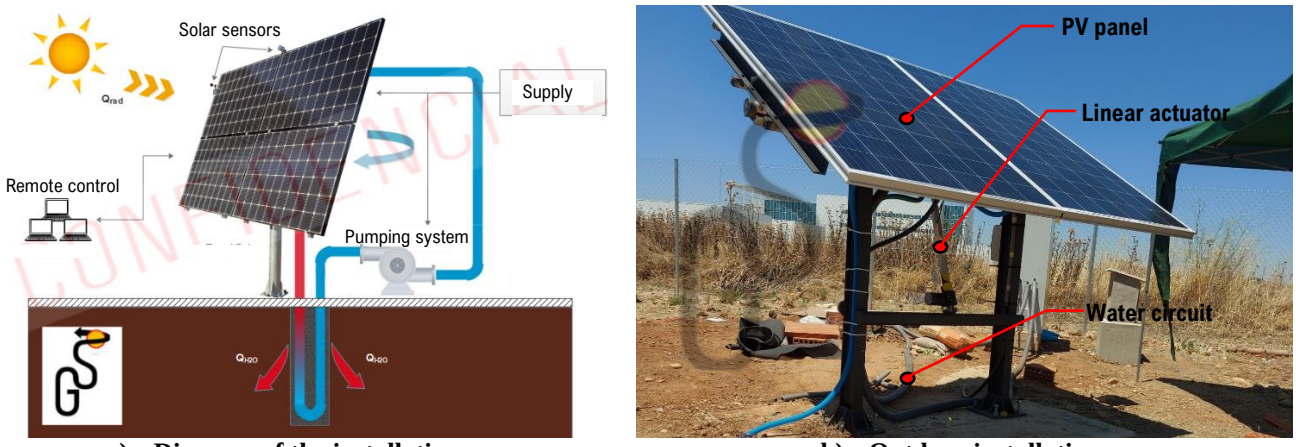

a) **Diagram of the installation** b) **Outdoor installation**

Figure 2.23 Installation of SolarG project - Testing prototype [62]

Elements of a PV solar installation

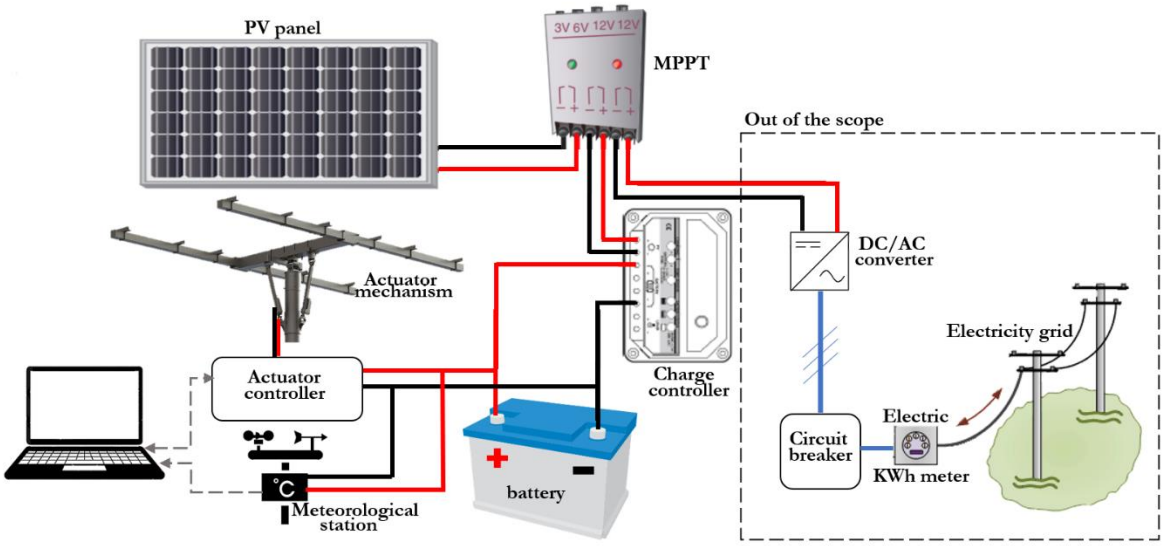

Figure 2.24 Diagram of a PV setup

The main components of a stand-alone PV installation are [63], [64]:

I. The PV panel

A photovoltaic panel is comprised of multiple solar cells connected into arrays. They are used to generate electricity using solar energy. The solar cells of the PV module are semiconductor electrical junction devices.

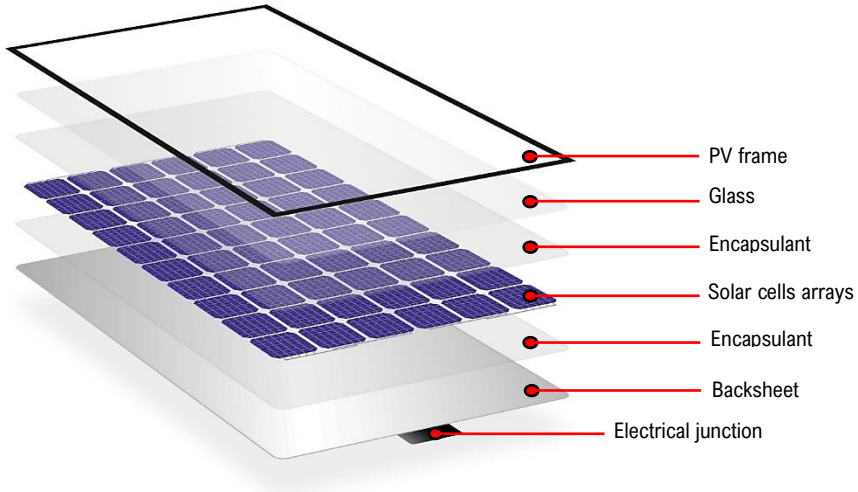

Figure 2.25 Solar PV panel layout

A wide variety of semiconductors have the potential of yielding solar cells. In fact, high conversion efficiency and suitability of fabrication are the main factors when selecting the suitable material for a solar cell.

II. Tracking system

Solar trackers can be classified as one-axis or double-axis tracking structures. If the system is a single-axis solar tracker or SAST, there is one degree of freedom that follows the sun's movement in one direction; it can be either horizontal (HSAT)- South North Seasonal path- or vertical (VSAT)- East West Daily Path. The most common actuator mechanisms are: DC motor + brake, endless crown, or the linear actuator.

III. Panel sensors

The main sensors for monitoring the system parameters include the solar irradiation sensor, thermometers for the PV cells temperature, weather sensors such as an anemometer (high winds may damage the structure if it is far from the rest position). SolarG project includes a flowmeter and a data acquisition board.

It has to be mentioned that sensors and other measuring devices have the lowest power consumption in PV systems, compared to the tracking mechanism.

IV. MPPT and power regulator

The MPPT (maximum power point tracker) is a DC-DC power converter that adapts the output voltage of the panels to the input voltage that the battery needs for being charged. The MPPT regulator digitally tracks the output of the panels and compares it to the voltage of the batteries. Its microprocessor calculates the optimum power that the regulator can deliver to the batteries at each state of charge.

Typically a power improvement of 20-45% in winter and 10-15% in summer can be obtained by using a regulator with MPPT maximum power point tracking. This varies depending on weather conditions, battery condition and other factors.

In grid-connected inverters, the power generated by the panels is converted to alternating current instead of being stored in batteries. In such cases the MPPT regulators calculate the optimum power to feed the DC-AC inverter.

V. Solar batteries

The solar batteries are designed to absorb and supply electricity by using a reversible chemical reaction. Deep-cycle batteries are designed to discharge between 50% and 80%. However, best lifespan is to keep the average cycle at about 50% or less.

Depending upon the solar array configuration, typical battery banks can be of 12V, 24V, or 48V and many hundreds of amperes in total.

The battery stage includes a charge controller in charge of regulating and controlling the output power. This device prevents the batteries from being over charged (or over discharged) by dissipating the excess power into a load resistance.

2.4.1. PV efficiencies and temperature influence

Nowadays, almost 90% of PV cell types are Crystalline Silicon based, namely monocrystalline silicon and multicrystalline silicon. The next biggest type refers to the Thin-Film Silicon cells. Cells based on Copper Indium Gallium Selenide (CIGS), CdTe or amorphous silicon belong to the Thin-Film Silicon group [65], [66]

A new emerging cell technology is the Perovskite solar cell (PSC), introduced in 2009. It has brought enormous progress in terms of energy efficiency ever since, even though it is still difficult to determine the electrical characteristics of these devices. [67], [68].

	Technologies	Advantages	Disadvantages
Crystalline Silicon	Monocrystalline silicon **Eff:** 25.6±0.5 % **Area for 1kW:** 3.8~4m^2	• Tested and established technology. • Stable at outdoor working conditions. • Relatively efficient.	• More sensitive to the temperature's variation than multicrystalline and amorphous silicon. • Waste of material in slicing wafers. • Costly to manufacture.
	Multicrystalline silicon **Eff:** 21.3±0.4 % **Area for 1kW:**4.6~4.8 m^2	• Tested and established technology. • Stable at outdoor working conditions. • Relatively efficient. • Less expensive than Monocrystalline.	• Slightly less efficient than Monocrystalline silicon. • Waste of material in slicing wafers. • Still costly to manufacture.
Thin Film	Copper Indium Gallium Selenide (CIGS) **Eff:** 21.0±0.6 % **Area for 1kW:**4.6~4.9 m^2	• Relatively efficient. • The optical bandgap can be tuned by varying the concentration of semiconductors to match the solar spectrum. • Improved V_{OC} can be obtained incorporating Ga.	• The vacuum production process of is time-consuming and expensive. • Unstable. The recycling of the Selenide vapor from the side walls of the system is a major limitation.

	Amorphous Silicon **Eff:** 10.2±0.3 % **Area for 1kW:**9.5~10 m^2	• Inexpensive. • Little material is needed. • Rapid and highly automated production.	▪ Low efficiency. ▪ Degradation in power output.
Others	Perovskite solar cells (PSC) **Eff:** 19.7±0.6 % **Areafor1kW:**4.9~5.2 m^2	• Relatively efficient. • The high absorption coefficient enables ultrathin, lightweight and flexible solar modules films. • The fabrication methods such as printing techniques have a low production cost.	• The material is toxic in nature. ▪ Degradation issue. The perovskite material breaks down quickly due to exposure of heat.

Table 2.2 Solar cell technologies comparison [66], [69]–[72]

For the sake of solar energy viability, it is mandatory to achieve the highest efficiency [1] possible during the light hours taken into account that PV generation is stopped during night periods. This improvement of the PV system performance may be achieved from different approaches.

Influence of temperature on PV performance

The physical process through which a solar cell converts sunlight into electricity is called photovoltaic effect. Certain semiconductor materials such as silicon exhibit the photovoltaic effect when exposed to sunlight. This happens because sunlight is composed of energy packets called photons, whose energy is associated with their wavelengths.

To generate electricity, electrons and holes need to be separated. If a load is connected between the terminals of the semiconductor, the circuit is closed and allows the electrons to flow. The free electron movement from one layer to the next one generates electricity. Direct current (DC) electrical power is therefore available [5], [73].

[1] When determining the PV module ratings, the standard testing conditions (STC) are applied as an industry-wide standard to indicate the performance of PV modules and specifies a cell temperature of 25ºC and 1000W/m^2 of total irradiance (UNE-EN IEC 61853-3:2018 [100])

Moreover, all the individual efficiencies of the PV system (thermodynamic efficiency, Fill Factor, absorption efficiency, and thermalization efficiency) suffer the same tendency [74]. This variation is related to certain coefficients of the material and the fact that as temperature increases, the density of intrinsic carriers decreases. The efficiency relation has been modelled as follows [75]:

$$\eta = \eta_{\mathrm{Tref}} \left[1 - \beta_{\mathrm{ref}} \left(T_c - T_{\mathrm{ref}} \right) + \gamma \log_{10} I \; t \right] \tag{2.1}$$

Where η_{Tref} is the efficiency at the temperature and solar radiation reference (STC: 25ºC and 1000 W/m^2 respectively according to UNE-EN IEC 61853-3:2018), β_{ref} is the temperature coefficient, and γ is the solar radiation coefficient. The two latter depend on the material properties. The following graph depicts the influence of temperature on different modules:

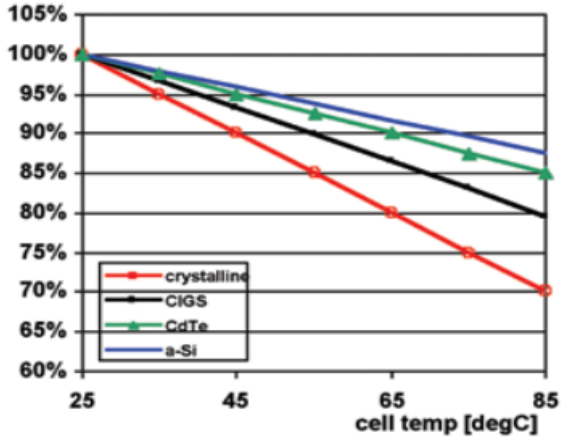

Figure 2.26 Effect of temperature on PV module performance relative to STC

Different techniques of thermal management have been applied to the PV system to reduce the module heating. Techniques such as including heat sink/ fins with natural and forced convection air flow [76], [77], heat pipes [78], lays of phase change material (PCM) [79], microchannel heat transfer [80], or thermoelectric cooling [81], [82].

The results showed that a controlling the maximum temperature with cooling systems prompts a maximum rate increment of 15.06% of the open-circuit voltage, and increments by 10% the transformation productivity of the PV module [83].

2.5. **Patents search**

This section introduces four patents regarding solar concentration mechanisms applied to TEG modules. Each of them proposes a different technique for boosting the performance of the system.

Patent No **US20140290712A1** `Solar Thermoelectric Generator`

Colorado School of Mines, 2014

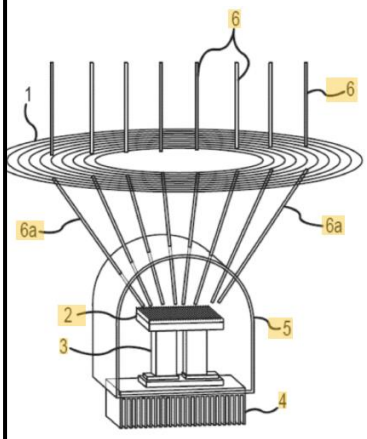

Figure 2.27 Patent US20140290712A1 diagram

This patent proposes a innovative design where the TEG module is housed in a dome-shape mechanism that focuses the light for the 360º

The author acknowledge the influence the lens in the losses of these generators. This solution virtually eliminates all of the emitted black body radiation and reduces the effect of the wind on the natural convection of the cell. This enables solar the TEG to achieve higher levels of optical concentration and operate at higher efficiency rates. This solution is suitable for both single and dual-axis mechanisms.

Patent No **20180000669** `Thermo-electric generator module`

CITY UNIVERSITY OF HONG KONG, 2018

No pictures are available of this patent. However, the authors describe a pioneer TEG system covered by special plates to increase heat absorption, and minimize heat dissipation regions. No concentration mechanism is included. In fact, the TE modules have a grid connection similar to a PV panel.

Patent **EP3255651** HYBRID SOLAR GENERATOR

GE Aviation Systems LLC, 2017

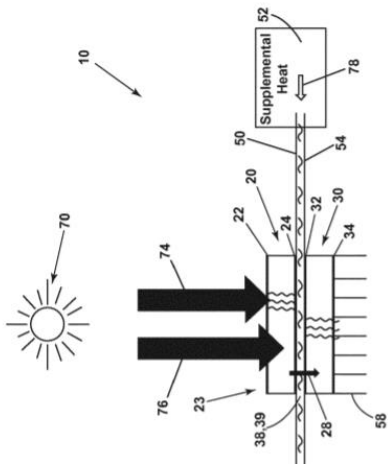

Figure 2.28 Patent EP3255651 diagram

This patent addresses the issue of the solar energy concentration from a different standing point. The authors have developed a hybrid system of solar concentration mechanism and solar thermal loads.

The thermal loads receive the irradiation from the sun and transfers the heat flux to the TE module through high thermal conductivity joints. By doing so, the thermal gradient is boosted without requiring a higher number of TE modules or a larger lens.

Patent No **201410435988.5** SOLAR GLASS TE INTEGRATED DEVICE

Inventors: Songshun Xu & Yin Xu, 2014

This device is particularly interesting because it gathers the three techniques of solar energy harnessing: solar thermal energy, photovoltaic energy, and solar concentration systems. The patent presents the invention of a solar glass with TEG modules. The purpose of its design is to reduce the reflection of the sunlight, what causes losses in the concentration mechanism. Moreover, this glass could be implemented on a PV panel, to increase the incidence of the sunlight. Thus, this invention is capable of using thermal energy, improve electrical energy production, reducing temperature of the photocell with TE devices, and ensuring proper power generation thereof.

The four patents abovementioned deal with the design of a power supply based on TEG modules from different perspectives. Either improving the irradiated surface, the absorptivity of the TEG module, the thermal load of the system, or the lens of the concentration mechanism.

The solar concentration TEG design developed in this project includes a concentration mechanism pioneer in the use of Fresnel lenses. One of the advantages lies in the improvement of the power performance of a small TEG cell compared to a five times larger TEG. This approach reduces significantly the heat convection losses.
In addition, the improved prototype overcomes the solar absorptivity issue of the TEG module and the solar orientation dependency.

Chapter 3

Design and development of the solar concentration thermoelectric generator

The best structure
will not guarantee performances,
but the wrong structure
is a guarantee of non-performance.

Peter F. Drucker

This chapter concerns the design of the outdoor system developed in this project. The laboratory setup and the assembly for the outdoor evaluation of the design are conducted in Chapter 4.

The conceptual design of the system is shown in Figure 3.1. The manual positioning mechanism has 3DOF for tracking the sun. Then, the incident solar irradiation is focused by the concentration mechanism onto the TEG cell. Its hotspot receives the solar heat while the heatsink evacuates the heat from the cold side. As a result, the TEG produces an output power transferred to the DC-DC converter. The output of the converter powers a rechargeable battery suitable for auxiliary components of the PV installation,

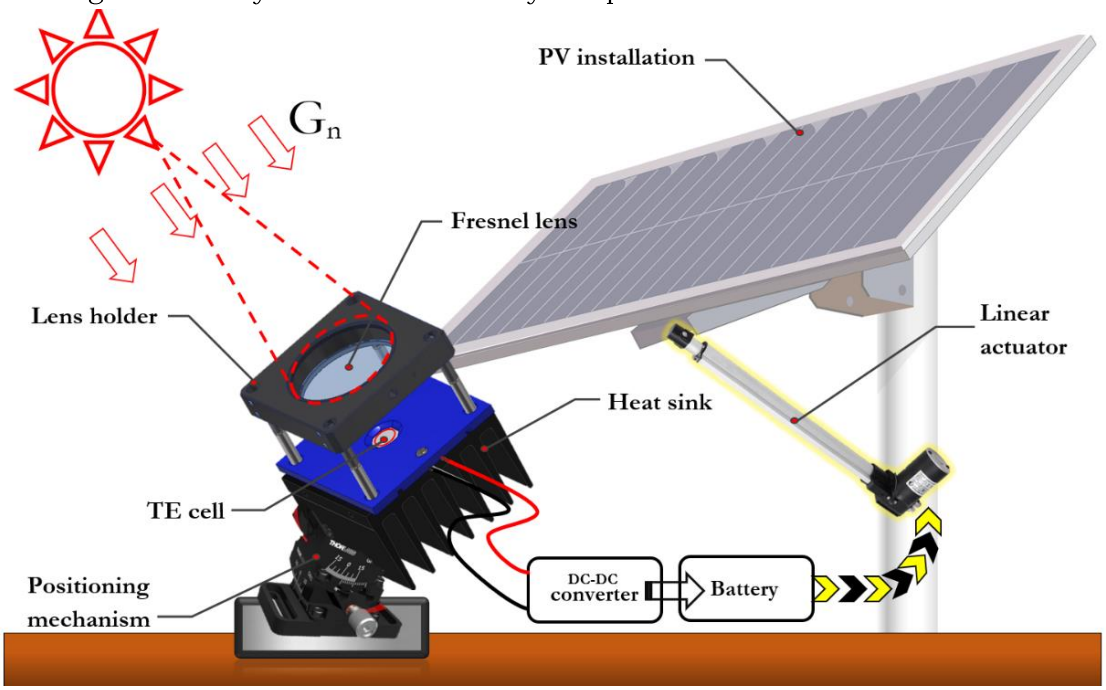

Figure 3.1 Conceptual design of the developed system

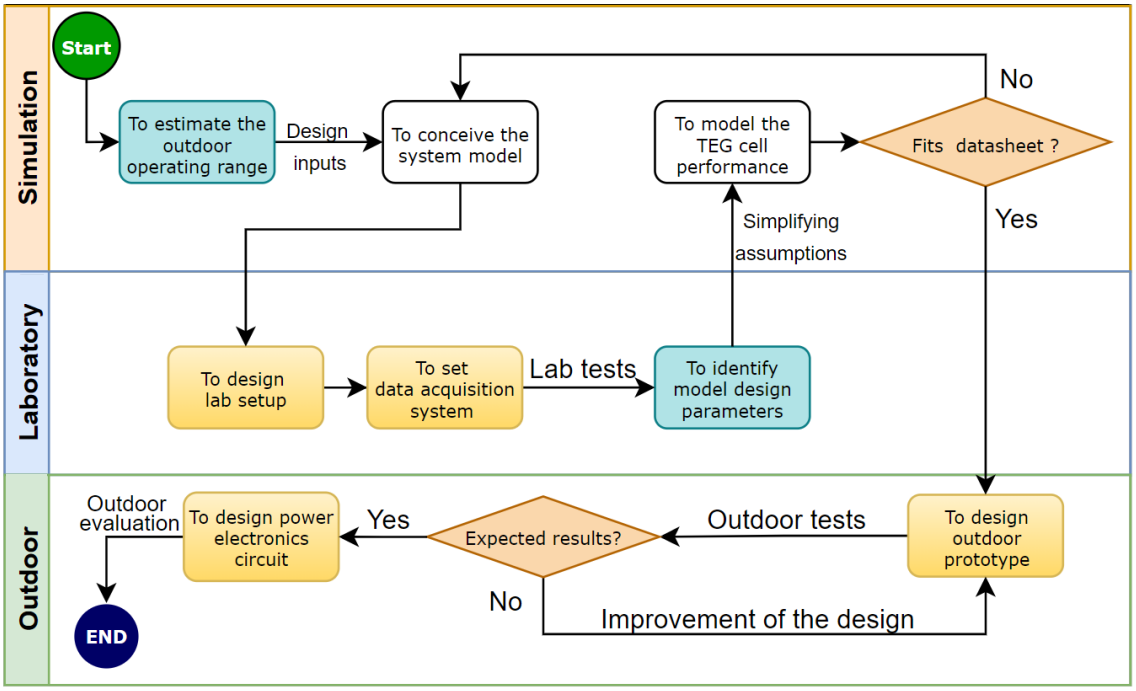

Figure 3.2 Flowchart diagram of the design process

The final system has been modelled and simulated, compared to the manufacturers performance specifications, evaluated at laboratory controlled conditions, and tested in the outdoor environment.

3.1. Description of the operating range

The outdoor tests will be carried out in the city of Alcalá de Henares (Madrid, Spain) in the month of July from 8:00h until 15:00h (See ANNEX VIII Sun path and solar irradiation).

The value of solar irradiation is not straightforward. In fact, the solar radiation record of the Photovoltaic Geographical Information System (PVGIS)[84] only includes the average monthly irradiation based on the average value between 2005 and 2016. In order to obtain an accurate value of the solar irradiation during the outdoor test, a solar calibrated sensor will be used.

	Expected working range
Air temperature	25ºC~35ºC
Solar irradiation	750~1000 W/m^2
Wind speed	0~0.5m/s

Table 3.1 Outdoor tests - expected operating range

3.2. Design of the preliminary prototype of the solar concentration TEG

This section addresses the design of the concentrating TEG system. Firstly, the components of the preliminary prototype are selected. These are: the TE modules, the concentration mechanism, heatsink, and the 3DoF orientation mechanism.

In the next chapter, the performance of the developed concentrating system will be compared to a non-concentrating system. The objective will be to assess the improvements that the concentrating design offers to the electricity production. Thus, an additional TEG system without a solar concentration is designed for operating in the same conditions.

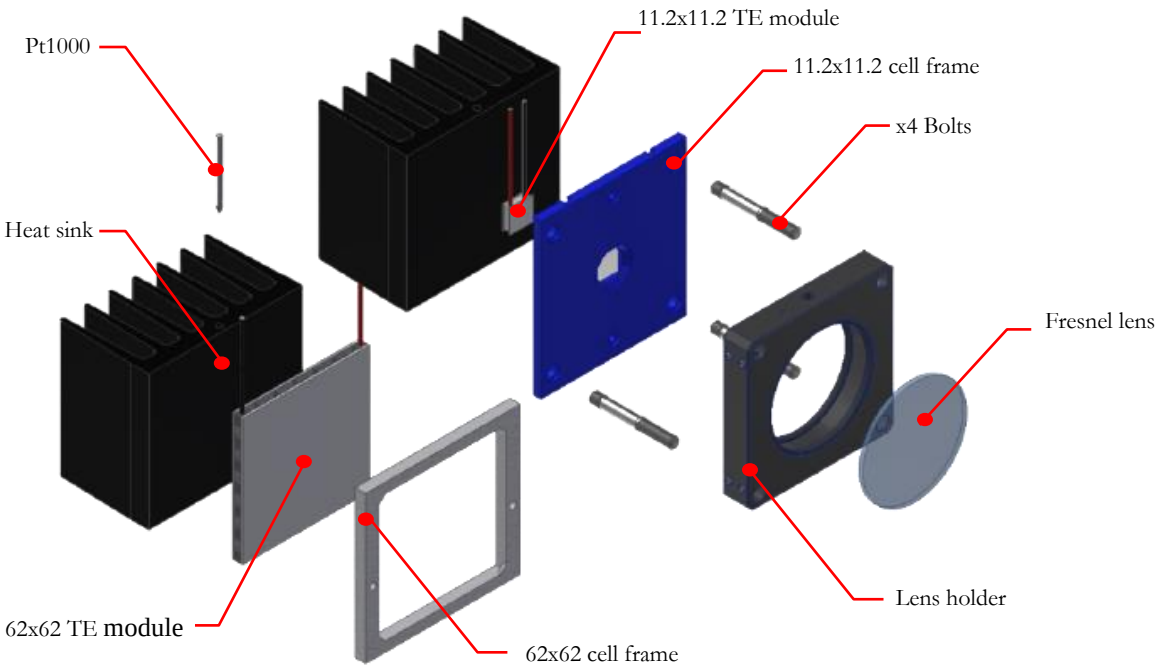

Figure 3.3 CAD design of the outdoor setup

The CAD design plan of the 11.2x11.2 concentrating TEG system is included in ANNEX IV Concentrating 11.2x11.2 TEG design plan.

TE modules

Two thermoelectric cells of different sizes are selected. The smaller one is used in the concentrating design and the larger TE cell serves for the reference system (Figure 3.3). Both TEG modules must share the same power performance for low temperature gradients in order to stablish a proper comparison between them.

TEG Calculator 

The author has developed a TEG calculator program that allows to easily compare different TE modules just from the available coefficients. The TEG calculator program is based on MATLAB App Builder (ANNEX III Developed TEG Calculator – MATLAB code).

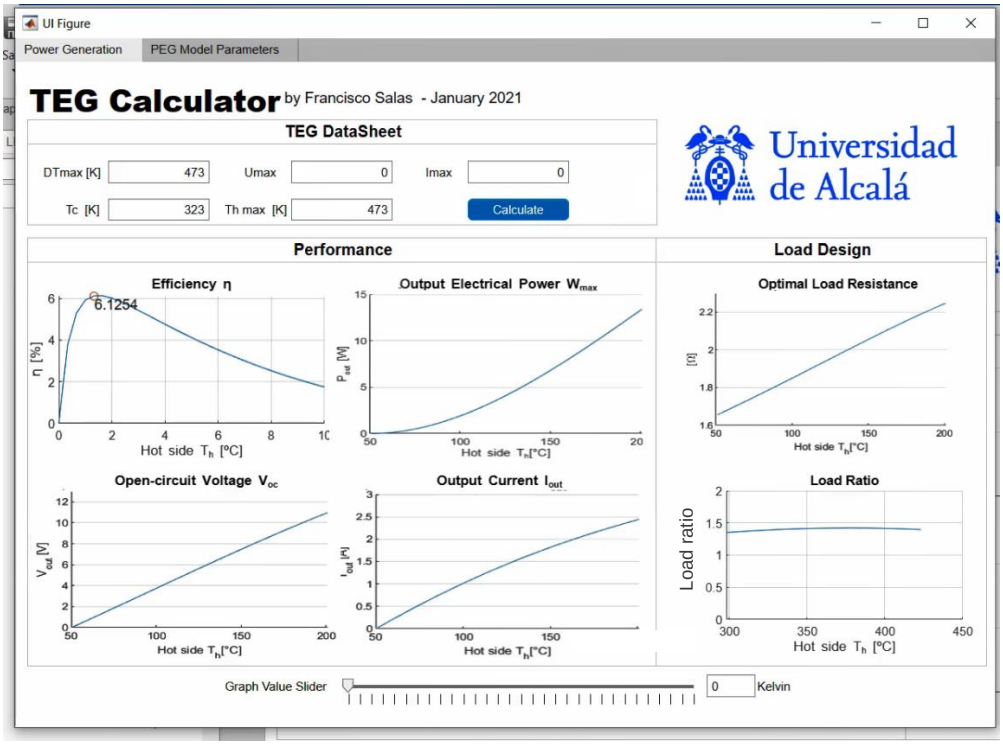

Figure 3.4 Developed TEG program interface – Performance and Load Design

It is a practical and intuitive executable that shows the TEG curves necessary for the design of harvesting systems. It calculates the different parameters applying the equations introduced in section 2.2.2 for a given temperature range. Besides the performance curves, the variation of the TE coefficients depending on temperature are plot as well. The program allows the user to select the TEG from a list of different modules.

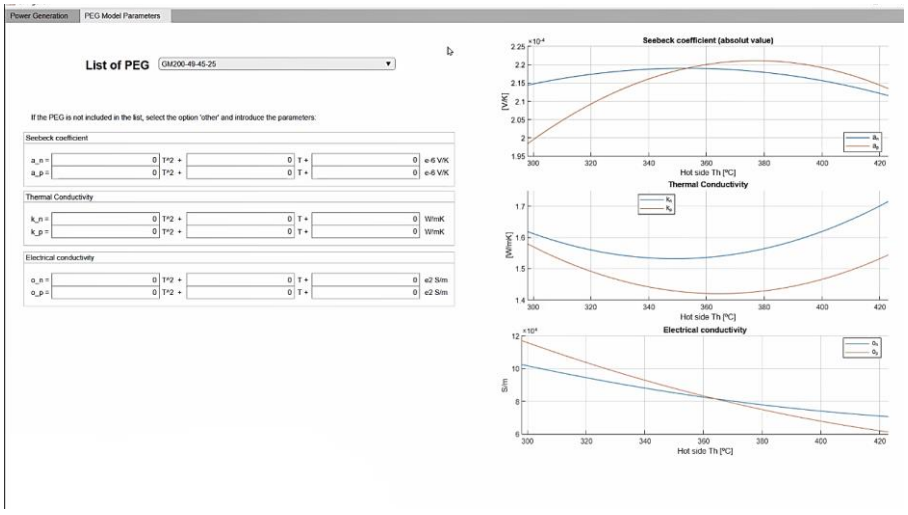

Figure 3.5 Developed TEG program interface - TE coefficients window

This program has helped to compare the commercial available TEG modules, especially in the low temperature gradient. Table 3.2 summarizes the main parameters of the two TEG modules selected. Both are developed by the same manufacturer, *Adaptive Power-Management*. (See ANNEX I Datasheet of the TE modules):

	MGM250-17-10-16	GM200-49-45-25
Useful surface	11.2 x 11.2mm	62 x 62mm
Output Power	0.42W	6.8W
Max. Temp. Grad.	+250°C	+150°C
Imax	600mA	6.8A
Vmax	1.4V	2.5V

Table 3.2 Manufacturer characteristics of the TE modules

These cells are made of Bi_2Te_3 and deliver the same output power at low temperature gradients, despite the fact that the larger module achieves a higher production rate.
The power curves obtained from the TEG calculator will be further discussed in the experimental evaluation of the design (Chapter 4).

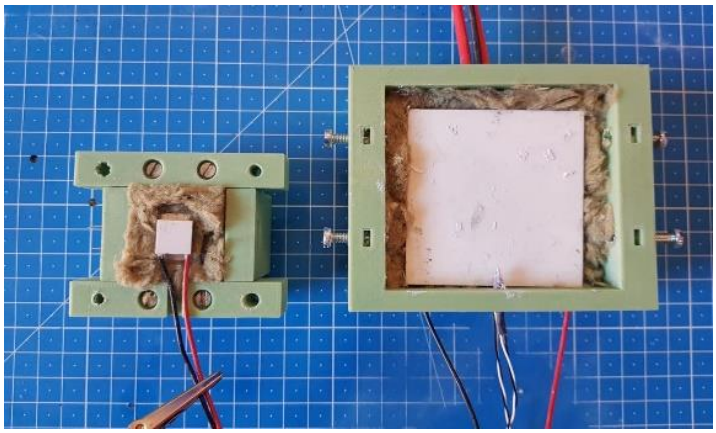

Figure 3.6 TE modules comparison. MGM250-17-10-16 (left) and GM200-49-45-25 (right)

Concentration mechanism

The concentration system is selected taking into account certain characteristics and requirements of the project, which are:

- The mechanism will have a manual dual-axis tracking of the sun path.
- Minimizing the reflection.
- Compactness (focal length as small as possible).

Back in section 2.1 two concentration mechanisms were analyzed: the Compound Parabolic Concentrator (CPC), and the Fresnel Lens.

CPC

This option is disregarded for the project due to the fact that the mechanism only uses direct radiation and not diffuse radiation. Moreover, the CPC has larger wind resistance and is prone to accumulation of dust [16].

Fresnel

Fresnel lenses are compact and require less maintenance. In addition, they allow easy adjustment of the concentration spot by varying its distance to the TE module. Moreover, Fresnel lenses are thin, what minimizes the material absorption. Thus, Fresnel lenses are chosen as the optical concentration system for the project.

The size ratio between both TEG modules is:

$$\frac{A^{62x62}}{A^{11.2x11.2}} = \frac{62x62}{11.2x11.2} \approx 30 \quad \textbf{(3.1)}$$

Thus, the concentration mechanism must belong to the medium concentration ratio (10 ~ 100 suns) group in order to establish a proper comparison between both systems.

Among the commercially available devices, the model FRP232(f=32mm) and FRP251 (f=51mm) from Thorlabs manufacturer (See Figure 3.7) are selected. These Fresnel lenses are able to work in the high-frequency radiation of the light spectrum (in the range 400 nm<λ<700 nm) (See Figure 3.8). On the other hand, these lenses belong to the category of medium concentration.

$$C_S = \frac{A_F}{A^{11.2x11.2}} = \frac{\frac{\pi}{4}(50.8mm)^2}{11.2x11.2} \approx 16 \text{ suns} \quad \textbf{(3.2)}$$

	FRP232	FRP251
Focal Length	32 mm	51mm
Focal Length Tolerance	±5%	±5%
Diameter	2" (50.8 mm)	2" (50.8 mm)
Thickness	1.5 mm (Nominal)	1.5 mm (Nominal)
Concentration ratio (for 11.2x11.2TEG)	16.15 suns	

Table 3.3 Characteristics of the Fresnel lenses

Figure 3.7 Fresnel lens FRP2xx by Thorlabs

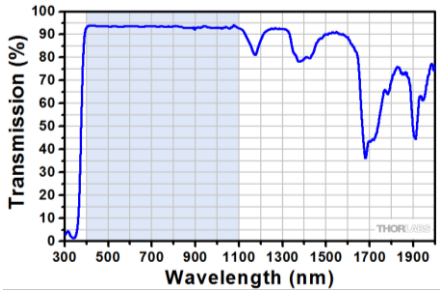

Figure 3.8 Percentage of light transmission - lenses FRP251 and FRP232 (source Thorlabs)

Heatsink

The heatsink plays a relevant role in the TEG design. It will enable the heat transmission from the hot side to the surrounding, thereby impacting the effectiveness of the TE cell as a power generator.

Before selecting the heatsink, a thermal simulation of each system (62x62 TE cell and 12x12TE cell + Solar Concentration) has been carried out. The purpose of this simulation is to evaluate the thermal gradient across the system.

TE62x62 module heatsink

The Aluminium 6061 heat sink 75x66x40mm by the manufacturer Fischer Elektronik has been subjected to the thermal simulation at outdoor conditions. The heat sink will have an embedded Pt1000 thermocouple for measuring its temperature.

Thermal analysis

The heatsink is simulated for the largest solar irradiation and the lowest dissipation. This is a possible situation when the solar irradiance is around of 1000W/m^2 and there is no wind.

The simulation is run in AutoDesk Fusion 360 under the following physical parameters and outdoor conditions:

- The heatsink thermal resistance $R_{heatsink}$=1.9K/W, according to the manufacturer.
- Solar irradiance of 1000W/m^2 is applied to the external upper surface of the TEG module. This is equal to an input heat of 3.844 W.
- Air temperature of 35ºC, according to the description of the operation range of section 3.1.
- There is heat evacuation by natural convection. Thus, the thermal convection coefficient h is estimated to be in the range 2~25[2] [W/m^{2}K] [85].
- There is heat transfer by radiation to the environment.

[2] For simplification purposes, it is assumed that the convection coefficient h is constant over the entire exchange surface

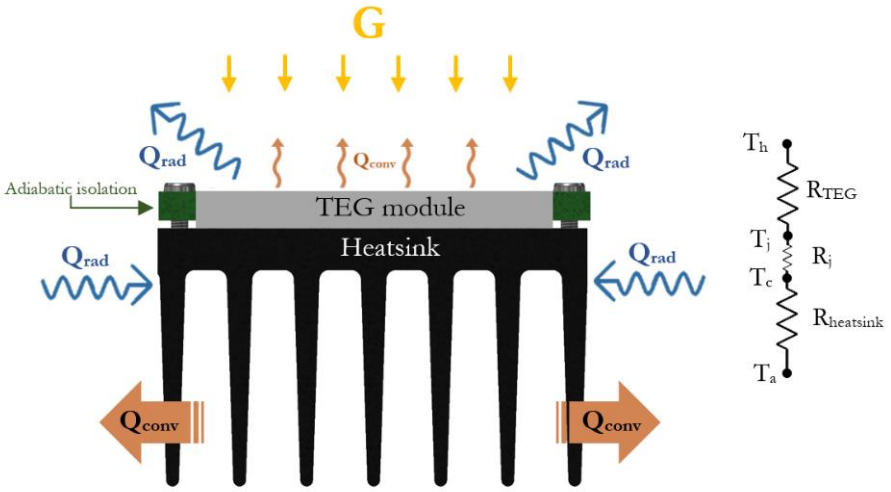

Figure 3.9 Diagram of the heat transfer across the 62x62 TE system

The simulation is for the steady-state of the system (dT/dt = 0), and the contact between the TEG module and the heatsink is perfect bounded[3]. The lateral surfaces of the TEG module are considered adiabatic[4].

For simplification purposes, the thermal junction between the TEG module and the heat sink is assumed to be perfect bounded.

$$R_j = 0 \qquad T_j = T_c \tag{3.3}$$

The thermal resistance R_{TEG}^{62x62} is calculated from the conductivity [5] of the TE cell from (2.13):

$$R_{TEG}^{62x62} = K^{-1} = \left(\kappa \frac{A}{dx}\right)^{-1} = \left(\kappa_p^{62x62} \frac{A_p^{62x62}}{L_p^{62x62}} + \kappa_n^{62x62} \frac{A_n^{62x62}}{L_n^{62x62}}\right)^{-1} \tag{3.4}$$

Where κ is the thermal conductivity of the TEG cell. According to the manufacturer:

$$\kappa_p^{62x62} = 0.0000361558 \times T_h^2 - 0.026351342 \times T_h + 6.22162 [W/mK] \tag{3.5}$$

$$\kappa_n^{62x62} = 0.0000334545 \times T_h^2 - 0.023350303 \times T_h + 5.606333 \, [W/mK] \tag{3.6}$$

[3] The actual system will not have perfect thermal contact, so thermal grease will be used to enhance heat transfer.
[4] The actual system will not have perfect heat isolation at its lateral surfaces. Due to the fact that these surfaces will be covered by PLA and their size is 20 times smaller than the hot side and the cold side of the TE cell, the lateral heat transfer is neglected.
[5] According to the manufacturer

Back to (3.4), Lp and Ln are the distance between the plates of the TE cell. Ap and An are the total surface of the p-type couples and the n-type couples, respectively.
In the case of the R_{TEG}^{62x62}:

$$L_p^{62x62} = L_n^{62x62} = 3\ mm \tag{3.7}$$

The cell has a fill-factor of 54%, what means that the semiconductor couples make up the 54% of the total surface of the TE cell. Thus:

$$A_p^{62x62} = fillfactor \times \frac{A^{62x62}}{2} = 0.54 \times \frac{62x62mm}{2} = 1037.88mm^2 \tag{3.8}$$

$$A_n^{62x62} = A_p^{62x62} = 1037.88mm^2 \tag{3.9}$$

In the simulation, the heat source is the solar irradiation. Due to the fact that this simulation is for the maximum achievable temperature, the spectral absorption component of the TEG module is set to 1 (black body).

From (3.5),(3.6), and (3.4) it can be noticed that the thermal resistance of the TEG module depends on the temperature and the temperature of the TEG module is unknown. Thus, the system is programmed for running iterative simulations for a parametric temperature. Once it has been explained all the parameters involved in the simulation, the final result is shown in Figure 3.10.

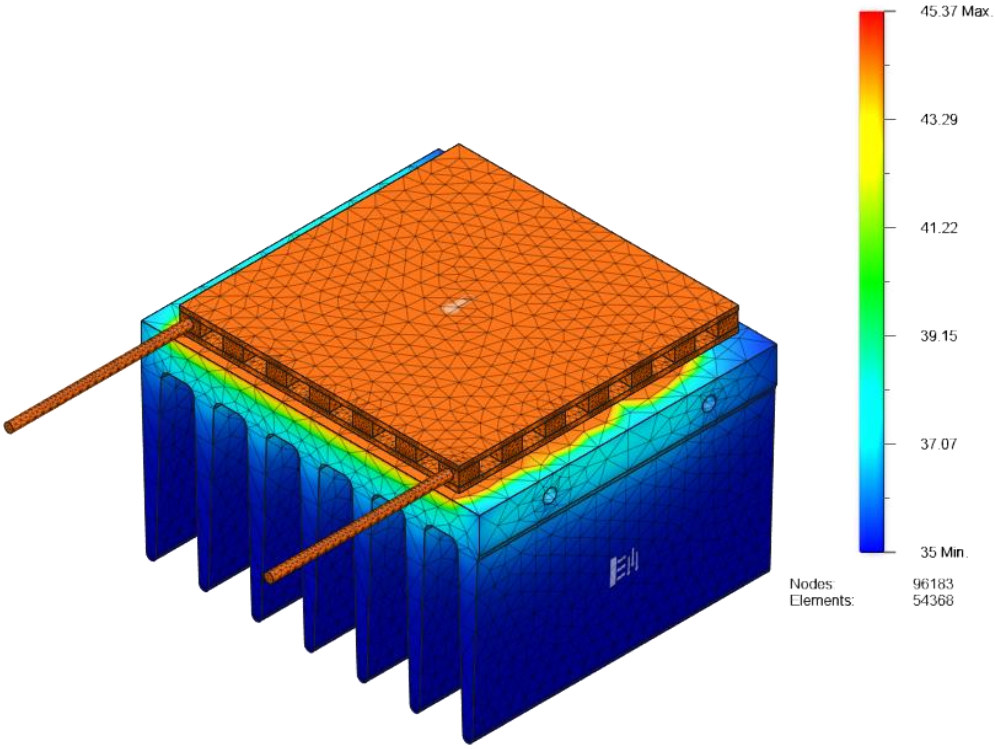

Figure 3.10 Thermal simulation of the 62x62 TEG system at outdoor conditions

Figure 3.10 shows the thermal analysis for a thermal convection coefficient h=2. The mesh has 96183 nodes, the max temperature is 45.37ºC and the minimum, 35ºC(ambient

temperature). The thermal gradient is 8.3ºC. According to the manufacturer, the output electrical power for this thermal gradient is 0.6mW.
The results for a wider range of thermal convection coefficients is shown in Table 3.4.

	h [W/m²K]					
	h=2	h=4	h=6	h=8	h=10	h=15
Th [ºC]	45.37	44.61	44.05	43.41	42.8	42
Tc [ºC]	37.07	36.92	36.71	36.62	36.4	36.1
ΔT [ºC]	8.3	7.69	7.34	6.79	6.4	5.9
MPP [mW][6]	0.62	0.7	0.54	0.52	0.5	0.46

Table 3.4 Thermal simulation of the 62x62TEG module - MPP depending on thermal convection coefficient

TE11.2x11.2 module heatsink

The same heatsink by Fischer Elektronik has been subjected to the thermal simulation for the 11.2x11.2 TEG module.

Thermal analysis

This thermal simulation is run under the same outdoor conditions:

- Heatsink thermal resistance $R_{heatsink}$=1.9K/W, according to the manufacturer.
- Solar irradiance of 1000W/m² is applied to the Fresnel lens. This means an input heat applied on the external upper surface of the TEG module, after concentration, of 2.03W.
- Air temperature of 35ºC, according to the description of the operation range of section 3.1.
- There is heat evacuation by natural convection.
- There is heat transfer by radiation to the environment.

The simulation is for the steady-state of the system (dT/dt = 0), and the contact between the TEG module and the heatsink is perfect bounded. The lateral surfaces of the TEG module are considered adiabatic.

[6] According to manufacturer's datasheet

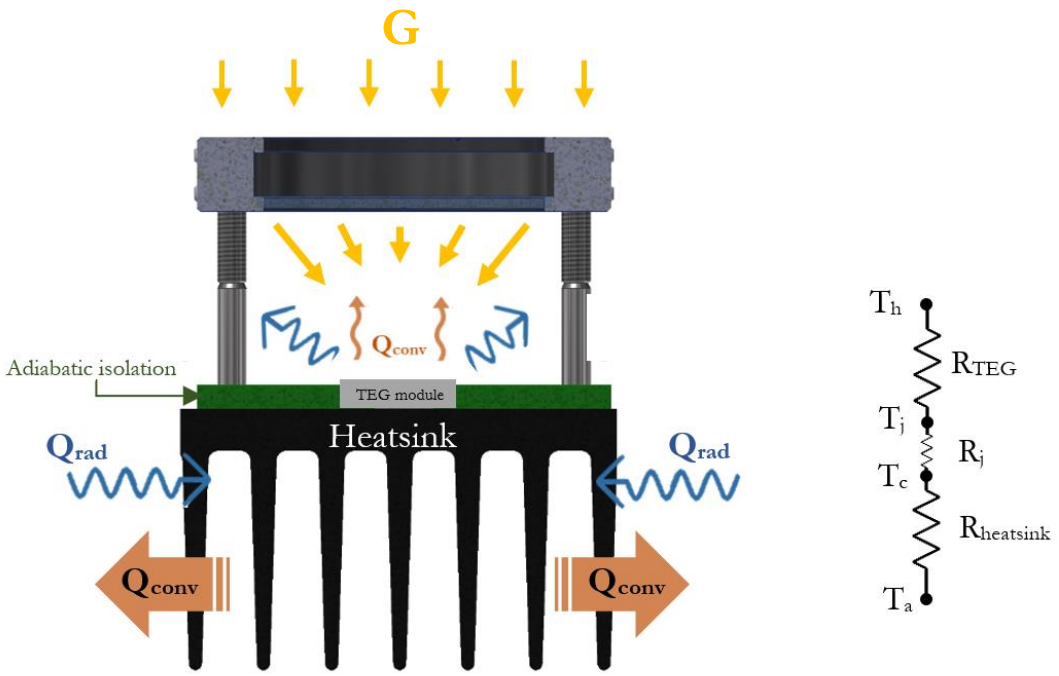

Figure 3.11 Diagram of the heat transfer across the 11.2x11.2 TE system

For simplification purposes, (3.3) is assumed. The thermal resistance $R_{TEG}^{11.2x11.2}$ is calculated as:

$$R_{TEG}^{11.2x11.2} = \left(\kappa_p^{11.2x11.2} \frac{A_p^{11.2x11.2}}{L_p^{11.2x11.2}} + \kappa_n^{11.2x11.2} \frac{A_n^{11.2x11.2}}{L_n^{11.2x11.2}} \right)^{-1} \quad \textbf{(3.10)}$$

According to the manufacturer, the 11.2x11.2TEG module has the same material thermal characteristics as the 62x62TEG. Thus:

$$\kappa^{11.2x11.2} = \kappa^{62x62} \quad \textbf{(3.11)}$$

In this case, $L_p^{11.2x11.2}$ and $L_n^{11.2x11.2}$:

$$L_p^{11.2x11.2} = L_n^{11.2x11.2} = 2.8 \text{ mm} \quad \textbf{(3.12)}$$

The cell has a fill-factor of 90%, what means that the semiconductor couples make up the 90% of the surface of the TE cell. Thus:

$$A_p^{11.2x11.2} = \text{fillfactor} \times \frac{A^{11.2x11.2}}{2} = 0.90 \times \frac{11.3x11.3mm}{2} = 57.47mm^2 \quad \textbf{(3.13)}$$

$$A_n^{11.2x11.2} = A_p^{11.2x11.2} = 57.47mm^2 \quad \textbf{(3.14)}$$

Once it has been explained all the parameters involved in the simulation, the final result is shown in Figure 3.12.

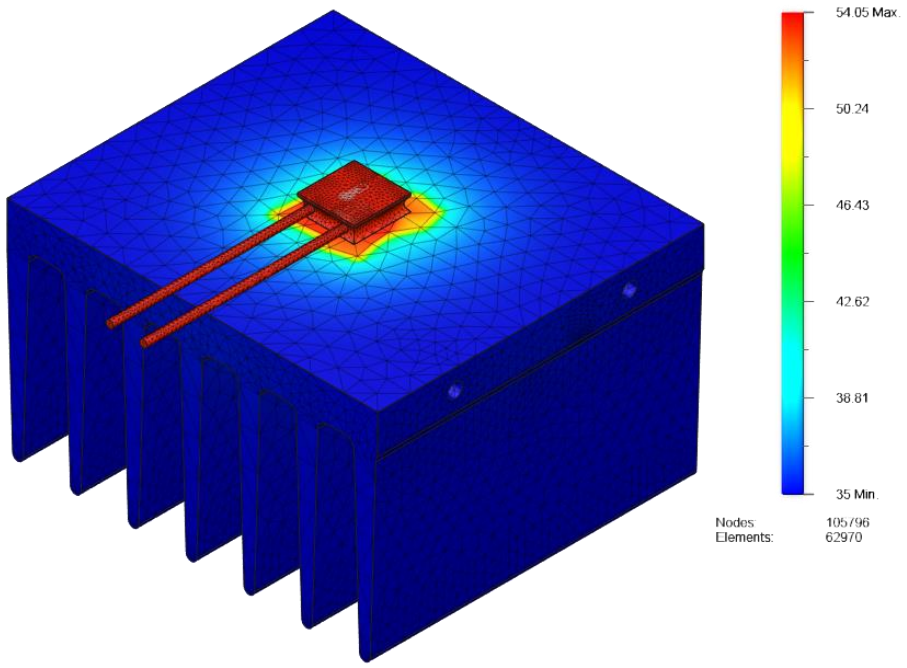

Figure 3.12 Thermal simulation of the 11.1x11.1 TEG system at outdoor conditions

The mesh has 105,796 nodes, the maximum temperature is 54.05ºC and the minimum, 35ºC (ambient temperature). The thermal gradient is around be 19.05ºC, 2.23 times larger than the 62x62TEG module. According to the manufacturer, a thermal gradient around 20ºC produces an output power of 5mW.

The results for a wider range of thermal convection coefficients is shown in Table 3.4.

	h [W/m²K]					
	h=2	h=4	h=6	h=8	h=10	h=15
Th [ºC]	54.05	53.3	51.75	49.34	48.7	46.8
Tc [ºC]	35	35	35	35	35	35
ΔT [ºC]	19.05	18.3	16.75	14.34	13.7	11.8
MPP [mW][7]	5.06	4.61	4.03	2.49	2.19	1.76

Table 3.5 Thermal simulation of the 11.2x11.2TEG module - MPP depending on thermal convection coefficient

[7] According to manufacturer's datasheet

Orientation mechanism

The sun position can be followed by adjusting two angles: the elevation above the horizon and the azimuth angle (See 3.4.1).

In this project, the position mechanism is manually oriented and it is imperative to have a precise register of the angle misalignment.
For this reason, a 2-axis goniometer of high precision is used. The model GN05 from Thorlabs is selected. This mechanism allows a fine adjustment of ±10ºC in the Y-axis and ±5ºC in the X-axis (Figure 3.13). For the coarse adjustment of the system, one-axis mechanism is used (Figure 3.14).

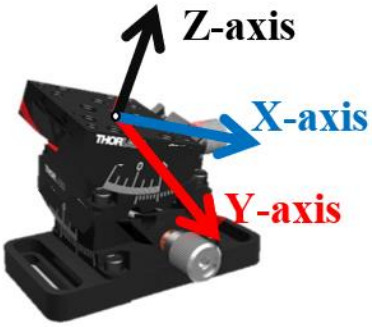

Figure 3.13 Fine 2-axis adjustment of angle - Goniometer GN Thorlabs

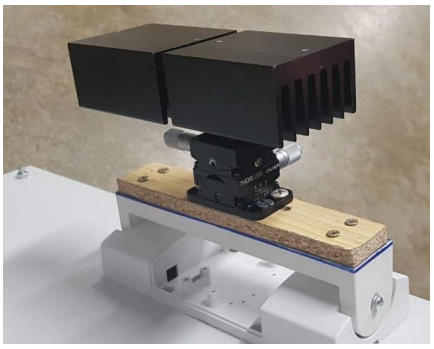

Figure 3.14 Positioning mechanism for outdoor testing

3.3. Improvement of the prototype design

The successive iterations of the outdoor model have brought performance improvements. Firstly, a high influence of the wind was observed on the cells. For preventing the heat dissipation due to the air convection over the TE module surfaces, a sheet of PMMA was suggested to be placed on the cells. However, the heat absorption of the material led to dismiss this idea. Instead, on the surrounding sides of both heatsinks a set of carboard sheets were set without shading the hot sides of the TE (Figure 3.15). As a result, the wind influenced was minimized.

Another improvement, and by all accounts the more far-reaching, was to increase the thermal absorptivity [8] of the TE modules.

[8] Absorptivity is the fraction of received irradiance that is absorbed by a body. The spectral absorptivity takes values between 0 and 1 (black body).

Figure 3.15 Cardboard sheets to reduce wind influence on the module

Thermal radiation is one of the three principal mechanisms of heat transfer, in addition to conduction and convection. The correlation among them is given by:

$$\alpha + \rho + \tau = 1 \tag{3.15}$$

where α stands for the spectral absorption (effectiveness in absorbing the incident radiant energy), ρ is the effectiveness in reflecting radiant energy, and τ represents the effectiveness in transmitting radiant energy.

An opaque body does not allow light to pass through it, which happens to be the case, and a black body absorbs all the radiation.

$$\tau = 0; \qquad \alpha + \rho = 1 \tag{3.16}$$

Thus, a thin coating of matt black special paint able to withstand high temperatures up to 300ºC was applied over the cells to provide high radiation absorptivity and low radiative emittance (Figure 3.16 and Figure 3.17). This improvement increased significantly the heat flux across the TE modules, and so, the power generation.

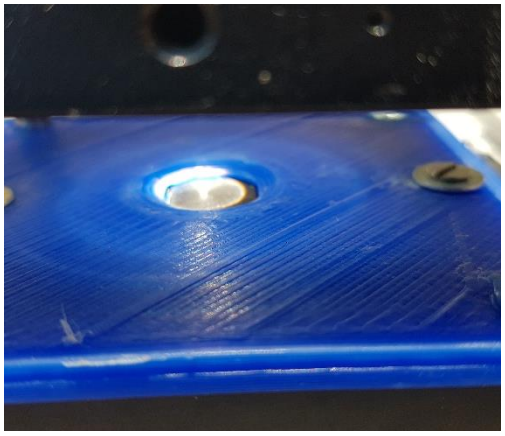

Figure 3.16 Black-painted 11.2x11.2 TE module

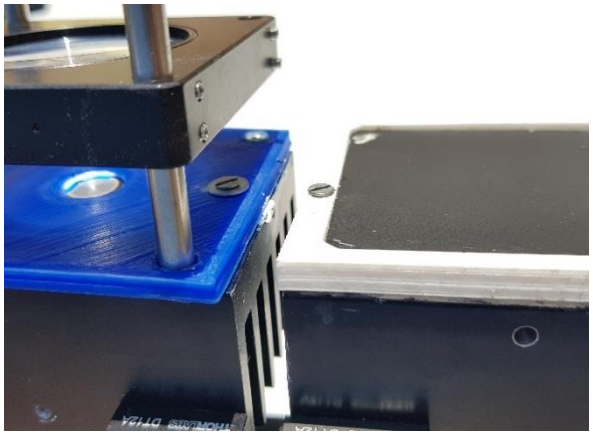

Figure 3.17 Black-painted TE modules

Another matter of fact is the accuracy when following the sun position. Moreover, a high angle deviation reduces significantly the heat transfer. For minimising the influence of

the solar position deviation on the power generation, a second Fresnel lens of a lower focal length was tested. By doing so, the distance between the lens and the TE module was reduced.

Although this modification effectively reduced the influence of the solar position, the output power peak was also reduced. This topic will be further discussed in the next chapter.

3.4. Design of the power electronics circuit and energy storage system

The power electronics circuit needed for the concentrating 11.2x11.2 TEG system is designed taken into consideration the experimental results from the laboratory tests (4.2) and the outdoor tests (4.4). A typical TEG-based source consists of the TEG stage, the power converter, and the storage stage, as Figure 3.18 shows.

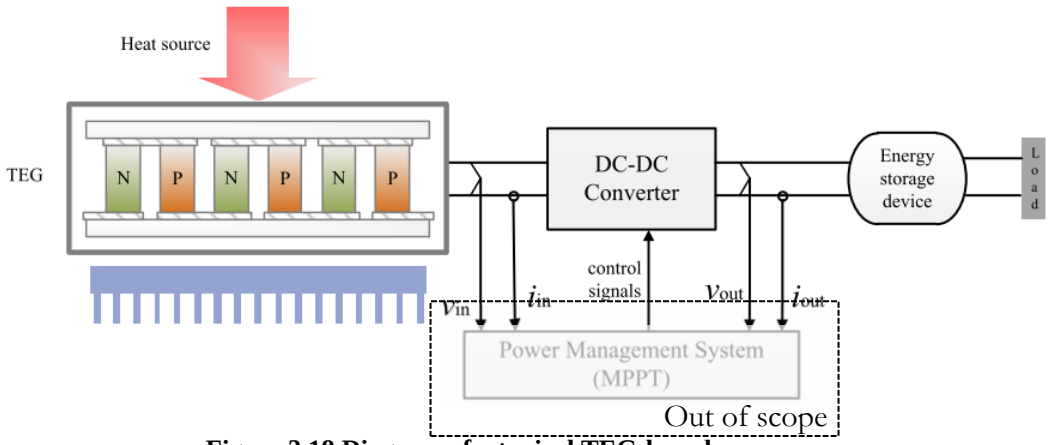

Figure 3.18 Diagram of a typical TEG-based source

The first approach of this section was to design the DC-DC power converter for a single TE module from scratch. However, this option was discarded as the magnitude of the maximum output power obtained at the outdoor tests was between 0.5 and 1mW. The desired voltage for the battery stage is 1V, what excels the achievable conversion ratio.

In this scenario, a DC-DC power converter for ultra-low power conversion has been selected and modified according to the characteristics of the TEG system designed. This option allows to adjust the DC-DC converter to a larger concentrating TEG system, in case of working with a higher number of TE modules.

After consulting the available options, the device selected is the STEVAL-ISV020V1 [86] whose schematic circuit can be seen in ANNEX V STMicroelectronics Evaluation Board – modified Schematic. It is an evaluation board based on buck-boost topology suitable for battery charging applications.

The board is optimized for harvesting energy from TEG in the range of:

$$1V < V < 2V \text{ and } 10\mu A < I < 20mA.$$

Thus, the following changes have been made in the board components in order to adapt the device to the designed TEG system.

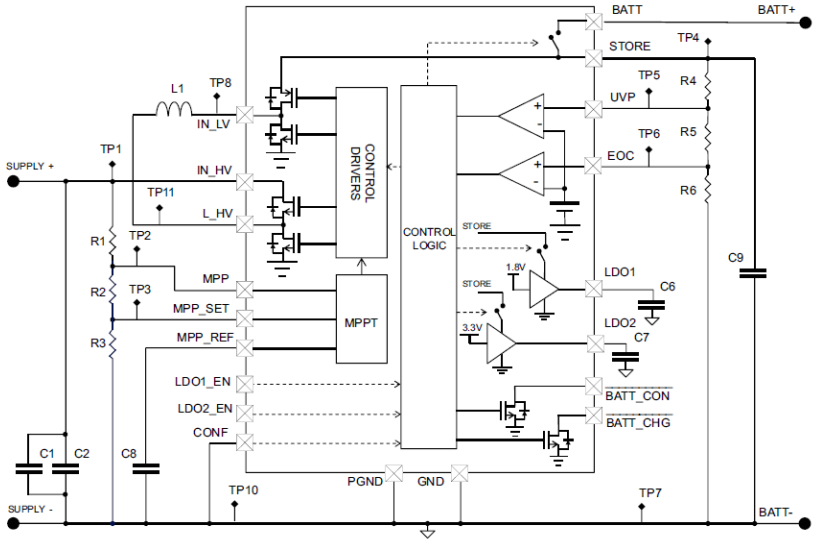

Figure 3.19 STEVAL-ISV020V1 application diagram

MPPT of the controller

As previously mentioned, the maximum power production if achieved when matched-load condition is fulfilled.

The evaluation tests demonstrated that, in the working range, the matched-load resistance variation is low enough (<8% deviation between 750W/m^2 and 1050W/m^2) to dispense with the MPPT (See Figure 4.21). This decision saves power consumption in the device and increases the overall production efficiency.
The MPPT function is therefore disabled by pulling up the pin MPP-SET and unsoldering the resistor R2.

Internal and optimal resistance

As far as the designed is concerned, the assumption of constant temperature at both sides of the TEG module is made. By doing so, the steady-state electrical parameters can be simplified to a DC voltage source VOC in series with an internal resistance $r_{TEG.}$ From equation 2.25:

$$r_{TEG} = \frac{\alpha \cdot \Delta T}{I} + R_{load} \quad \textbf{(3.17)}$$

According to the obtained results;

$$r_{TEG} = \frac{1.5x10^{-6} \quad 54.4-35}{17.17x10^{-3}} + 0.19 \;=\; 0.214\ \Omega \quad \textbf{(3.18)}$$

In order to achieve the matched-load resistance, a variable resistor is connected in series with the thermoelectric generator. Measuring the internal impedance of the TEG allows to adjust the variable resistor until a value of 0.214Ω is set. In practice, the voltage drop in the variable resistor R is negligible and MPP is virtually achieved.

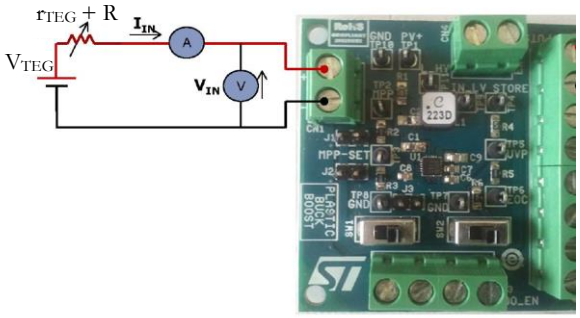

Figure 3.20 TEG module connection to the DC-DC converter

Input capacitance

Every 16 seconds (typical value) the SPV1050 device stops switching for 400 ms. During this time frame the input capacitor C1 is charged up to V_{OC} by the source according to the time constant T1, which depends both on its capacitance and on the equivalent resistance of the converter, which is:

$$C1 \;\leq\; \frac{T1}{R_{EQ}} \;=\; \frac{400x10^{-3}}{50x10^{3}} \;=\; 8\mu F \quad \textbf{(3.19)}$$

The SPV1050 performances might be further improved by reducing the time constant (e.g. reducing input capacitance) at very low input power:

$$C1 \;=\; 4.7\mu F \quad \textbf{(3.20)}$$

The rest of the elements are selected according to manufacturer's recommendations:

$$C8 \;=\; 10\ nF \quad \textbf{(3.21)}$$

Inductor selection

The SPV1050 device controls the switching of the integrated DC-DC by limiting the peak current flowing through the inductor L1. The lower is the series resistance of the selected inductor, the lower is its DC loss. The most typical magnitude for the TEG power range, according to the datasheet, is selected.

$$L1 = 22\mu H \tag{3.22}$$

Undervoltage protection and end-of-charge protection

The board includes a bus for controlling the output of the battery, however, the lowest battery voltage that this bus can handle is 1.23V(internal voltage reference set).

Thus, the output of the DC-DC converter is connected to a separate charge stage circuit. It has two purposes. Firstly, controlling the power flow from the converter to the battery, and not the other way around. In addition, this circuit disconnects the battery when it is fully charged for protecting the device. Secondly, it shows the state of the battery (charging or fully charged) by means of two LEDs. The schematic of this circuit is included in ANNEX VI Charge stage schematic.

3.4.1. Energy consumption estimation of the linear actuator

The last stage of the circuit is the battery. Its purpose is to supply auxiliary equipment of the PV system. For instance, the linear actuator of the solar tracker. Thus, its power capacity has been stablished on the basis of the linear actuator used in the Project SolarG. Firstly, the angle sweep is calculated. Then, the required electric power is determined.

System characteristics

The solar tracker mechanism used in the project SolarG is a linear actuator of 12 VDC and maximum push-force of 6000N . The system has the following characteristics:

- The system is a one-axis solar tracker with fixed azimuth angle.
- Maximum panel sweep angle of $\pm 45^{o}$ (0^{o} is the horizontal line with respect to the ground).
- The load of the system is 20% the maximum electrical power of the actuator, according to measures done in the field.

Calculation of the daily angle sweep

The daily working time is determined by the sun path and the daylight duration. For instance, in the month of July there are 14hours of sunlight, however, some of these hours have low solar irradiation (ANNEX VIII Sun path and solar irradiation).
For this estimation, only hours whose irradiation is over 800W/m^2 are considered. Thus, each day has 8 hours (from 9:00h until 17:00h) of solar tracking.

The following calculation of the angle sweep is carried out according to the consulted literature [87].

First, the tracking rotation angle at 9:00h and 17:00h is calculated. According to the European Centre for Weather Forecasts (ECWF) data [88]:

$$\beta_s^{\,9} = 21.67^{\circ} \qquad \gamma_s^{\,9} = 79.68^{\circ} \tag{3.23}$$

$$\beta_s^{\,17} = 49.84^{\circ} \qquad \gamma_s^{\,17} = 254.49^{\circ} \tag{3.24}$$

Where:

β_t	Tilt angle of inclination of the tracker above the horizon
β_s	Solar elevation angle above the horizon [0~+90º]
γ_t	Azimuth angle of the tracker
γ_s	Solar azimuth angle [0~+360º]
9 & 17	9:00h and 17:00h, respectively.

All these angles are referred to the cardinal points as it can be seen Figure 3.21.

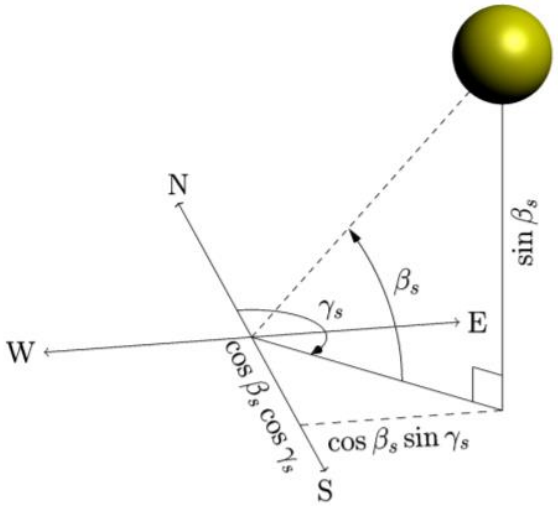

Figure 3.21 Solar position angles and their projections

The cartesian projection to the tracker coordinate system is:

$$\begin{bmatrix} S_x \\ S_y \\ S_z \end{bmatrix} = \begin{bmatrix} \cos\beta_s \sin\gamma_s \\ \cos\beta_s \cos\gamma_s \\ \sin\beta_s \end{bmatrix} \quad \textbf{(3.25)}$$

Where $S\ x, y, z$ are the cartesian coordinates of the tracker coordinate system. In addition, the PV panel is mounted with the following angles:

$$\beta_t = 0^{\circ} \qquad \gamma_t = 91.31^{\circ} \quad \textbf{(3.26)}$$

The elevation angle is equal to zero because its reference position is parallel to the ground (0º). If we apply the transformation matrix to project the solar coordinates into the tracker coordinate system:

$$\begin{bmatrix} S'_x \\ S'_y \\ S'_z \end{bmatrix} = \begin{bmatrix} s_x cos(\gamma_t) - s_y sin\ \gamma_s \\ s_x sin(\gamma_t)cos(\beta_t) + s_y cos(\beta_t)cos(\gamma_t) - s_z sin(\beta_t) \\ s_x sin(\gamma_t)sin(\beta_t) + s_y sin(\beta_t)cos(\gamma_t) + s_z cos(\beta_t) \end{bmatrix} \quad \textbf{(3.27)}$$

Where are the projected solar coordinates into the tracker coordinate system. Now the tracking rotation angle around the rotating axis ty of the PV panel (See Figure 3.22)

$$\theta_T = \text{atan2}\ S'_x, S'_z \quad \textbf{(3.28)}$$

Where $\theta_T\ [\text{degrees}]$ is the tracking rotation angle. In other words, the angle deviation from the referential rotation plane [-45º ~ +45º]

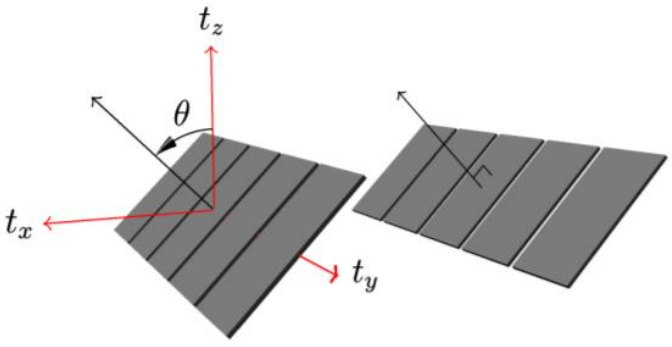

Figure 3.22 Tracking rotation angle

Applying equation (3.23),(3.24),(3.25),(3.26),(3.27), and (3.28)the tracking rotation angles at 9:00h and at 17:00h are:

$$\theta_T^9 = -26.90^{\circ} \approx -27^{\circ} \quad \textbf{(3.29)}$$

$$\theta_T^{17} = +13.72^{\circ} \approx +14^{\circ} \quad \textbf{(3.30)}$$

Once it has been calculated the initial and final positions of the PV panel, the daily sweep angle for tracking the sun and coming back to the initial position afterwards is:

$$\text{daily sweep} = 2 \times \ |\theta_T^9| + |\theta_T^{17}| \ = \ 2 \times 41^o/\text{day} \quad \textbf{(3.31)}$$

Estimation of power consumption

The calculations of this section have been obtained from the consulted literature [89].

A. Power consumed during the sun tracking displacement

Time: 8 hours
Angle sweep: 41º
Angle velocity: 41º/8h ≈ 6º/h

If the solar tracker rotates 6º every hour, the controller can set three rotations of 2º per hour. If each correction of 2º in the orientation takes 3 se c, it accounts to 6 seconds of working time per hour. Then, the linear actuator operates for a total of 48s per day for tracking the sun.

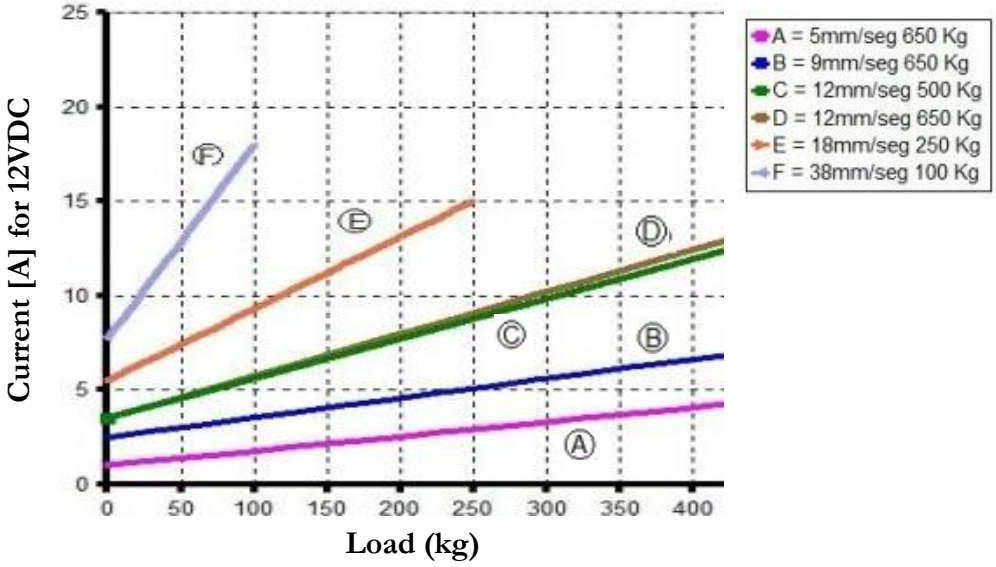

Figure 3.23 Power consumption of the linear-actuator

Taking into account the previous consideration of working at 20% of the maximum power:

$$E = 20\% \ \cdot V \ \cdot I \ \cdot t \quad \textbf{(3.32)}$$

$$E_{tracking} \ = \ 20\% \ \cdot 12 \ \cdot 4 \ \cdot 48 \ = \ 460.8 \ [J] \ = \ 0.13 \ [Wh] \quad \textbf{(3.33)}$$

B. Power consumed for returning to the initial position

Due to the fact that the linear actuator only operates at 5mm/s, the return movement lasts the same time: 48 s. Therefore:

$$E_{return} = E_{tracking} = 0.13\ [Wh] \tag{3.34}$$

Thus:

$$\boxed{E_{day} = E_{tracking} + E_{return} = 0.26\ Wh/day} \tag{3.35}$$

The capacity of a battery able to supply 0.26Wh at 12V is equal to 21.67mAh. The DC-DC converter cannot boost the output power until 12V, thus the battery voltage is set at 1V. If the 0.26Wh are supplied at 1V, the capacity increase up to 260mAh.

The lead acid battery of 260mAh and 1V from the manufacturer Yuasa is selected according to these requirements. For powering the linear actuator at 12V, a second DC-DC power converter would be required, yet the power needed would be available at the battery stage.

A battery may be recharged using either a constant voltage charger or a constant current charger, or a modification of either or both of these. The exact regime chosen generally depends upon the time and economic constraints imposed by the system. Constant current charging is widely used in cyclic applications where a recharge must be accomplished in a relatively short time period. Constant voltage charging, where a single voltage level is applied across the battery terminals, is the most suitable method to recharge the selected lead battery.

3.5. Data Acquisition system

Laboratory data acquisition system

The laboratory setup is introduced in section 4.1. An acquisition program has been designed with the software NI LabVIEW 2021 for measuring the TEG output power and all the temperatures involved. The data acquisition board for the tests was the USB6211 by the manufacturer National Instruments.

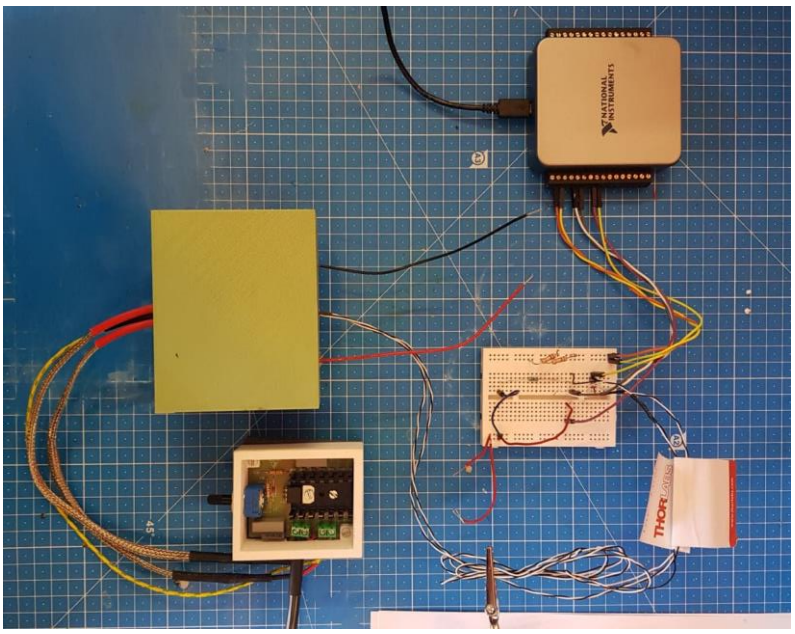

Figure 3.24 Testing setup of GM200-49-45-25 with DAQ

The NI USB6211 is a multifunction USB board with 16 analog inputs of 16 Bits, 250k samples per second, and a resolution of 0.3mV. It measures up to ±10V, high enough for our system.

The acquisition time of the DAQ is set according to the thermal steady-state of each TEG system. For determining so, the laboratory system was tested starting from the ambient temperature until the steady-state (dT/dt=0). This analysis also allows to better the quality of the designed heat insulator.
As it will be further demonstrated, the time needed for reaching the steady-state was found to be 7min at the 11.2x11.2TEG and 10min for the 62x62TEG module.

The data obtained in the tests contain some outliers and unknown disturbances. For partially solving the latter issue, a low-pass filter was included in the acquisition circuit in order to remove the harmonics multiplies of 50Hz. When it comes to the former issue, curve fitting techniques have been applied to the data. Further information regarding this methodology is explained in ANNEX VII Curve Fitting with MATLAB.

Outdoor measurements and data acquisition system

In this occasion, the power production measurements of the solar position tests were carried out using two multimeters, as shown in Figure 3.25. For determining the optimal load of the system during the tests (below 1Ω), a high precision measuring instrument was used instead of the multimeters.
The charge test is made with the data acquisition board previously used at the lab tests.

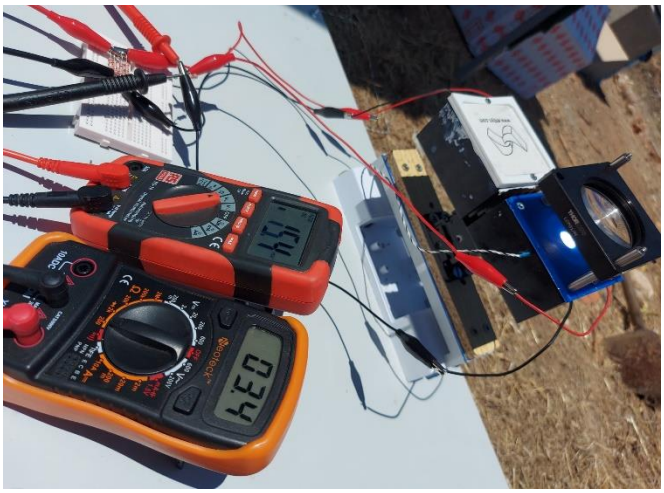

Figure 3.25 Measurements during solar position test

The instrument 405i by Testo manufacturer is used for ambient temperature and wind speed measurements. The temperature is measured by means of a NTC with a resolution of 0.1 ºC and a tolerance of ±0.5 ºC, and the wind measurements have a resolution of 0.01 m/s and a tolerance of ±(0,1 m/s + 5% wind average).

The solar calibrated sensor No1003001 by ATERSA is used for the solar irradiation measurements, as commented in section 3.1. This device is able to operate in the range of 0~1,250W/m^2 with an intrinsic error of ±0.2%. It has to be mentioned that this instrument was fixed to the PV structure of SolarG installations. Thus, it did not measure perpendicular incident radiation because there is a orientation deviation that increases throughout the day. The solar irradiance values registered at the tests might have slightly lower values than actual ones. To cope with this, the historical meteorological record [84] has been consulted in order to cross-check the results.

Once the results had concluded, no significant differences were observe between the meteorological forecast (solar irradiation, outdoor temperature, and speed wind) and the registered values on site. As far as the solar irradiation is concerned, the maximum level registered was 1050W/m^2 between 13:00h and 15:00h, which is in line with the consulted sources.

Chapter 4

Experimental evaluation of the design

Like the star that shines afar.
Without haste.
Without rest.

Goethe

4.1. Laboratory test setup

The purpose of this verification is to test the performance of the TE under controlled working conditions. These analysis draw a better understanding of the system before the outdoor implementation.

Assembly of the laboratory setup

Figure 4.1 shows the laboratory setup for evaluating the 62x62TEG. Its function is to direct the heat flux across the TEG module. All the components are housed inside of a PLA heat insulator lined with mineral wool with small holes for the wires.

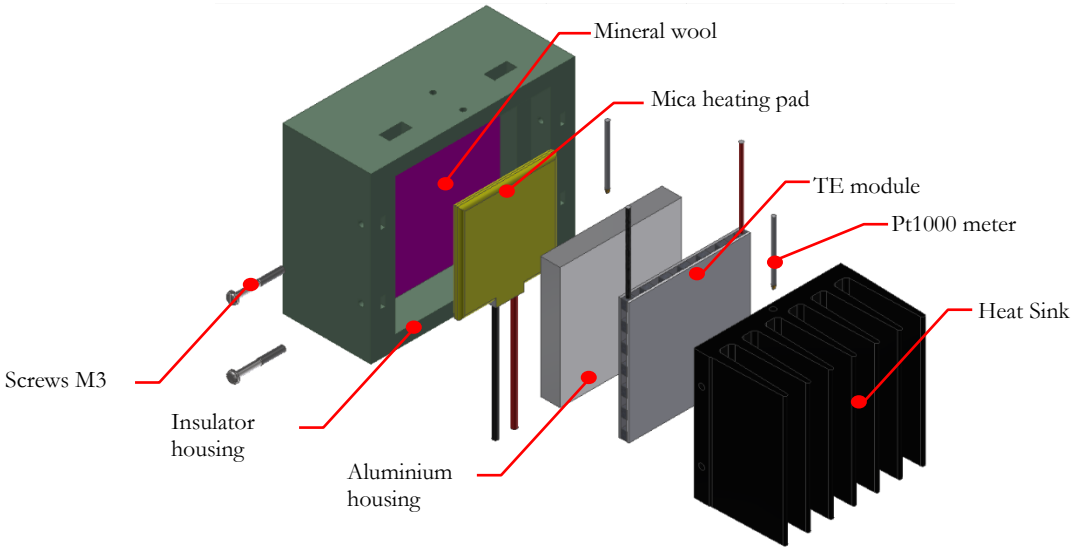

Figure 4.1 CAD model for lab testing of the GM200-49-45-25

A mica heating pad was chosen as regulated heat source. This device is embedded in an aluminium housing custom made for fitting the dimensions of the TE module and conducting the heat (Figure 4.2).

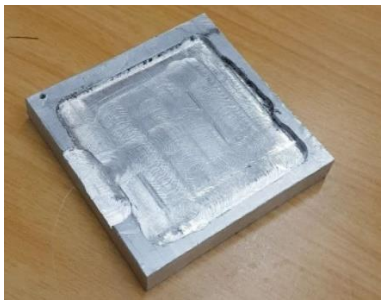

Figure 4.2 Aluminium socket for housing mica heating pad for the laboratory thermal tests

The whole system is screwed to the heatsink. The compression force guarantees the heat transfer. There are two Pt1000[9] at both the hot and cold sides for measuring the temperatures during the tests.

For the 11.2x11.2 TEG module (Figure 4.3), the heat source is a thermal resistance load. As previously outlined, the heat source will be approximately 2W. Therefore, two resistors connected in series are set to deliver 2W. A special aluminium piece houses these two resistors and is in direct contact with the TE module.

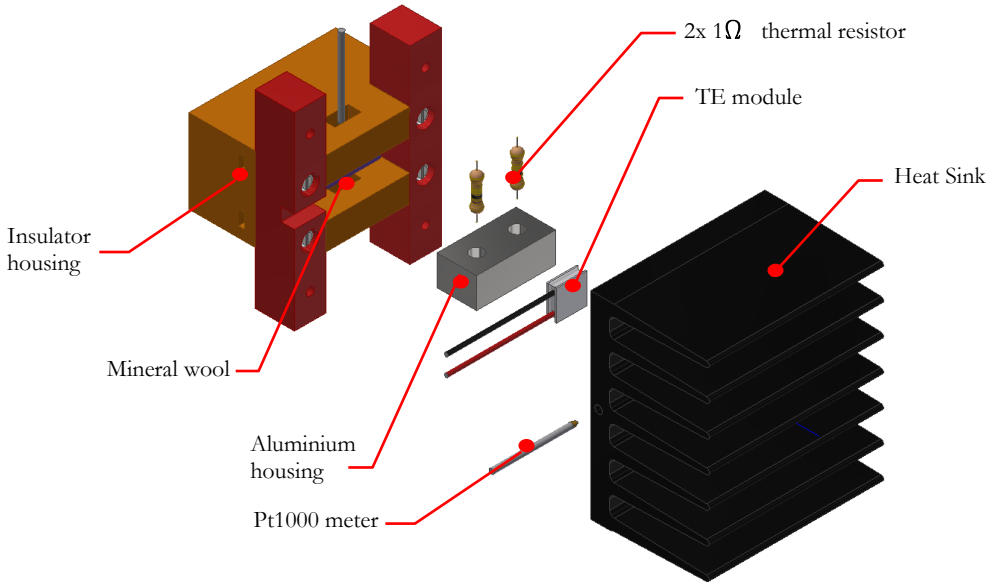

Figure 4.3 CAD model for lab testing of the MGM250-17-10-16

[9] A Pt1000 is a type of RTD that operates as a temperature sensor. Its electrical resistance varies with the temperature level and gives a resistance of 1000Ω at 0° C. Their values are standardized according to UNE-EN 60751:2008 [70].

All the components are housed by a PLA insulator with holes for all the wires. Its inside is lined with mineral wool, so is the 62x62 insulator. This setup includes two Pt1000 for measuring the temperatures during the tests too. The whole system is screwed to the heatsink and the compression force guarantees a proper heat transfer.

All the thermal junctions include thermal grease due to its ability to fill any microscopic roughness at the surface and its high thermal conductivity. By doing so, the air gap between surfaces is reduced and ensures the heat transfer. This grease has been applied following the manufacturer instructions [90].
Figures 4.5 to 4.8 depicts the actual setup of the testing system.

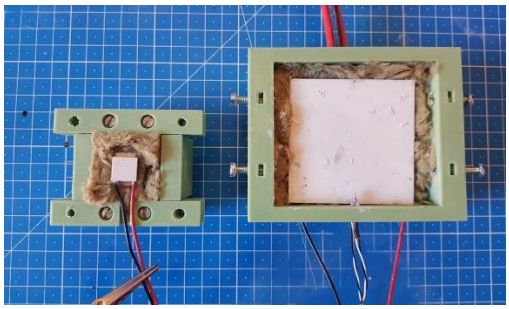

Figure 4.4 Heat insulator comparison. Cross-section view

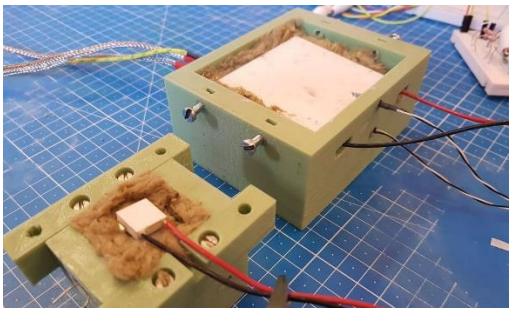

Figure 4.5 Heat insulator comparison. Overview

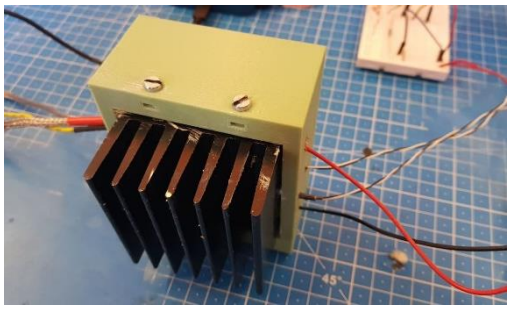

Figure 4.6 Testing setup of GM200-49-45-25 with heatsink

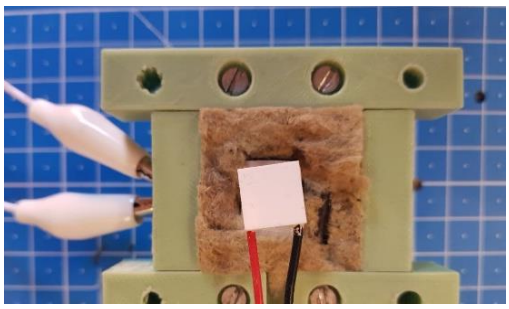

Figure 4.7 Testing setup of MGM250-17-10-16 without heatsink

Test procedure of the laboratory tests

The tests consisted of gradually increasing the heat flow at controlled intervals to attain quasi-steady conditions. Both TEG modules were tested under a temperature gradient between 0ºC and 60ºC. The temperature of the heatsink was kept constant around 25~ 30 ºC. By doing so, the results can be compared to those provided by the manufacturer, which offers its own test results for a constant cold side of 30ºC.

During the test, the temperature of all the outer faces of the heat insulator were measured for a EMS of 0.95 (emissivity of the PLA). This helped to improve thermal insulation by reinforcing those areas that reached the highest temperatures.

Between each test, there is a minimum separation of 1 hour that allows the whole system to return to the room temperature.

The open-circuit voltage test was made without any load. It allows us to obtain the Seebeck coefficient according to equation (3.2). The output power test was made for the optimal load.

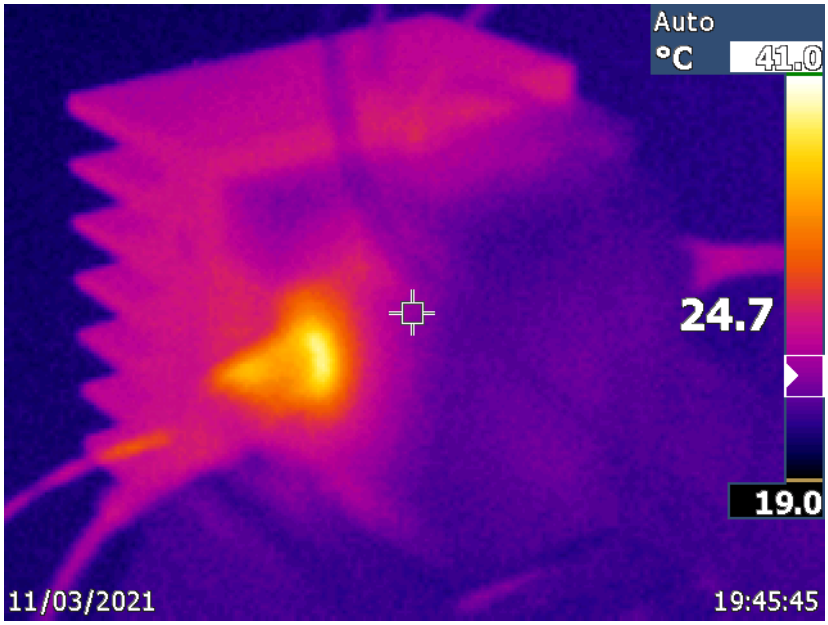

Figure 4.8 Thermal photograph of the MGM250-17-10-16 module insulator during power generation test

4.2. Results and discussion of the laboratory tests

The experimental verification of the TE modules allowed to test each device at specific working conditions. Even though the heat insulator designed is not adiabatic, the desired temperatures were achieved.

Thermal steady-state for the laboratory setup

The results from the test described in last section are shown in Figure 4.9. The 11.2x11.2 TEG lasts 7min to reach the ±5% range of the steady-state (dT/dt=0) and it takes 10min for the 62x62 TE module. Taken into account this information, the sample time of the acquisition program was set to take 30sec straight of measurements every 7 and 10min, respectively.

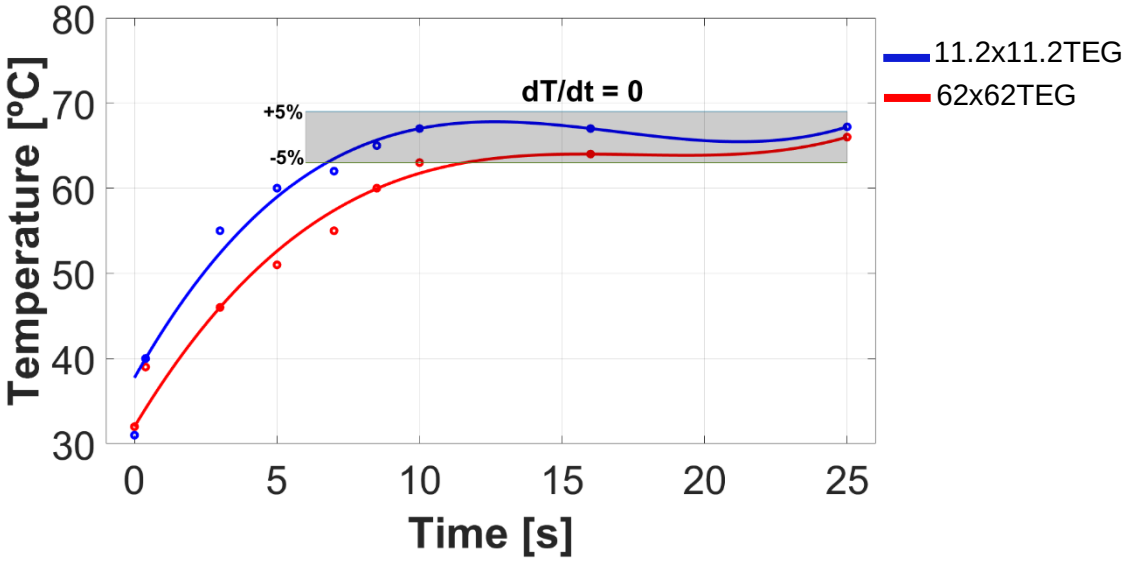

Figure 4.9 Time needed to reach the thermal steady-state

Maximum power curve characterisation and optimal load

TE62x62

The results of the MPP curve are shown in Figure 4.10 a). A detailed zoom for the lower temperature range (where the module is expected to operate in outdoor conditions) is also included in Figure 4.10 b).

An output power around 1mW was achieved for the expected outdoor conditions. The result fits the expected values offered by the manufactured for the whole temperature range and the maximum deviation from the fitted curve is lower than 10%. The results obtained from the TEG calculator are also plotted. Even though this latter curve follows the same trend, the simulated curve is slightly higher along the entire range, especially in

the zone close to the zero gradient. This may be due to the simplifications made during the simulations, such as constant matched-load or constant cold side temperature.

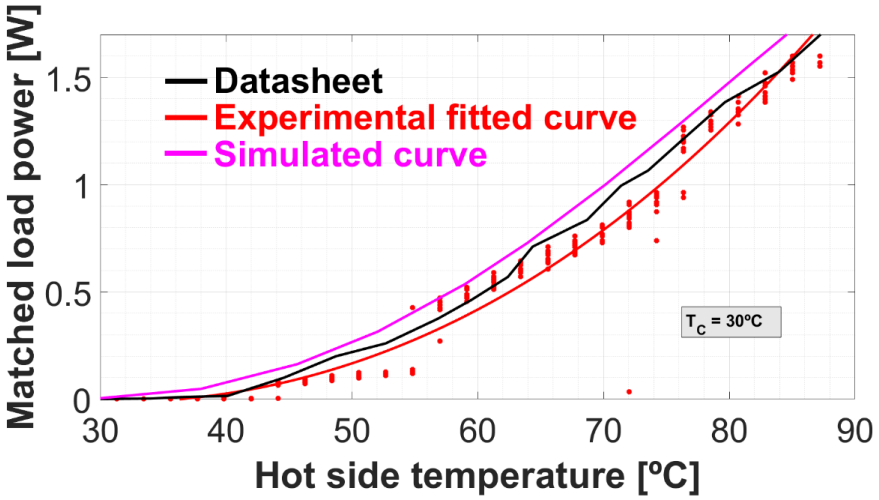

a) 30ºC < Tc < 90ºC

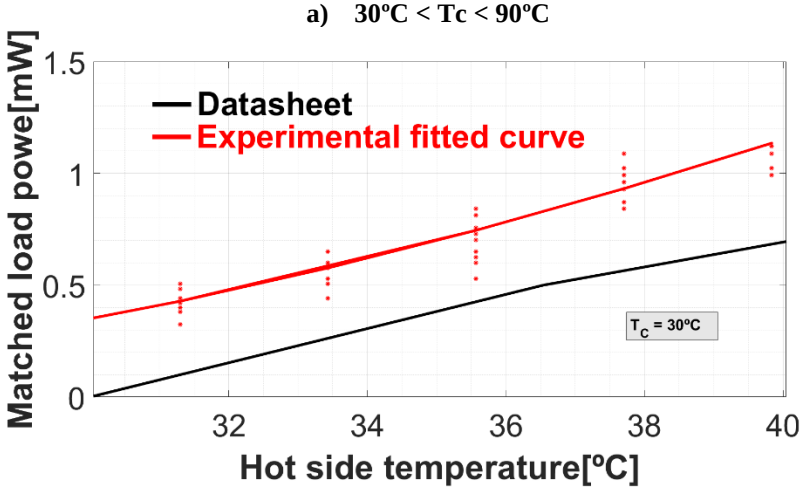

b) Detail view for the range 30ºC < Tc < 40ºC

Figure 4.10 Matched-load power graph - 62x62 TE module

It can be noticed from equations (3.17) and (3.19) that the internal resistance of each TE module depends on temperature. Thus, the matched load tests required a changing load resistance so as to follow the MPP. As a result, the optimal load for each interval has been determined, information that has been applied to the design of the DC-DC convert.

The matched load resistance changes throughout the temperature range. For tracking the MPP curve, the load was adjusted for reaching the maximum output power every 5ºC. The final values have been registered in Table 4.1. There are no significant differences.

	30 <Th< 45 ºC	45 <Th< 55 ºC	55 <Th< 75 ºC	75 <Th< 90 ºC
Manufacturer matched R_L	0.16Ω	0.165Ω	0.17Ω	0.175Ω
Experimental matched R_L	0.12Ω	0.13Ω	0.15Ω	0.18Ω

Table 4.1 Experimental matched load resistance for 62x62TE at Tc=30ºC

Taken into account the results, the MPP curve has been modelled for a Th given in [ºC] and Tc = 30ºC. The error of the experimental fitted model is shown in Table 4.2.

$$P_{MPP}^{62x62} = 1.668 \cdot 10^{-6} \times Th^3 + 3.015 \cdot 10^{-4} \times Th^2 - 0.02323 \times Th + 0.366 \quad \textbf{(4.1)}$$

SSE	R-square	Adjusted R-square	RMSE
0.07311	0.9945	0.9945	0.01016

Table 4.2 Error of the experimental fitted MPP curve of 62x62 TE power module

TE11.2x11.2

The results of the MPP curve are shown in Figure 4.11 a). It can be seen in Figure 4.11 b) that both TE modules share the same power range at low temperatures, what ensures a proper comparison of their performance for the outdoor tests.

This TE module is designed for a higher thermal gradient, however an output power around 2mW was achieved for outdoor conditions. The result fits the expected values offered by the manufactured for the whole temperature range and the maximum deviation from the experimental curve is lower than 5%.

The match load values have been registered in Table 4.3. In this case, there is a deviation from the expected values. This can be caused for the cold side temperature, which is being

	30 <Th< 45 ºC	45 <Th< 55 ºC	55 <Th< 75 ºC	75 <Th< 90 ºC
Manufacturer matched R_L	0.56Ω	0.65Ω	0.70Ω	0.77Ω
Experimental matched R_L	0.30Ω	0.40Ω	0.50Ω	0.70Ω

Table 4.3 Experimental matched load resistance for 11.2x11.2TEG at Tc=30ºC

heated from 25ºC until 30ºC. The curve of the manufacturer is for a constant Tc = 30ºC. That explains why the matched load deviation is lower for high temperatures, where the heatsink is closer to 30ºC.

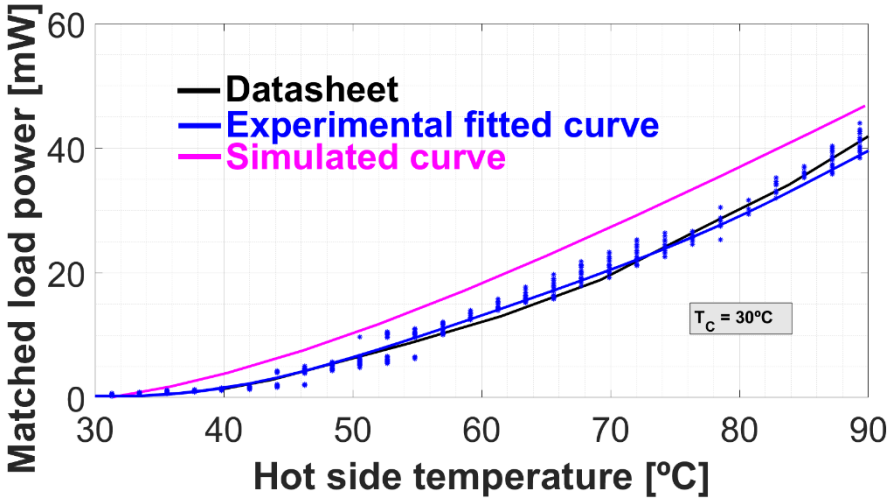

a) 30ºC < Tc < 90ºC

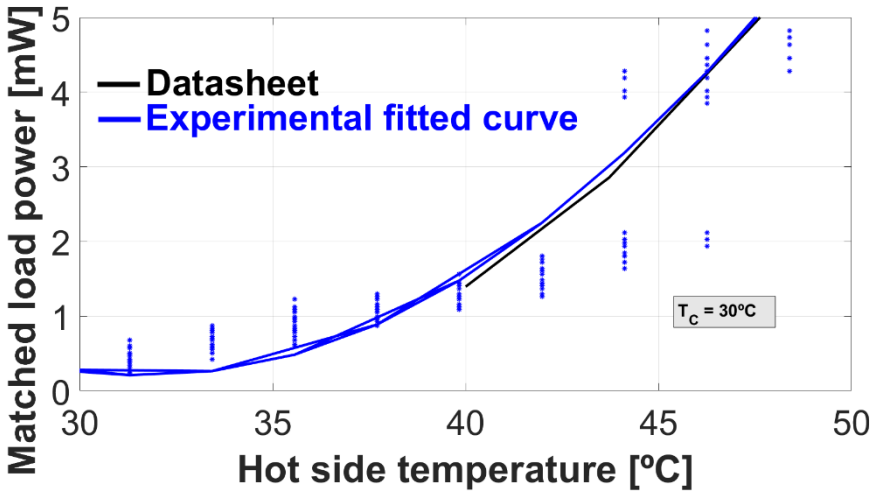

b) Detail view for the range 30ºC < Tc < 50ºC

Figure 4.11 Matched-load power graph – 11.2x11.2 TE module

Taken into account the results, the MPP curve has been modelled for a Th given in [ºC] and Tc = 30ºC. The error of the experimental fitted model is shown in Table 4.2.

$$P_{MPP}^{11.2x11.2} = -1.875 \cdot 10^{-7} \times Tc^3 + \ 3.299 \cdot 10^{-5} \times Tc^2 - 0.001299 \times Tc + 0.0146 \quad \textbf{(4.2)}$$

SSE	R-square	Adjusted R-square	RMSE
0.0021	0.9995	0.9995	0.0007952

Table 4.4 Error of the experimental fitted MPP curve of 11.2x11.2 TEG module

4.3. Outdoor test setup

Once the TE modules have been tested, and there is a power electronic circuit for harvesting the electrical energy, the whole system performance is tested at outdoor real working conditions. The tests aim to determine the actual electricity production in the month of July in the city of Alcalá de Henares (Spain).

Assembly of the outdoor setup

For the outdoor tests, the heatsinks were those used in the labs tests. For the 62x62 TE module, a PLA frame was designed in order compress the cell to the heatsink while maximising the TE surface exposed to the sunlight. The final design fits the cell and only touches its four corners. Two screws compress sufficiently the PLA frame against the heatsink so as to avoid the existence of an air gap in between.

The 11.2x11.2 TE module, on the other hand, has a PLA frame covering the heatsink for minimising its heating by heat radiation. The cell is sandwiched between the PLA and the heatsink at a certain pressure for ensuring the thermal contact. Figure 4.12 shows how the light is focused on the cell. On the top, the concentrator mechanism for heating the hot side of the TE module is set. It consists of the Fresnel lens and its holder mounted on four screws for easily adjusting its position.

The whole system is connected to a 3-degree-of-freedom positioning system (Figure 3.14). The first axis is for the coarse adjustment of the elevation of the sun, and a goniometer allows the fine adjustment of the sun position in two different axis.

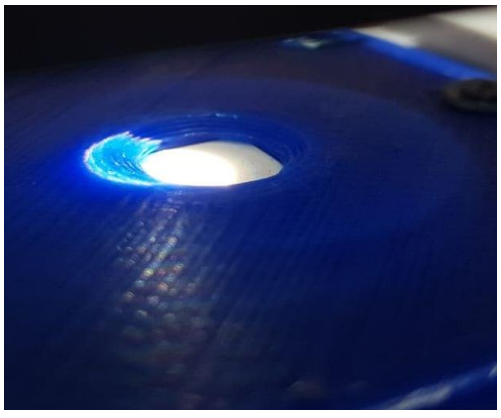

Figure 4.12 Detailed photograph of the light exposure of the TE module for a 6º deviation

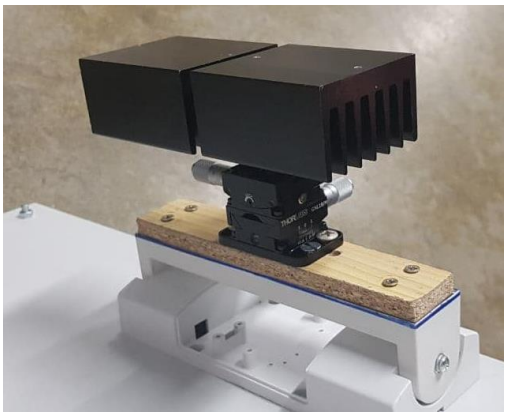

Figure 3.14 Positioning mechanism for outdoor testing

The overall circuit and the battery were placed in a protection box to reduce their exposure to the environment, and covered for preventing the sunlight to heat the electronic components (Figure 4.14).

Figure 4.13 Outdoor setup of the 11.2x11.2 and 62x62 TE modules

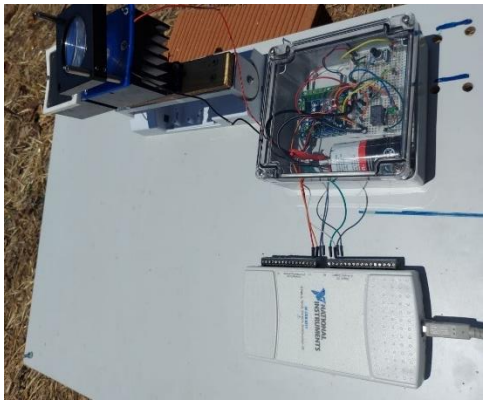

Figure 4.14 Outdoor setup of the circuit and the DAQ

The data were collected from 8AM until 3PM with clear sky during three weeks in the month of July. By doing so, a large range of irradiance was covered. Figure 4.15 depicts how the irradiance is supposed to vary throughout the day.

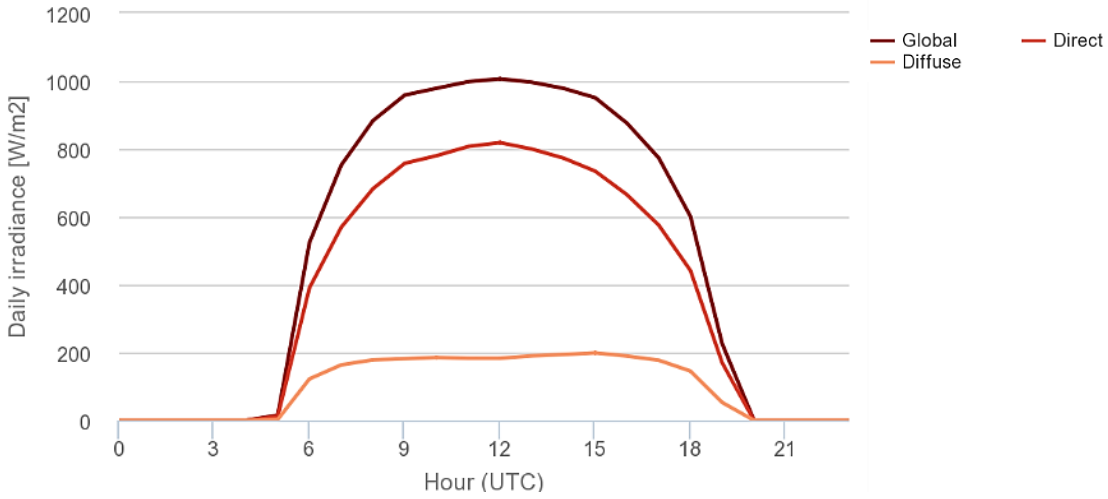

Figure 4.15 Daily irradiance profile for a 2-axis tracking in July at Alcalá de Henares (source PVGIS)

Three different kinds of tests were made: Open-circuit voltage test, power production for an optimal load and charging test. All of them under measured conditions (ambient temperature, solar irradiance, and wind speed). Both TE modules were exposed to the same conditions and their measures were taken simultaneously.

The azimuth orientation of the radiation measuring instrument was fixed to a PV module during the tests. Some solar irradiation measurements will therefore be lower than the actual values, specially from the midday onwards. This will be taken into account in the discussion of the results.

During all the tests, the goniometer was used for slightly varying the angle from -10º until +10º in the X-axis, being 0º the position perpendicular to the sun light (See Figure 3.13 and Figure 3.14). This made it possible to characterize the influence of solar positioning on the project.

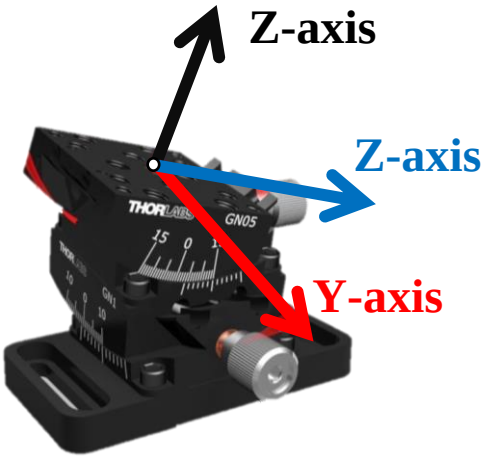

Figure 3.8 Fine 2-axis adjustment of angle - Goniometer GN Thorlabs

It will be proven in the next section that once the cell is oriented directly towards the sun, a rotation around the X-axis of the goniometer has the same impact on the results as a rotation around the Y-axis.

4.4. **Results and discussion of the outdoor tests**

This section gathers and discusses all the obtained results from the evaluation analysis performed over the three weeks of outdoor tests.

The angle variation tests take the perpendicular position to the sun as 0º reference. The comparison between the Y-axis angle misalignment and the X-axis angle misalignment is shown in Figure 4.16. It can be noticed that the axis of rotation is indifferent due to the symmetry of the TE module. The goniometer has a larger range for its Y-axis, so this will be the axis used for the position tests.

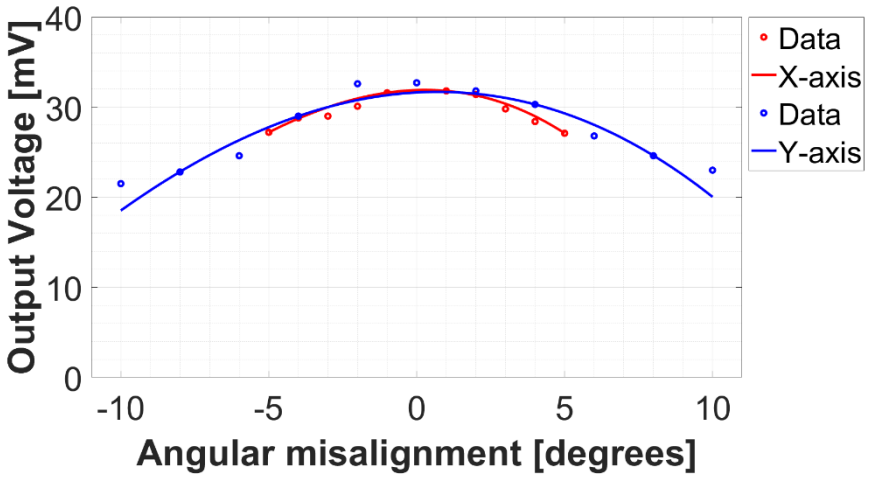

Figure 4.16 Y-axis vs X-axis rotation influence on the TE performance

Preliminary prototype results

During the outdoor tests, the 11.2x11.2TEG module had a production performance for the open-circuit test 3.7 times higher than the 62x62TE module and 11.5 times higher for the matched load power test, despite the fact that the 62x62 TE module has an effective surface exposed to the solar irradiation twice the size of the Fresnel area.

In other words, at the same working conditions, the optical concentration of solar irradiation achieves better results in energy harvesting than larger modules. This occurs for all the different solar irradiation values tested during the project (1050, 950, 850, and 750 W/m^2).

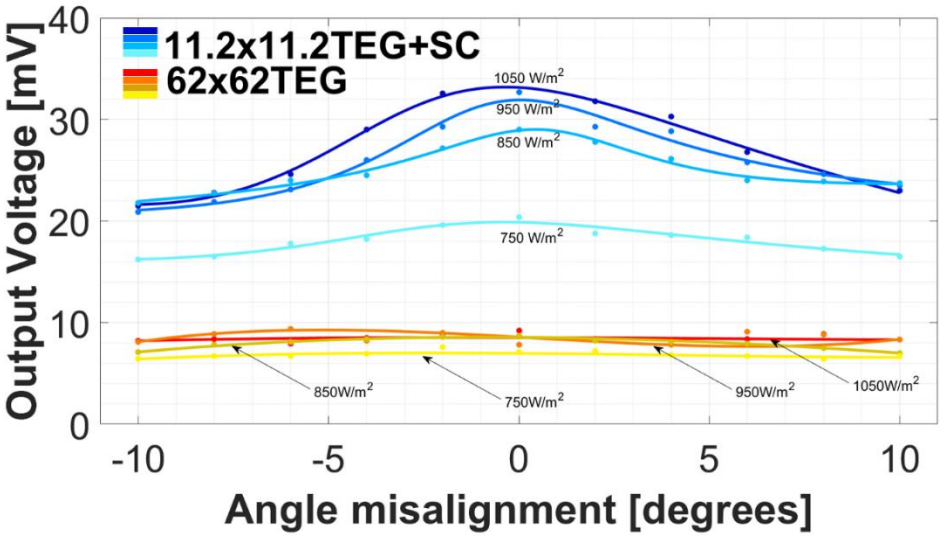

Figure 4.17 Outdoor TEG open-circuit test. Comparison between 11.2x11.2+Solar Concentrator and 62x62 TEG modules

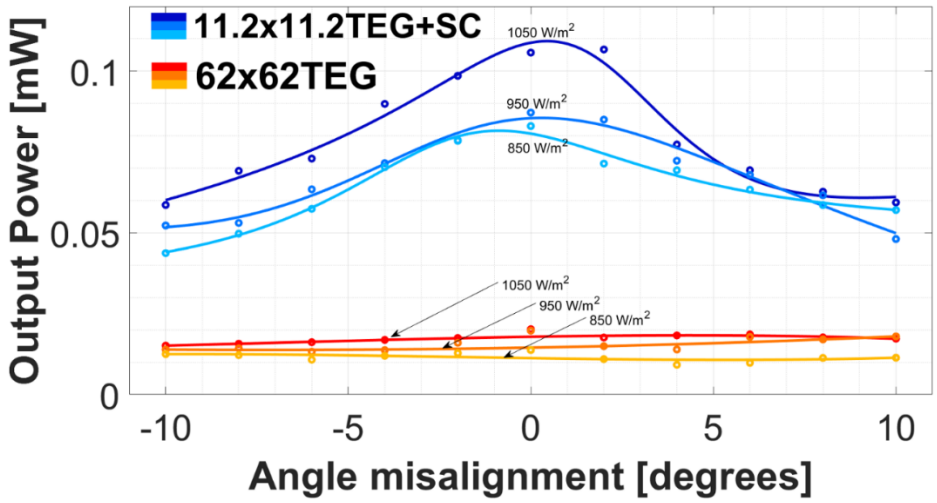

Figure 4.18 Outdoor TEG power test. Comparison between 11.2x11.2+Solar Concentrator and 62x62 TEG modules

The main reason behind this effect, in the light of the laboratory validation results, is the irradiation losses. Each cell is exposed to the environment, and so, a significant amount of the solar energy is removed as heat convection and radiation. In the case of the 62x62TEG module, this effect is even more visible. Back in Chapter 3, the utmost importance of minimising the convection and radiation was highlighted.

Future improvements on the system must overcome this issue by isolating the cell, perhaps by means of a thin-layer of non-reflective glass, or as it was finally done, by means of paint coating.

In addition, it can be noticed from Figure 4.17 and Figure 4.18 that there is a notable dependency on the angle orientation. Indeed, a variation of 10º from the incident position reduces 50% of the Voc and 45% of the output power.

The electrical performance curves depict an asymmetry with respect to the reference angle position. This displacement lies on the movement of the sun location during each period of measurement. In that period, the azimuth and the elevation angle change slightly. This effect is more evident for the lowest irradiances because they correspond to moments of the day when sun elevates faster in the sky.

Another matter of fact is the strong relationship between the solar irradiance and the electrical performance in both systems. This increase in the input heat is materialized in higher efficiency and electrical conversion. The 11.2x11.2TEG and the 62x62TEG share a similar slope owing to the fact that the incoming heat variation is identical for both systems

Altogether, it can be concluded that the first version of the system is not suitable for supplying applications (maximum values reached of 23mV and 4.7mA).

Results of the improved prototype design

The second iteration of the system brought more promising results. The layer of matt black paint boosted the spectral absorptivity of each cell as expected. The reflection of the system in both the 11.2x11.2TE+SC and the 62x62TE modules was successfully minimized and, in consequence, the power production increased.

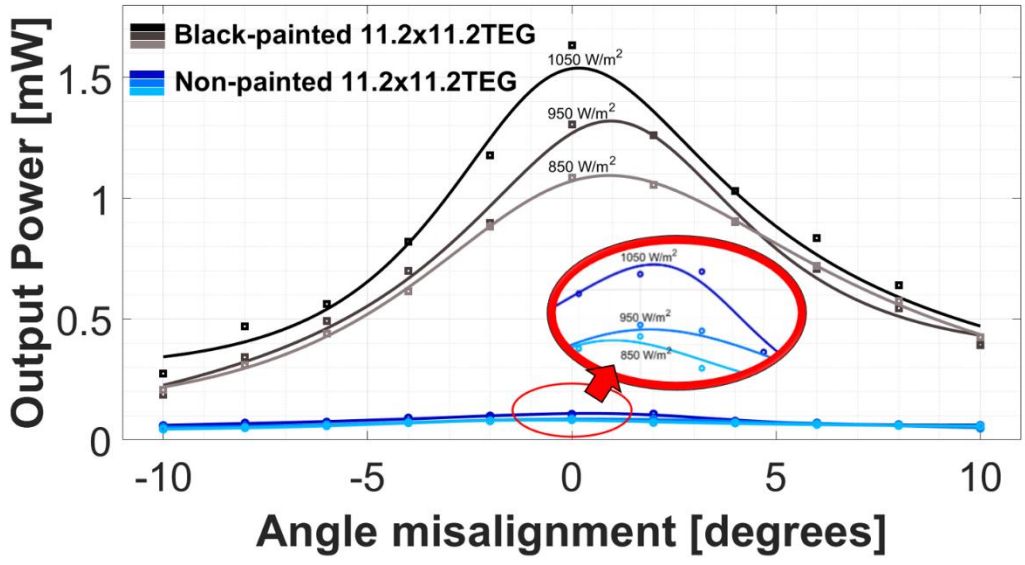

Figure 4.19 Outdoor TEG power test. Comparison between black and white 11.2x11.2 TEG module

In the improved design, the peak power is 15.31 times higher in the 11.2x11.2TEG+SC system compared to the non-painted design (Figure 4.19). Both voltage and current increased their average values.

However, the aforementioned dependency on the angle orientation is stronger in the black version. The initial system had a total power loss of -44% whereas the painted system has an drop of -78%.

The reason behind may be due to the thermal conductivity of the paint used. In fact, the obtained results are pointing out the importance of material research related to coating thermal energy systems with black layers [91], [92]. The composition of the paint and its application procedure usually lead to the formation of agglomerates on the surface that reduce the thermal conductivity.

Therefore, the morphology of the particles in the paint is crucial for improving the coating for the developed TEG system. A solution to this issue is the usage of nanomaterials such as Al_2O_3 in the paint. Morphology testing experiments have demonstrated that the powder of this metallic alternative enhances the thermal conductivity and the solar absorptivity of the coating [93].

As far as the 62x62TEG is concerned, the coating of matt-black paint has improved the power generation x18.43 compared to the non-painted version (Figure 4.20).

It can be noticed that this iteration in the design has not increased the angle dependency for the 62x62TEG system. In fact, the power production remains almost constant regardless of the angle position

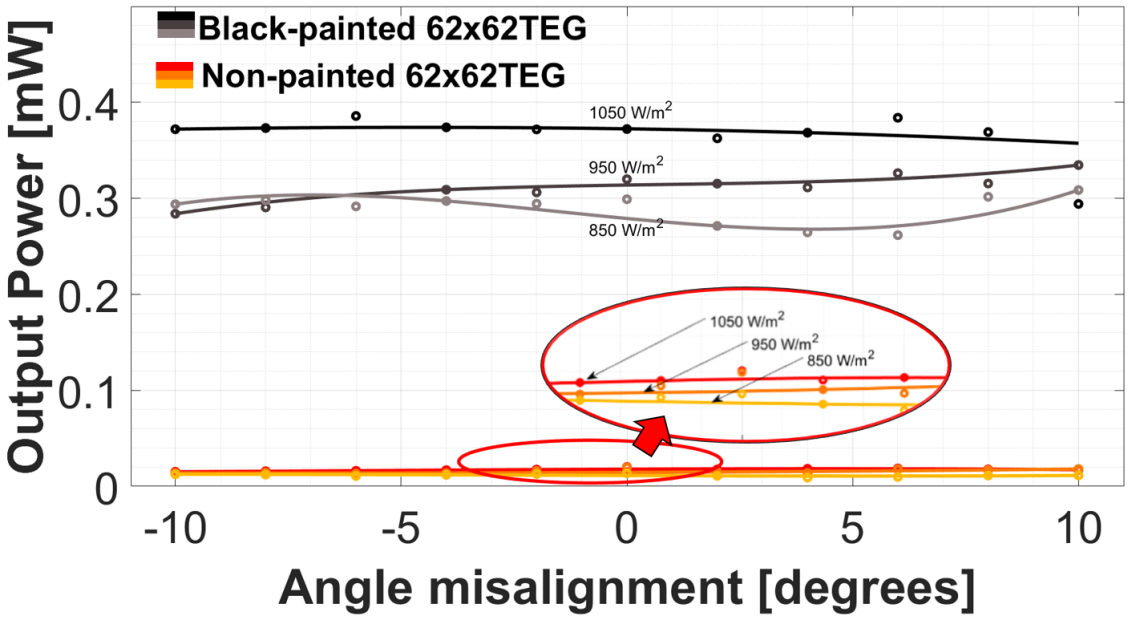

Figure 4.20 Outdoor TEG power test. Comparison between black and white 62x62 TEG module

It has to be mentioned that this system is constantly exposed to the sun, even when the direction is far from the initial position. Thus, the composition of the paint is not that relevant in this second case.

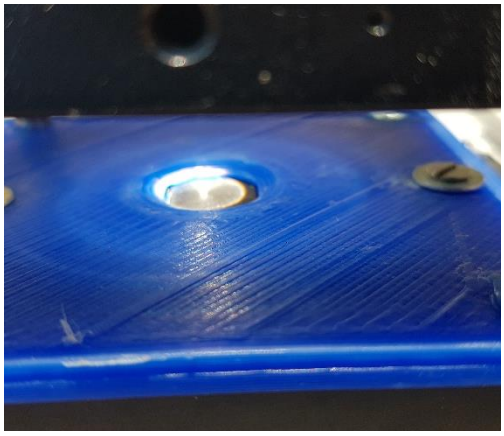

Figure 4.27 Black 11.2x11.2 TE module

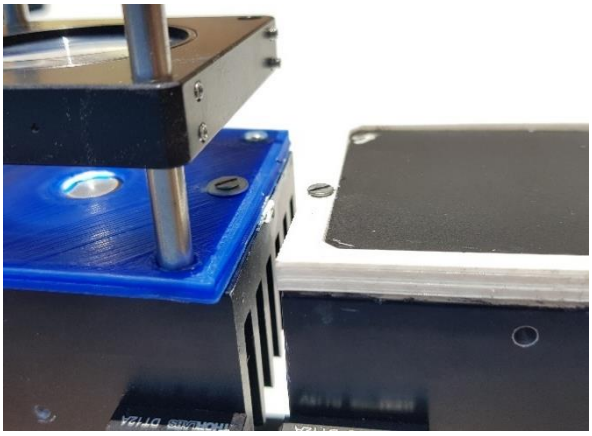

Figure 4.28 Black TE modules

Back in the state-of-the-art, it was highlighted the importance of the matched load, or optimal load resistance, for achieving the highest power production. During the outdoor tests, the matched load was tunned and registered for the whole range of solar irradiation.

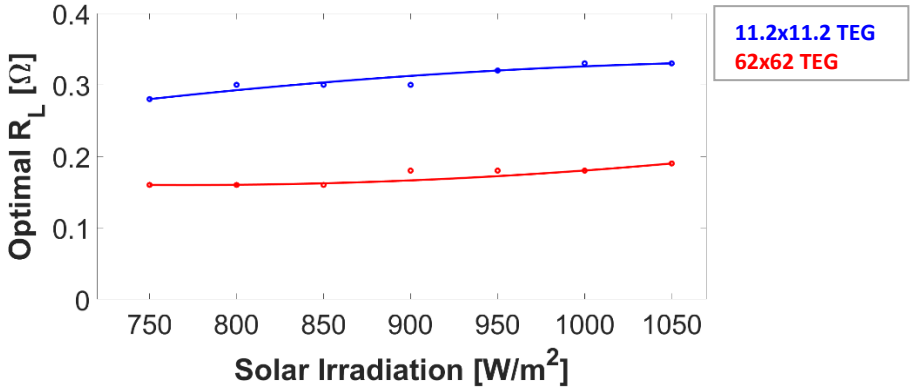

Figure 4.21 Optimal load resistance of the painted TEGs depending on the solar irradiance

The results from the outdoor conditions, shown in Figure 4.21, and the results obtained in the lab, Table 4.1 and Table 4.3, are pretty alike. In particular, the outdoor results fit the lab results for the range 30ºC-40ºC, which is precisely the registered temperature during the tests. These results have been used for the electronic design.

The third and last iteration deals with the optical characteristics of the Fresnel lens. All the outdoor tests so far this thesis were conducted with a lens whose focal length is 51mm (See section 2.1). At this point, two lenses of the same surface and different focal length were compared (Figure 4.22). This test is carried out for the dark version of the 11.2x11.2 TEG module previously discussed.

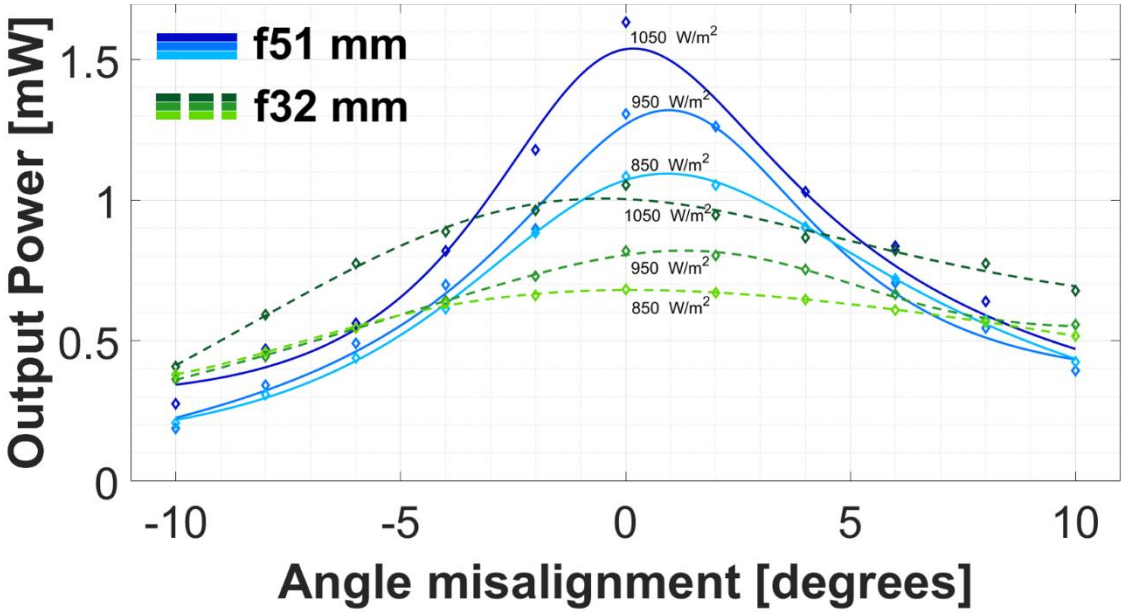

Figure 4.22 Outdoor TEG power test. Comparison between Fresnel f=51mm and f32mm

Two main observations can be remarked. Firstly, the peak power is 35.8% lower for the f32mm configuration. The power difference between both systems gets lower as the angle deviates from the reference position. Indeed, the f32mm concentration system offers a higher power production when the angular misalignment is bigger than 4.5 degrees (1050 W/m^2). Secondly, the f32mm configuration has lowered the angle dependency.

The first observation occurs due to the Refraction Law. Back in section 2.1 it was addressed how is the light transition from one medium to another.
For the f32mm lens, the incidence angle is higher due to the fact that the lens converges the same amount of light in a closer distance. Thus, the reflected light is increased. This explains why the peak power is lower.

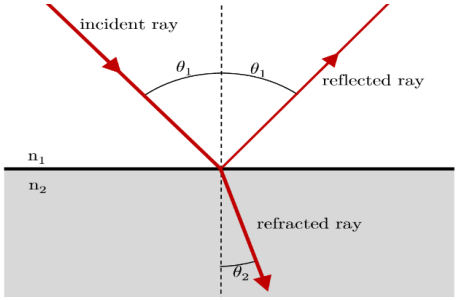

Figure 3.14 Law of refraction

Second observation concerns the design of the lens itself. The angle that defines the groove of the lens is designed to operate at a specific position. If the focal length increases, the optimal operation range is reduced [94]. Taken this into account, the f32mm system is suitable for operating in a wider range.

In terms of solar irradiance, the previous trend is present in the black-painted version. The slope between both systems is almost identical due to the fact that they share the same working conditions and experience the same temperature changes.

This thesis prioritize the energy production over the tolerance in the angle misalignment. In the light of the results, the Fresnel lens of f=51mm is more suitable for the final system. Nonetheless, an automatic solar tracker should consider the option of working with low focal length concentrators for covering a wider angle range.

Figure 4.23 shows, in logarithmic scale, the evolution in the power production from the single-TEG system to the improved concentrating TEG.

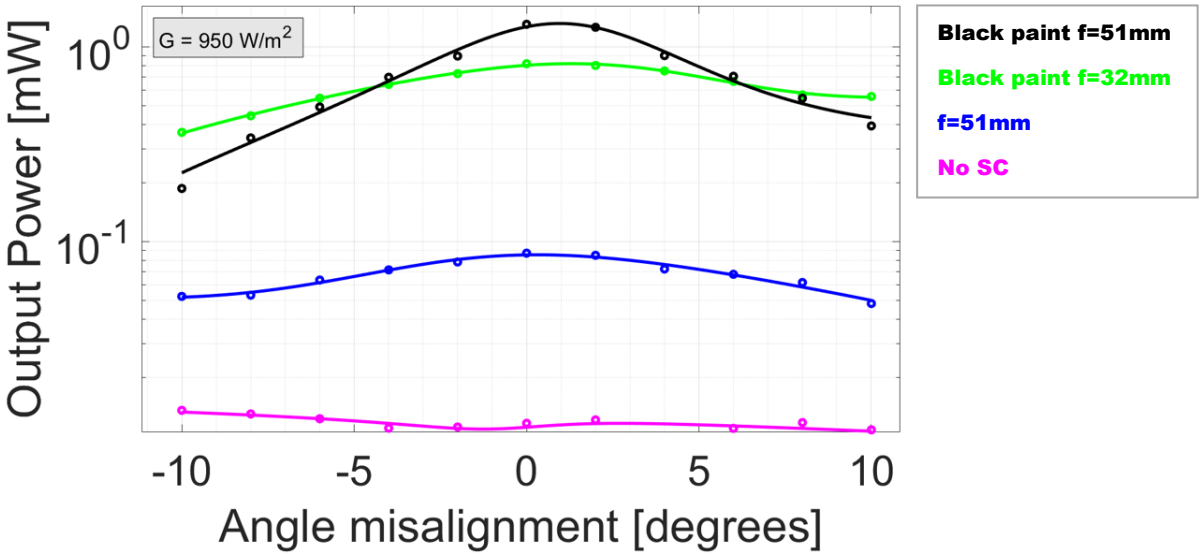

Figure 4.23 Power production comparison

The maximum power achieved was 1.634mW. According to the laboratory evaluation, this value corresponds to Th=40ºC and Tc=25ºC. However, the cold side temperature at outdoor conditions is Tc=35ºC, ten degrees higher. If the developed MPP function characterized in the laboratory is taken into account, 1.634mW is reached for Th=45ºC and Tc = 30ºC. Again, these temperatures seem to be far from the actual values.
In the thermal analysis simulation of the system for 1000W/m^2, the hot side temperature reached 55ºC and the heatsink remained at 35ºC. This is a thermal gradient of 20ºC, what would generate 5mW.

Regarding the thermal convection coefficient, its value the results obtained in the thermal analysis (Table 3.5) for the obtained output power was close to h=15 [W/m^{2}K], higher than h=8 [W/m^{2}K] corresponding to the larger module. This happens because the thermal convection coefficient is a parameter that depends on the size of the body. In addition, it has to be mentioned that a constant value of the coefficient for the whole cell was assumed, what may differ from the actual magnitude.

On the whole, there is a slight deviation of 5ºC between the MPP function and the thermal analysis simulation, especially in the low temperature gradient. This might be the cause of the different power estimations.
As previously mentioned, the objective of the power converter stage is to stabilize the TEG output voltage, which has a high sensitivity to solar radiation variations. The DC-DC power converter has been set for delivering a continuous voltage level of 1V (the voltage needed for charging the battery), and tested during a period of 200 seconds. During that time, the concentration mechanism was tracking the sun position and the TEG electrical power was at its maximum value.

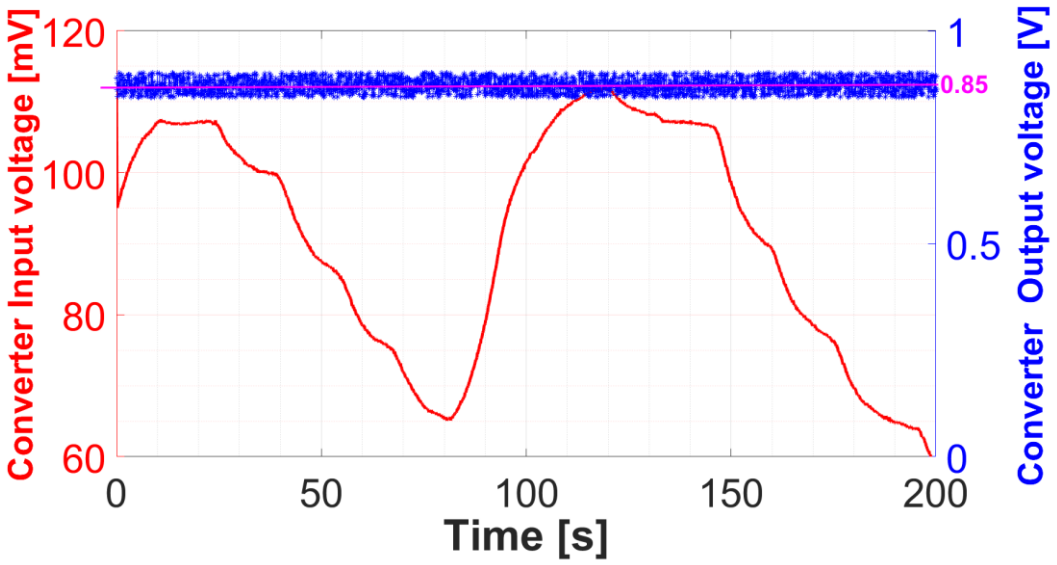

Figure 4.24 DC-DC converter - TEG voltage conditioning

In the light of the results, the converter successfully manages to maintain a voltage over a long period of time and compensates input voltage drops of up to 40% without resulting in output swings. The average output voltage is 0.851V (high enough for charging the battery), and the output peak ripple voltage was 10mV. This voltage signal can be applied to the system's battery, which was sized in section 3.4.1.

4.5. Feasibility of implementation in the SolarG project

This section discusses the feasibility of implementing the developed generator in the SolarG system as an autonomous supply for the linear actuator.

Scalability of the developed TEG system

The developed TEG-based system could be implemented in the SolarG project under specific further improvements.

The conversion efficiency can be improved by increasing the temperature gradient from 10-15ºC($\eta = 3\%$) to 30ºC($\eta = 4\%$). This is achievable for a larger Fresnel lens (diameter of 100mm) and coating of metallic powder over the TE module. According to the MPP characterization curve, this increase in efficiency accompanied by a higher hot-source temperature can boost the power production at least three times compared to the developed system. This accounts to a daily power production of 50mWh per TE.
Considering a conversion efficiency of 80%, 7 units of the system would be needed for generating the enough electrical power required by the linear actuator (estimation of 0.26Wh per day).

The proposed system of 7 units has a total price of 210€[10], including commercially available Fresnel lenses of 100mm, the used TEG cells, and a larger heatsink.
According to PVGIS [84], an one-axis PV panel of 1kW located at Alcalá de Henares in July produces 49.27% more electrical energy than a stand-alone system, more precisely 84.67kWh more. The linear actuator displaces two PV panels, what accounts for an additional power production of 169.34kWh.
In the 2019 report of the Renewable Energy Agency (IRENA) [95], the price of PV energy is 0.07 €/kWh. Thus, the benefits of generating 169.34kWh more per month would amortized the proposed system in 18 months.

[10]Calculations based on the prices registered in the Budget of the project. See Chapter 5

Hybrid thermoelectric and PV system

The expensive manufacturing process of the PV panel and the fact that high working temperatures affect the production efficiency pose a challenge for PV systems. The possibility of alternating a PV solar system with TEG technologies can bring a more efficiently use of the solar energy without causing any harm to the environmental.
It has been demonstrated that CPV+TEG systems enhance power production at high solar concentrations. This improvement depends on design parameters of the CPV and the TEG, such as the ZT of the TEG cell or the temperature coefficient of the PV panel [96].

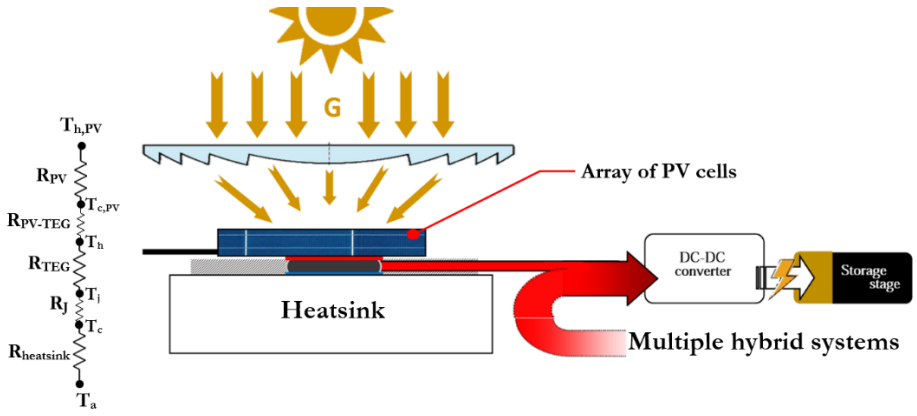

Figure 4.25 Hybrid solar system CPV+TEG

However, this approach has some downsides. Firstly, the adding of TEG cells to a PV panel increases the overall thermal resistance of the structure, thereby increasing the operating temperature at the PV cells with respect to a PV-only system. As previously introduced in section 2.4.1, the higher the operating temperature of a PV, the lower its conversion efficiency. Moreover, a higher operating temperature accelerates material degradation and the reduces the MPP of the PV cell [97]–[99].

On the whole, ultra-high concentration PV (UHCPV) systems are more suitable for this hybridisation, though there is a lack of investigations on this topic. The PV panels of SolarG project do not have solar concentration and thermal hybridisation with TEG systems is therefore disregarded.

Chapter 5

Budget of the project

This section describes the budget for the whole project. This budget compounds the manpower, goods, and software costs.

Manpower

Item	Ref.	Description	Unit cost [€/h]	Time [h]	Total Cost [€]
Research Staff (Student)	P01	Time dedicated to the project by the student (estimation)	20.00	500	10,000.00
Total					€ 10,000.00

Table 5.1 Manpower cost

Goods

Item	Ref.	Description	Unit cost [€/unit]	Units	Total Cost [€]
HP Pavilion 15DK0020NS	M01	Laptop	363.64*1	1	363.64
NI USB6211	M02	Multichannel data acquisition module	391.35*2	1	391.35
Electronic components	M03	Power electronic system and storage stage	46.95	1	46.95
STMicroelectronics Evaluation Board	M04	Energy Harvester and Battery Charger	43.44	1	43.44
Heatsink	M05	Heat evacuation of the TEG cells	12.21	2	24.42
PLA [m]	M06	Material for 3D prototyping	0.059	70	4.13
Solid Optical Breadboards	M07	Laboratory test rig	48.20	1	48.20
Large Dual-Axis Goniometer	M08	2DOF mechanism for accurate orientation	516.42	1	516.42
Mica heating pad	M09	Heat source at lab tests	45.01	1	45.01
Thermal resistor 1W	M10	Heat source at lab tests	0.05	10	0.50
Fresnel lens f51mm	M11	Optical concentration	22.13	1	22.13
Fresnel lens f32mm	M12	Optical concentration	30.25	1	30.25
TE module 11.2x11.2	M13	TEG power production	23.47	2	46.94
TE module 62x62	M14	TEG power production	51.16	1	51.16

Fresnel cage plate	M15	Lens holder	37.38	1	37.38
Thermal Grease	M16	High conductivity paste	7.70	1	7.70
Mineral wool	M17	Insulating material	3.00	1	3.00
Pt1000	M18	Temperature meter	0.67	4	2.68
Solar calibrated sensor	M19	Solar irradiation meter	29.62*3	1	29.62
Total					€ 1,714.92

Table 5.2 Goods cost

Unit cost amortized for 231 working days.

*1 Purchase cost € 700.00. Time used: 120 days.
*2 Purchase cost € 1,130.00. Time used: 80 days.
*3 Purchase cost € 310.97. Time used: 20 days.

Software licenses

Item	Ref.	Category	Unit cost [€/day]	Time [days]	Total Cost [€]
NI LabVIEW 2020	S01	Data acquisition	25.38*4	80	2,030.40
MATLAB R2021a	S02	TEG Calculator, data acquisition, and curve fitting	3.47*5	120	416.40
Autodesk Inventor Professional 2021	S03	Design of the concentrator mechanism	12.50*6	100	1,250.00
Autodesk Fusion 360	S04	Thermal simulation	2.18*7	20	43.60
CADENCE OrCAD 17.4	S05	Design of the circuit electronics	2.91*8	20	58.20
Microsoft Office 365	S06	Report of the project	0.31*9	120	37.20
Total					€ 3,835.80

Table 5.3 Software cost

Unit cost calculated for 231 working days. Installation and maintenance costs prorated.

*1 Licence cost € 5,861.00.
*2 Licence cost € 800.00.
*3 Licence cost € 2,886.00.
*4 Licence cost € 503.00.
*5 Licence cost € 670.00.
*6 Licence cost € 70.00.

Miscellaneous

Item	Ref.	Description	Unit cost [€/month]	Time [months]	Total Cost [€]
Internet subscription	MS01	-	30.00	6	180.00
Total					180.00

Table 5.4 Miscellaneous cost

The total amount is:

Total [€]	15,730.72

Taxes not incl.

" The total budget for the execution of this project amounts to fifteen thousand seven hundred and thirty thousand euros and seventy-two cents (15,730.72 euros). Taxes not included"

Chapter 6

Conclusions

I saw the angel enclosed in the marble,
and carved until I set him free.

Michelangelo

This project presents the design, manufacturing, and testing of a solar concentration thermoelectric generator that harvests energy directly from solar radiation.

The prototype of the concentrating TEG system is mainly composed by a 50.8 mm Fresnel lens that concentrates sun radiation (about 16 times) on top of a TEG module of 11.2x11.2 mm^2. This module is fixed to an aluminium heatsink in order to improve the flow of the heat from the hot upper surface of the TEG and the environment (cold sink). The output of the TEG module is electrically connected to a power electronics circuit and an energy storage system that maximizes, stabilizes and stores the electric energy produced.

After various prototype improvements and tests in laboratory conditions, a final improved prototype was tested in outdoor conditions in Alcalá de Henares (Spain) in July 2021. The performance of the concentrating TEG was characterized for various irradiance levels and environmental conditions, and compared to the performance of a non-concentrating TEG system. A peak power generation of 1.6mW for a solar irradiance of 1050 W/m^2 was observed.

Thanks to the improved performance of the concentrating TEG, it produces up to 4 times the output power of that of the non-concentrating TEG. This is mainly due to the fact that temperature gradient is improved in the concentrating prototype and also heat losses are minimized.

The potential of the TEG system to power an orientation mechanism of a solar photovoltaic facility is also investigated. In ten hours, a generator based on 7 concentrating TEG systems can charge a battery with sufficient capacity to supply the solar tracker actuator for an entire day.

The implementation of the system in PV installations is feasible, although the low efficiency of the TE technology makes solar TEG systems a less attractive alternative to power PV auxiliary system than traditional PV panels.

Future work

The presented project analyzed the power generation of a single TE+SC system. A series connection of more systems will better the conversion rate of the electronic circuit. Thus, the advantages of a larger TE+SC system able to power the battery faster can be amortized by the consequent increase in photovoltaic energy production. Applying certain modifications to the design, a seven-unit system such as the one developed in this project could fully charge the battery stage in one single day.

The extrapolation of the obtained results to a system operating 24 hours a day is out of scope. Hence a further improvement in the system involves studying the thermal inertia of the surrounding air and obtaining the output power performance throughout the day.
Owing to the fact that TEG modules can change its electrical polarity depending on the sense of the temperature gradient, future course of action can analyse the feasibility of harnessing the temperature of the ground during the night, when the hot side of the mechanism is at its lowest temperature. If a high enough temperature gradient is achieved, the system will be able to operate high-enough per day and the time estimated for charging the battery will decrease.

Bibliography

[1] Intergovernmental panel on climate change (IPCC), "Summary for Policymakers. In: Climate Change 2021: The Physical Science Basis. Contribution of Working Group I to the Sixth Assessment Report of the Intergovernmental Panel on Climate Change," *Cambridge Univ. Press*, pp. 1–42, Aug. 2021.

[2] International Energy Agency, *World Energy Statistics 2019*. OECD, 2019.

[3] O. B. Adekoya, J. K. Olabode, and S. K. Rafi, "Renewable energy consumption, carbon emissions and human development: Empirical comparison of the trajectories of world regions," *Renew. Energy*, vol. 179, pp. 1836–1848, Dec. 2021

[4] IRENA, "World Energy Transitions Outlook: 1.5° C Pathway," Abu Dhabi, 2021.

[5] D. P. Kothari and P. M. V. Subba Rao, *Handbook of Mechanical Engineering - Power Generation*, 1st ed. New York: Springer, 2009.

[6] D. Sakthivadivel, K. Balaji, D. Dsilva Winfred Rufuss, S. Iniyan, and L. Suganthi, *Solar energy technologies: principles and applications*. Academic Press, 2021.

[7] K. Shanks, S. Senthilarasu, and T. K. Mallick, *High-Concentration Optics for Photovoltaic Applications*, vol. 190. Springer, Cham, 2015.

[8] M. H. Freeman, C. C. Hull, and W. N. Charman, *Reflection and refraction at plane surfaces*. Butterworth-Heinemann, 2003.

[9] G. Wang, F. Wang, Z. Chen, P. Hu, and R. Cao, "Experimental study and optical analyses of a multi-segment plate (MSP) concentrator for solar concentration photovoltaic (CPV) system," *Renew. Energy*, vol. 134, pp. 284–291, Apr. 2019,

[10] S. C. Bhatia, "Solar thermal energy," in *Advanced Renewable Energy Systems*, Elsevier, 2014, pp. 94–143.

[11] W. Weiss and M. Rommel, "Solar heat for industrial processes. Temperature collectors," *Int. Energy Agency*, vol. 33, no. II, pp. 23–48, Sep. 2006, Accessed: Aug. 28, 2021. [Online]. Available: www.iea-ship.orgwww.iea-shc.orgwww.solarpaces.org.

[12] V. Kumar and A. Yadav, "Experimental investigation of parabolic dish concentrator with various sizes of receiver," *Mater. Today Proc.*, vol. 44, pp.

4966–4971, Jan. 2021

[13] K. S. Reddy, T. S. Vikram, and T. K. Mallick, "Experimental performance investigations of an elliptical hyperbolic non-imaging solar concentrator with trapezoidal surface receiver for process heat applications," *J. Clean. Prod.*, vol. 192, pp. 735–750, Aug. 2018

[14] S. Sripadmanabhan Indira, C. A. Vaithilingam, R. Sivasubramanian, K.-K. Chong, R. Saidur, and K. Narasingamurthi, "Optical performance of a hybrid compound parabolic concentrator and parabolic trough concentrator system for dual concentration," *Sustain. Energy Technol. Assessments*, vol. 47, p. 101538, Oct. 2021

[15] M. Khamooshi, H. Salati, F. Egelioglu, A. Hooshyar Faghiri, J. Tarabishi, and S. Babadi, "A Review of Solar Photovoltaic Concentrators," *Int. J. Photoenergy*, vol. 2014, pp. 1–17, 2014

[16] H. Zheng, "Solar Energy Utilization and Its Collection Devices," *Sol. Energy Desalin. Technol.*, pp. 47–171, 2017

[17] P. A. Tipler and G. P. Mosca, *Physics for scientists and engineers*, 6th ed. New York: W.H. Freeman, 2003.

[18] J. Page, "The Role of Solar-Radiation Climatology in the Design of Photovoltaic Systems," in *Practical Handbook of Photovoltaics*, Elsevier, 2012, pp. 573–643.

[19] G. Casano and S. Piva, "Experimental investigation of the performance of a thermoelectric generator based on Peltier cells," *Exp. Therm. Fluid Sci.*, vol. 35, no. 4, pp. 660–669, May 2011

[20] J. C. Peltier, "Nouvelles expériences sur la caloricité des courants électrique (New experiments on the heat effects of electric currents)," *Ann. Chim. Phys.*, vol. 56, pp. 371–386, 1834.

[21] W. Thomson, "On a Mechanical Theory of Thermo-Electric Currents.," *Proc. R. Soc. Edinburgh*, vol. 3, pp. 91–98, Mar. 1857

[22] T. J. Seebeck, "Magnetic polarization of metals and minerals," *Abhandlungen der Dtsch. Akad. der Wissenschaften zu Berlin*, vol. 265, 1822.

[23] W. Thomson, "IX.— On the Dynamical Theory of Heat . Part V. Thermo-electric Currents," *Trans. R. Soc. Edinburgh*, vol. 21, no. 1, pp. 123–171, Jan. 1857

[24] H. Jouhara, N. Khordehgah, S. Almahmoud, B. Delpech, A. Chauhan, and S. A. Tassou, "Waste heat recovery technologies and applications," *Therm. Sci. Eng. Prog.*, vol. 6, pp. 268–289, Jun. 2018

[25] B. Singh, T. Lippong, A. Date, and A. Akbarzadeh, "The Effects of Temperature Difference and Compressive Force to the Electrical Characterization of Peltier Cell for Artificial Concentrated Solar Power Thermoelectric Application," pp. 15–30, 2014.

[26] M. J. Moran and H. N. Shapiro, *Fundamentals of engineering thermodynamics*, 6th ed. Chichester: John Wiley, 1998.

[27] Y. Apertet, H. Ouerdane, O. Glavatskaya, C. Goupil, and P. Lecoeur, "Optimal working conditions for thermoelectric generators with realistic thermal coupling," *EPL (Europhysics Lett.*, vol. 97, no. 2, p. 28001, Jan. 2012

[28] H. Alam and S. Ramakrishna, "A review on the enhancement of figure of merit from bulk to nano-thermoelectric materials," *Nano Energy*, vol. 2, no. 2, pp. 190–212, 2013

[29] E. Kanimba and Z. Tian, "Modeling of a Thermoelectric Generator Device," *Thermoelectr. Power Gener. - A Look Trends Technol.*, Dec. 2016

[30] R. Venkatasubramanian, E. Siivola, T. Colpitts, and B. O'Quinn, "Thin-film thermoelectric devices with high room-temperature figures of merit," *Nature*, vol. 413, no. 6856, pp. 597–602, Oct. 2001

[31] T.-S. Kim, I.-S. Kim, T.-K. Kim, S.-J. Hong, and B.-S. Chun, "Thermoelectric properties of p-type 25%Bi2Te3+75%Sb2Te3 alloys manufactured by rapid solidification and hot pressing," *Mater. Sci. Eng. B*, vol. 90, no. 1–2, pp. 42–46, Mar. 2002

[32] Z.-G. Chen, G. Han, L. Yang, L. Cheng, and J. Zou, "Nanostructured thermoelectric materials: Current research and future challenge," *Prog. Nat. Sci. Mater. Int.*, vol. 22, no. 6, pp. 535–549, Dec. 2012

[33] "nanoHUB.org - Resources: Introduction to Thermoelectricity Lecture 1.6: Theory - Figure of Merit." https://nanohub.org/resources/31462/watch?resid=31516&time=00:01:04 (accessed Aug. 08, 2021).

[34] G. J. Snyder and E. S. Toberer, "Complex thermoelectric materials," *Nat. Mater.*, vol. 7, no. 2, pp. 105–114, Feb. 2008

[35] M. Aminzare, Y.-C. Tseng, and Y. Mozharivskyj, "Effect of spark plasma sintering and Sb doping on the thermoelectric properties of Co4Ge6Te6 skutterudite," *J. Solid State Chem.*, vol. 269, pp. 434–441, Jan. 2019

[36] S. Deng, Y. Saiga, K. Suekuni, and T. Takabatake, "Enhancement of thermoelectric efficiency in type-VIII clathrate Ba8Ga16Sn30 by Al substitution

for Ga," *J. Appl. Phys.*, vol. 108, no. 7, p. 073705, Oct. 2010

[37] Y. Zhang, X. Wang, M. Cleary, L. Schoensee, N. Kempf, and J. Richardson, "High-performance nanostructured thermoelectric generators for micro combined heat and power systems," *Appl. Therm. Eng.*, vol. 96, pp. 83–87, Mar. 2016

[38] Y. Zhang *et al.*, "High-temperature and high-power-density nanostructured thermoelectric generator for automotive waste heat recovery," *Energy Convers. Manag.*, vol. 105, pp. 946–950, Nov. 2015

[39] R. Rabari, S. Mahmud, and A. Dutta, "Numerical simulation of nanostructured thermoelectric generator considering surface to surrounding convection," *Int. Commun. Heat Mass Transf.*, vol. 56, pp. 146–151, Aug. 2014

[40] T.-C. Tsai, H.-C. Chang, C.-H. Chen, and W.-T. Whang, "Widely variable Seebeck coefficient and enhanced thermoelectric power of PEDOT:PSS films by blending thermal decomposable ammonium formate," *Org. Electron.*, vol. 12, no. 12, pp. 2159–2164, Dec. 2011

[41] C. Wang, S. Tang, X. Liu, G. H. Su, W. Tian, and S. Qiu, "Experimental study on heat pipe thermoelectric generator for industrial high temperature waste heat recovery," *Appl. Therm. Eng.*, vol. 175, p. 115299, Jul. 2020

[42] B. Singh, W. A. N. W. Mohamed, M. N. F. Hamani, and K. Z. N. A. Sofiya, "Enhancement of low grade waste heat recovery from a fuel cell using a thermoelectric generator module with swirl flows," *Energy*, vol. 236, p. 121521, Dec. 2021

[43] B. Kılkış, "Development of a composite PVT panel with PCM embodiment, TEG modules, flat-plate solar collector, and thermally pulsing heat pipes," *Sol. Energy*, vol. 200, pp. 89–107, Apr. 2020

[44] E. S. Mohamed, "Development and performance analysis of a TEG system using exhaust recovery for a light diesel vehicle with assessment of fuel economy and emissions," *Appl. Therm. Eng.*, vol. 147, pp. 661–674, Jan. 2019

[45] A. Heghmanns, M. Beitelschmidt, S. Wilbrecht, K. Geradts, and G. Span, "Development and Optimization of a TEG-system for the Waste Heat Usage in Railway Vehicles," *Mater. Today Proc.*, vol. 2, no. 2, pp. 780–789, 2015

[46] E. Kordetoodeshki and A. Hassanzadeh, "An ultra-low power, low voltage DC-DC converter circuit for energy harvesting applications," *AEU - Int. J. Electron. Commun.*, vol. 98, pp. 8–18, Jan. 2019

[47] TEGWAY, "Flexible Thermo-electric Device," 2021. http://tegway.co/tegway/ (accessed Sep. 01, 2021).

[48] D. Kraemer *et al.*, "High-performance flat-panel solar thermoelectric generators with high thermal concentration," *Nat. Mater.*, vol. 10, no. 7, pp. 532–538, Jul. 2011

[49] M. Telkes, "Solar Thermoelectric Generators," *J. Appl. Phys.*, vol. 25, no. 6, pp. 765–777, Jun. 2004

[50] N. Mohan, T. M. Undeland, and W. P. Robbins, *Power electronics : converters, applications and design*, 3rd ed. John Wiley & Sons, 2003.

[51] J. UREÑA *et al.*, *ELECTRONICA DE POTENCIA*, 1st ed. Alcalá de Henares: UNIVERSIDAD ALCALA, 1999.

[52] V. Kamala Devi, K. Premkumar, A. Bisharathu Beevi, and S. Ramaiyer, "A modified Perturb & Observe MPPT technique to tackle steady state and rapidly varying atmospheric conditions," *Sol. Energy*, vol. 157, pp. 419–426, Nov. 2017

[53] S. Necaibia, M. S. Kelaiaia, H. Labar, A. Necaibia, and E. D. Castronuovo, "Enhanced auto-scaling incremental conductance MPPT method, implemented on low-cost microcontroller and SEPIC converter," *Sol. Energy*, vol. 180, pp. 152–168, Mar. 2019

[54] T. Esram and P. L. Chapman, "Comparison of Photovoltaic Array Maximum Power Point Tracking Techniques," *IEEE Trans. Energy Convers.*, vol. 22, no. 2, pp. 439–449, Jun. 2007

[55] M. Fathi and J. A. Parian, "Intelligent MPPT for photovoltaic panels using a novel fuzzy logic and artificial neural networks based on evolutionary algorithms," *Energy Reports*, vol. 7, pp. 1338–1348, Nov. 2021

[56] F. Li *et al.*, "Adaptive rapid neural optimization: A data-driven approach to MPPT for centralized TEG systems," *Electr. Power Syst. Res.*, vol. 199, p. 107426, Oct. 2021

[57] J. Kim, P. K. T. Mok, and C. Kim, "A 0.15 V Input Energy Harvesting Charge Pump With Dynamic Body Biasing and Adaptive Dead-Time for Efficiency Improvement," *IEEE J. Solid-State Circuits*, vol. 50, no. 2, pp. 414–425, Feb. 2015

[58] G. Singh and S. Kundu, "An efficient DC-DC boost converter for thermoelectric energy harvesting," *AEU - Int. J. Electron. Commun.*, vol. 118, p. 153132, May

2020

[59] A. F. Mirza, M. Mansoor, K. Zerbakht, M. Y. Javed, M. H. Zafar, and N. M. Khan, "High-efficiency hybrid PV-TEG system with intelligent control to harvest maximum energy under various non-static operating conditions," *J. Clean. Prod.*, p. 128643, Aug. 2021

[60] B. Yang *et al.*, "MPPT design of centralized thermoelectric generation system using adaptive compass search under non-uniform temperature distribution condition," *Energy Convers. Manag.*, vol. 199, p. 111991, Nov. 2019

[61] B. Yang *et al.*, "Fast atom search optimization based MPPT design of centralized thermoelectric generation system under heterogeneous temperature difference," *J. Clean. Prod.*, vol. 248, p. 119301, Mar. 2020

[62] I. Valiente Blanco, "SolarG Mejora sostenible de la eficiencia energética de paneles solares mediante sistema modular de refrigeración geotérmico," 2019.

[63] R. Satpathy and V. Pamuru, "Solar photovoltaic systems," *Sol. PV Power*, pp. 267–315, Jan. 2021

[64] D. Zhang and A. Allagui, "Fundamentals of solar photovoltaic systems," *Des. Perform. Optim. Renew. Energy Syst.*, pp. 117–129, Jan. 2021

[65] A. Jäger-Waldau, "PV Status Report 2019," EUR 29938 EN, 2019.

[66] M. A. Green, E. D. Dunlop, D. H. Levi, J. Hohl‐Ebinger, M. Yoshita, and A. W. Y. Ho‐Baillie, "Solar cell efficiency tables (version 54)," *Prog. Photovoltaics Res. Appl.*, vol. 27, no. 7, pp. 565–575, Jul. 2019

[67] H. Muellejans *et al.*, "State-of-the-art for assessment of solar energy technologies," 2020.

[68] REN21, "RENEWABLES 2020 GLOBAL STATUS REPORT," 2020. [Online]. Available: https://abdn.pure.elsevier.com/en/en/researchoutput/ren21(5d1212f6-d863-45f7-8979-5f68a61e380e).html.

[69] S. Razza, S. Castro-Hermosa, A. Di Carlo, and T. M. Brown, "Large-area deposition, coating, printing, and processing techniques for the upscaling of perovskite solar cell technology," *APL Mater.*, vol. 4, no. 9, p. 091508, Sep. 2016,

[70] J. Ramanujam and U. P. Singh, "Copper indium gallium selenide based solar cells – a review," *Energy Environ. Sci.*, vol. 10, no. 6, pp. 1306–1319, 2017

[71] A. K. S. David Tan, *Handbook for Solar Photovoltaic Systems*, 1st ed. California: American Energy Market Authority (AEMA), 2011.

[72] S. Chander, A. Purohit, A. Sharma, S. P. Nehra, and M. S. Dhaka, "Impact of

temperature on performance of series and parallel connected mono-crystalline silicon solar cells," *Energy Reports*, vol. 1, pp. 175–180, Nov. 2015

[73] K. W. Böer, *Survey of Semiconductor Physics Volume II Barriers, Junctions, Surfaces, and Devices*. 1992.

[74] A. Ouédraogo, B. Zouma, E. Ouédraogo, L. Guissou, and D. J. Bathiébo, "Individual efficiencies of a polycrystalline silicon PV cell versus temperature," *Results Opt.*, vol. 4, p. 100101, Aug. 2021

[75] S. Dubey, J. N. Sarvaiya, and B. Seshadri, "Temperature dependent photovoltaic (PV) efficiency and its effect on PV production in the world," in *Energy Procedia*, Jan. 2013, vol. 33, pp. 311–321

[76] A. K. Behura, B. N. Prasad, and L. Prasad, "Heat transfer, friction factor and thermal performance of three sides artificially roughened solar air heaters," *Sol. Energy*, vol. 130, pp. 46–59, Jun. 2016

[77] A. M. A. Soliman, H. Hassan, and S. Ookawara, "An experimental study of the performance of the solar cell with heat sink cooling system," *Energy Procedia*, vol. 162, pp. 127–135, Apr. 2019

[78] D. López Pascual, "Diseño de un sistema de mejora de la eficiencia de paneles solares fotovoltaicos," 2020.

[79] A. Machniewicz, D. Knera, and D. Heim, "Effect of Transition Temperature on Efficiency of PV/PCM Panels," *Energy Procedia*, vol. 78, pp. 1684–1689, Nov. 2015

[80] R. Wang, J. Wang, and W. Yuan, "Analysis and Optimization of a Microchannel Heat Sink with V-Ribs Using Nanofluids for Micro Solar Cells," *Micromachines*, vol. 10, no. 9, p. 620, Sep. 2019

[81] M. Benghanem, A. A. Al-Mashraqi, and K. O. Daffallah, "Performance of solar cells using thermoelectric module in hot sites," *Renew. Energy*, vol. 89, pp. 51–59, Apr. 2016

[82] M. D. S. Borkar, D. S. V. Prayagi, and M. J. Gotmare, "Performance Evaluation of Photovoltaic Solar Panel Using Thermoelectric Cooling," *Int. J. Eng. Res.*, vol. 3, no. 9, pp. 536–539, Sep. 2014

[83] T. O. Ale and K. J. Rotipin, "Cooling effects on photovoltaic module performance in the tropical region," *Niger. J. Technol.*, vol. 38, no. 3, p. 702, Dec. 2019

[84] Joint Research Centre (JRC), "Photovoltaic Geographical Information System

(PVGIS) - European Commission." https://re.jrc.ec.europa.eu/pvg_tools/en/#MR (accessed Aug. 11, 2021).

[85] P. Kosky, R. Balmer, W. Keat, and G. Wise, *Mechanical Engineering*. Academic Press, 2013.

[86] STMicroelectronics, "STEVAL-ISV020V1 ¦ Evaluation Board for SPV1050 ULP Energy Harvester and Battery Charger," *RS Components*. https://es.rs-online.com/web/p/kits-de-desarrollo-de-alimentacion-motores-y-robots/1962570 (accessed Aug. 30, 2021).

[87] K. Anderson and M. Mikofski, "Slope-Aware Backtracking for Single-Axis Trackers," 2020, Accessed: Sep. 04, 2021. [Online]. Available: https://www.nrel.gov/docs/fy20osti/76626.pdf.

[88] T. Hoffmann, "SunCalc." https://www.suncalc.org/#/40.5134,-3.3454,15/2021.07.15/10:19/1/0 (accessed Aug. 11, 2021).

[89] S. Ahmad, S. Shafie, and M. Z. A. Ab Kadir, "Power Feasibility of a Low Power Consumption Solar Tracker," *Procedia Environ. Sci.*, vol. 17, pp. 494–502, 2013,

[90] P. Drexhage and P. Beckedahl, "Thermal Paste application process," 2018.

[91] H. H. Al-Kayiem, A. A. Ismaeel, A. T. Baheta, and M. A. Aurybi, "Performance enhancement of solar vortex power generator by Al2O3-in-black paint coating," *J. Clean. Prod.*, vol. 316, p. 128303, Sep. 2021

[92] R. Kumar, S. K. Verma, and M. Singh, "Experimental investigation of black paint coating on absorber for energy conversion applications," *Mater. Today Proc.*, vol. 44, pp. 961–967, 2021

[93] P. M. Yusoff, F. Ahmad, N. Amir, and S. F. Leong, "Effect Of Particle Dispersion On Thermal Conductivity Of Copper Powder Filled Epoxy Composites," *AIP Conf. Proc.*, vol. 1217, no. 1, p. 363, Mar. 2010

[94] M. H. Freeman, C. C. Hull, and W. N. Charman, "The basics of light and optical surfaces," in *Optics*, Elsevier, 2003, pp. 1–24.

[95] I. Renewable Energy Agency, "Renewable power generation costs in 2019," 2020. Accessed: Sep. 05, 2021. [Online]. Available: www.irena.org.

[96] A. Rezania and L. A. Rosendahl, "Feasibility and parametric evaluation of hybrid concentrated photovoltaic-thermoelectric system," *Appl. Energy*, vol. 187, pp. 380–389, Feb. 2017

[97] R. Bjørk and K. K. Nielsen, "The maximum theoretical performance of unconcentrated solar photovoltaic and thermoelectric generator systems," *Energy*

Convers. Manag., vol. 156, pp. 264–268, Jan. 2018

[98] F. Attivissimo, A. Di Nisio, A. M. L. Lanzolla, and M. Paul, "Feasibility of a Photovoltaic–Thermoelectric Generator: Performance Analysis and Simulation Results," *IEEE Trans. Instrum. Meas.*, vol. 64, no. 5, pp. 1158–1169, May 2015,

[99] A. Rezania, D. Sera, and L. A. Rosendahl, "Coupled thermal model of photovoltaic-thermoelectric hybrid panel for sample cities in Europe," *Renew. Energy*, vol. 99, pp. 127–135, Dec. 2016

[100] Asociación Española de Normalización, "UNE-EN IEC 61853-3:2018," 2018.

ANNEXES

ANNEX I Datasheet of the TE modules

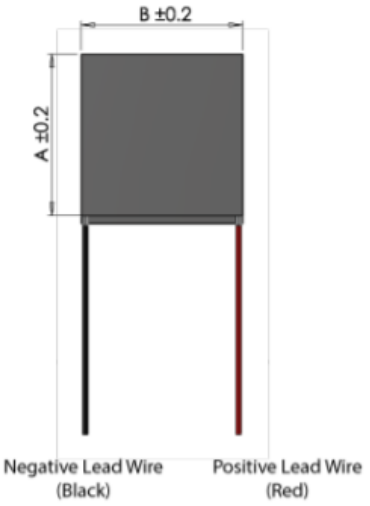

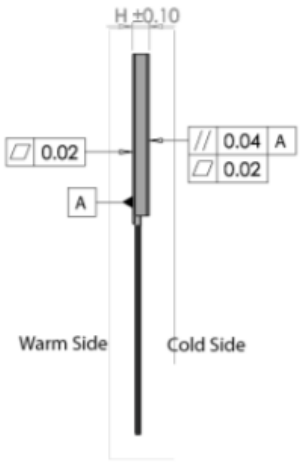

Model GM200-49-45-25

Parameters correct at temp.	Hot side: 250°C Cold side: 30°C	Hot side: 100°C Cold side: 30°C
Matched load output power	0.42W	0.05W
Matched load resistance	1.0Ω ± 15%	0.8Ω ± 15%
Open circuit voltage	1.4V	0.4V
Matched load output	0.6A	0.3A
Matched load output voltage	0.7V	0.2V
Heat flow through module	8W	2.5W
Maximum compress (non-destructive)		1MPa
Maximum operation temperature	Hot side - 250°C. Cold side - 175°C	

Geometric dimensions:

A	62mm
B	62mm
H	5.2mm

Model MGM250-17-10-16

Parameters for hot side temp 200°C and cold side temp 30°C

Matched load output power	9.1W
Matched load resistance	0.22Ω ± 15%
Open circuit voltage	2.8V
Matched load output	6.4A
Matched load output voltage	1.4V
Heat flow through module	~181W
Maximum compress (non-destructive)	1MPa
Maximum operation temperature	Hot side - 200°C. Cold side - 175°C

Geometric dimensions:

A	11.2mm
B	11.2mm
H	3.8mm

ANNEX II Characteristics of the Fresnel lenses

	FRP232	FRP251
Focal Length	*32 mm*	*51mm*
Focal Length Tolerance	*±5%*	*±5%*
Diameter	*2" (50.8 mm)*	*2" (50.8 mm)*
Diameter Tolerance	*±0.125 mm*	*±0.125 mm*
Thickness	*1.5 mm (Nominal)*	*1.5 mm (Nominal)*
Thickness Tolerance	*±0.25 mm*	*±0.25 mm*
Clear Aperture	*>90% of Diameter*	*>90% of Diameter*
Groove Spacing	*0.2 mm*	*0.33 mm*
Pitch	*10°*	*10°*
Design Wavelength	*588 nm*	*588 nm*
Refractive Index	*1.49*	*1.49*
Abbe Number (V_D)	*55.3*	*55.3*
Parallelism	*<3 arcmin*	*<3 arcmin*
Surface Quality	*80-50 Scratch-Dig*	*80-50 Scratch-Dig*
Substrate Material	*Optical-Grade Acrylic*	*Optical-Grade Acrylic*

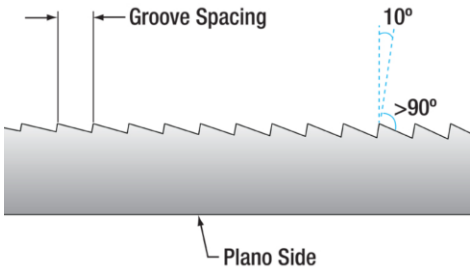

ANNEX III Developed TEG Calculator – MATLAB code

```
classdef app_tec_calc < matlab.apps.AppBase

    % Properties that correspond to app components
    properties (Access = public)[...]
    end
    properties (Access = private)
            res = 30;   %resolution of the measurement
            Tc = 298;
            aux = 125;
            Th = 298:125/30:(423);
    end
% Callbacks that handle component events
    methods (Access = private)

    % Button pushed function: CalculateButton
    function CalculateButtonPushed(app, event)
        DTmax = app.DTmaxKEditField.Value;
        if DTmax < app.aux
           app.Th = app.Tc:app.aux/app.res:(DTmax-app.Tc);
        end
        len = length(app.Th);
        app.GraphValueSlider.Limits= [app.Tc app.Th(end)];
        app.GraphValueSlider.MajorTicks =app.Tc:app.aux/app.res:app.Th(end);
%             app.GraphValueSlider.MajorTickLabels = [];

        %----PEG Model Parameters
        option = app.ListofPEGDropDown.Value;
        if strcmp(option,'MGM250-17-10-16')
          R = 0.8;  %Match Load condition
          a_n1=0.0000334545;    a_n2=-0.023350303;  a_n3=5.606333;
          a_p1=0.0000361558;    a_p2=-0.026351342;  a_p3=6.22162;
          k_n1=0.001530736;     k_n2=-1.08058874;   k_n3=-28.338095;
          k_p1=-0.003638095;    k_p2=2.74380952;    k_p3=-296.214286;
          o_n1=0.01057143;      o_n2=-10.16048;     o_n3=3113.71429;
          o_p1=0.015601732;     o_p2=-15.708052;    o_p3=4466.38095;
        elseif strcmp(option,'GM200-127-28-12')%Pendiente de actualizar
          a_n1=0.0000334545;    a_n2=-0.023350303;  a_n3=5.606333;
          a_p1=0.0000361558;    a_p2=-0.026351342;  a_p3=6.22162;
          k_n1=0.001530736;     k_n2=-1.08058874;   k_n3=-28.338095;
          k_p1=-0.003638095;    k_p2=2.74380952;    k_p3=-296.214286;
          o_n1=0.01057143;      o_n2=-10.16048;     o_n3=3113.71429;
          o_p1=0.015601732;     o_p2=-15.708052;    o_p3=4466.38095;
        elseif strcmp(option,'GM200-49-45-25')%Pendiente de actualizar
          R=9.1;
          a_n1=0.001530736;     a_n2=-1.08058874;   a_n3=-28.338095;
          a_p1=-0.003638095;    a_p2=2.74380952;    a_p3=-296.214286;
          k_n1=0.0000334545;    k_n2=-0.023350303;  k_n3=5.606333;
          k_p1=0.0000361558;    k_p2=-0.026351342;  k_p3=6.22162;
          o_n1=0.01057143;      o_n2=-10.16048;     o_n3=3113.71429;
          o_p1=0.015601732;     o_p2=-15.708052;    o_p3=4466.38095;
```

```
133
134         else
135 %             R =
136           a_n1=app.EditField.Value;     a_n2=app.EditField_2.Value;      ...
                 a_n3=app.EditField_3.Value;
137           a_p1=app.EditField_4.Value;   a_p2=app.EditField_5.Value;     ...
                 a_p3=app.EditField_6.Value;
138           k_n1=app.EditField_13.Value;  k_n2=app.EditField_14.Value;    ...
                 k_n3=app.EditField_15.Value;
139           k_p1=app.EditField_16.Value;  k_p2=app.EditField_17.Value;    ...
                 k_p3=app.EditField_18.Value;
140           o_n1=app.EditField_7.Value;   o_n2=app.EditField_8.Value;     ...
                 o_n3=app.EditField_9.Value;
141           o_p1=app.EditField_10.Value;  o_p2=app.EditField_11.Value;    ...
                 o_p3=app.EditField_12.Value;
142         end
143
144         for i = 1:len
145             %Seebeck
146             a_n(i) = abs((a_n1*app.Th(i)^2+a_n2*app.Th(i)+a_n3)*10^-6);
147             a_p(i) = (a_p1*app.Th(i)^2+a_p2*app.Th(i)+a_p3)*10^-6;
148             seebeck(i) = a_p(i) ;
149
150             %Thermal Conductivity
151             k_n(i) = (k_n1*app.Th(i)^2+k_n2*app.Th(i)+k_n3);
152             k_p(i) = (k_p1*app.Th(i)^2+k_p2*app.Th(i)+k_p3);
153             th_cond(i) = k_p(i) ;
154
155             %Electrical Conductivity
156             o_n(i) = (o_n1*app.Th(i)^2+o_n2*app.Th(i)+o_n3)*10^2;
157             o_p(i) = (o_p1*app.Th(i)^2+o_p2*app.Th(i)+o_p3)*10^2;
158             el_cond(i) = o_p(i) ;
159
160         %----------Electrical performance of the TEG
161         r_var = 0:10/(len-1):10;%to check the efficiency dependence on ...
                load ratio
162         for i = 1:1:app.Th
163             %----------Load Ratio load_r = RL/R
164             load_r(i) = ...
                    sqrt(1+(el_cond*seebeck(i)^2/th_cond)*(app.Th(end)+app.Tc)/2);
165             %--Figure of merit
166             app.Z(i) = el_cond(i)*seebeck(i)^2/th_cond(i);
167             app.Z_Tmean(i) = app.Z(i)*(app.Th(end)+app.Tc)/2;
168             app.ZTh(i) = 2*app.Z_Tmean(i)*(1 + app.Tc/app.Th(end))^-1; ...
                              %(8)
169             %Internal resistence
170             app.Ri(i) = app.n * (( integral(app.rhon, (app.Tc(i)), ...
                    (app.Th(i)))./app.DTmax) * (app.h/app.An) ...
171             + ( integral(app.rhop, (app.Th(i)), ...
                    (app.Th(i)))./app.DTmax(i)) * (app.h/app.Ap)) ...
172             + app.n*2*app.rcn/app.An + app.n*2*app.rcp/app.Ap + ...
                    app.n*app.rhoEl*app.L1El/app.AEl1 ...
173             + ...
                    (app.n/2)*(app.rhoEl*app.L1El/app.AEl1)*(app.DRR*(app.Th2(i)))
                    + ...
                    (app.n/2)*(app.rhoEl*app.L1El/app.AEl1)*(app.DRR*(app.Tc2(i)));
174             %Open-circuit voltage
175             app.Vopen(i) = app.n * integral(app.apn, (app.Tc(i)), ...
                    (app.Th(i)))   ;
176             %Output maximum current
177             app.Imax(i) = app.Vopen(i)/(2*app.Ri(i));
178             %Maximum output power
179             app.Pmax(i) = (seebeck(i)*(app.Th(i)-app.Tc))^2/4/R;
```

```
180             %--efficiency
181             app.eff(i) = r_var(i)*(1-app.Tc/app.Th(end))/(1+r_var(i) ...
                   -(1-app.Tc/app.Th(end))/2 + (1+app.Tc/app.Th(end))*(1 + ...
                   r_var(i))^2/2/app.Z_Tmean(i));
182             app.eff(i) = 100*app.eff(i);
183             %app.eff = ( app.Pmax )./( app.Qcold +app.Pmax )*100;
184             app.check = 'Cycle end';
185             display(app.check);
186         end
187         %-- Graphs
188         function PEGplot[...]
224         end
225         %----PEG Model Parameters plot
226         function paramplot
238         end
239     end
240
241         %---------------------------------------
242     % Component initialization
243     methods (Access = private)
244
245         % Create UIFigure and components
246         function createComponents(app)[...]
341         end
342     end
343
344     % App creation and deletion
345     methods (Access = public)[...]
367     end
368 end
```

ANNEX IV Concentrating 11.2x11.2 TEG design plan

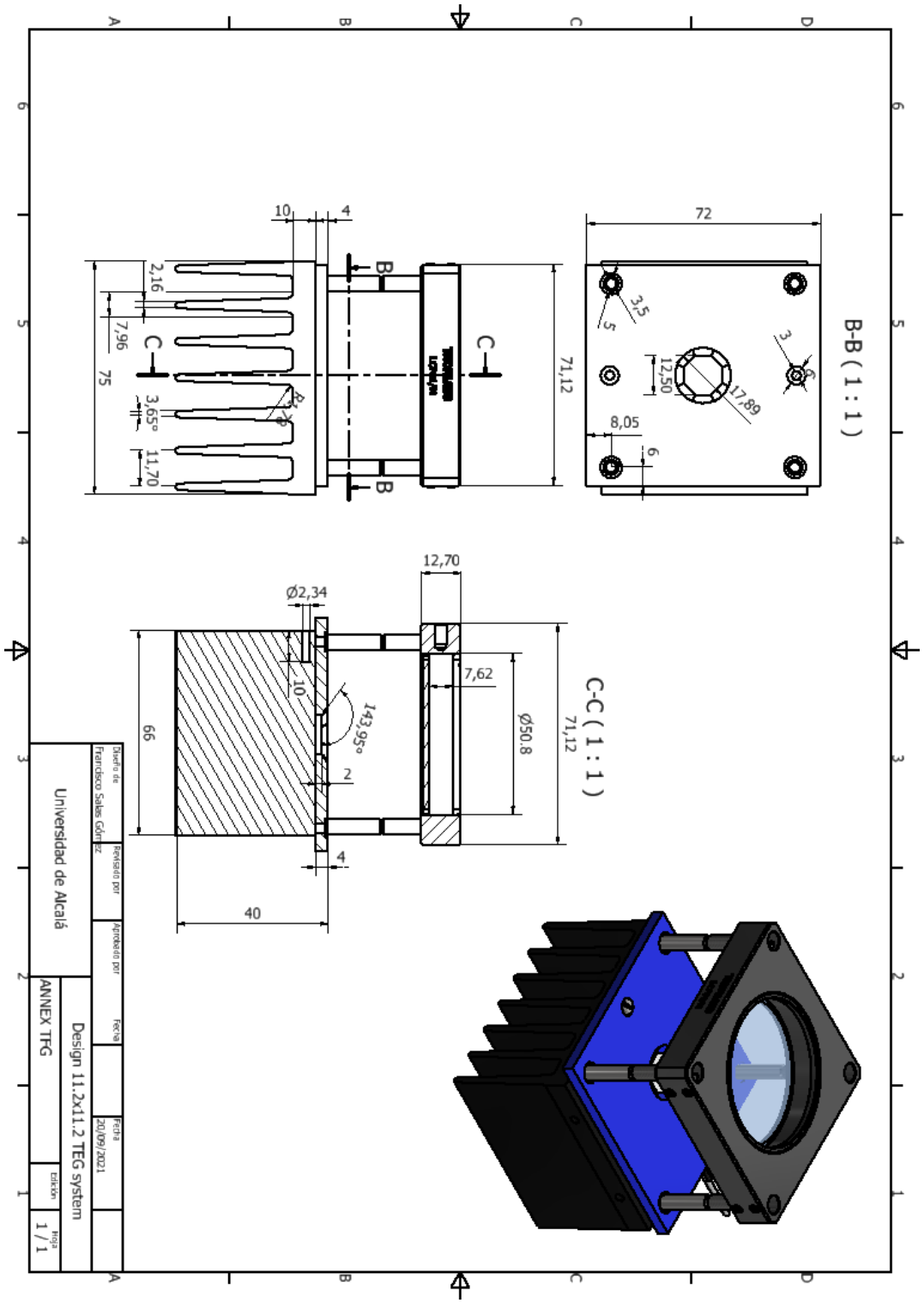

ANNEX V STMicroelectronics Evaluation Board – modified Schematic

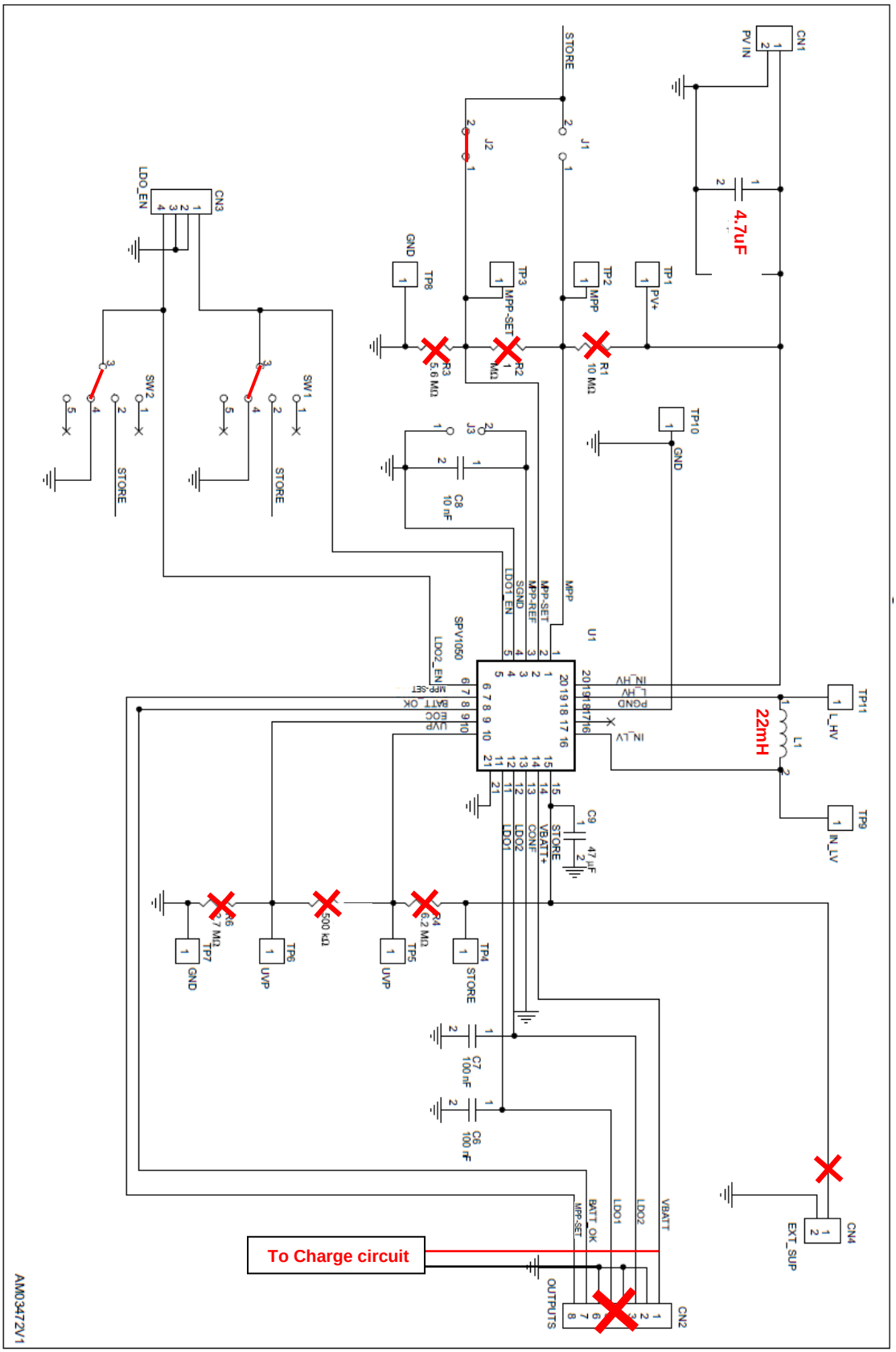

ANNEX VI Charge stage schematic

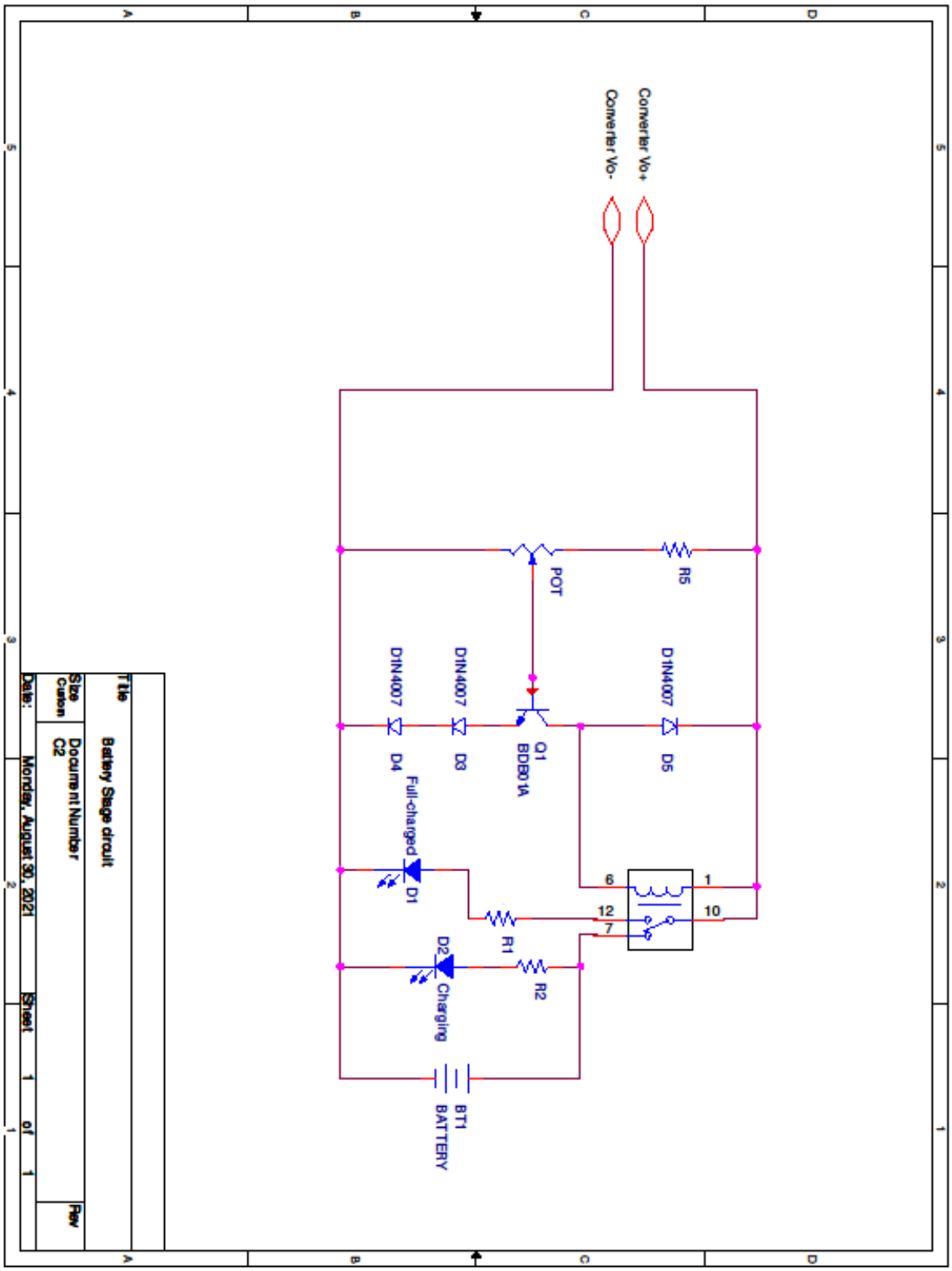

ANNEX VII Curve Fitting with MATLAB

This report works with the third-degree polynomial fitting model:

```
f(x) = p1*x^3 + p2*x^2 + p3*x + p4
```

Curve Fitting Toolbox software by MATLAB is based on these goodness-of-fit statistics for parametric models: The sum of squares due to error (SSE), R-square (SSR), Adjusted R-square, and Root mean squared error (RMSE).

LAR robust regression has been implemented to the all the models due to the fact that the measurements contain a number of outliners.

Least absolute residuals (LAR)

The LAR method finds a curve that minimizes the absolute difference of the residuals, rather than the squared differences. Therefore, extreme values have a lesser influence on the fit.

Bisquare weights

This method minimizes a weighted sum of squares, where the weight given to each data point depends on how far the point is from the fitted line. Points near the line get full weight. Points farther from the line get reduced weight. Points that are farther from the line than would be expected by random chance get zero weight.

Fitting example

Table A. 1 draws a comparison between two regression methods, and the effect of no applying the robust solution.

		Without robust regression	With robust regression solution:	
			LAR method	Bisquare Method
Goodness of fit:	SSE	0.1181	**0.001932**	0.06827
	R-square	0.962	**0.9994**	0.978
	Adjusted R-square:	0.9618	**0 .9994**	0.9779
	RMSE	0.01102	**0.001409**	0.008377

Table A. 1 Goodness of the fit comparison - example

Figure A. 1 corresponds to the output voltage measurement of the fan-cooled test. It can be noticed that there is a number of outliers that have an impact on the curve.

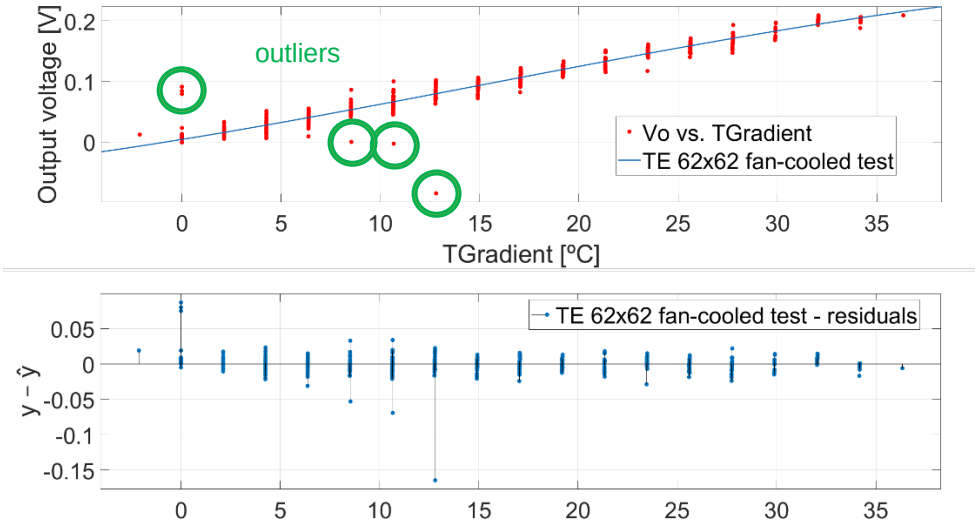

Figure A. 1 LAR method curve – example for the developed lab test

ANNEX VIII Sun path and solar irradiation

The sun path estimations needed for the outdoor tests were obtained from Suncalc.org [88]. This website uses the registered data from the European Centre for Weather Forecasts (ECWF). The irradiance estimations needed for the outdoor tests were obtained from the Photovoltaic geographical information system of European Commission's Joint Research Centre (JRC) [84].

Solar data for 40°30'48.2"N 3°20'43.4"W (Alcalá de Henares, Spain)			
Dawn:	**06:23:32**	**Sunset:**	**21:43:01**
Sunrise:	**06:55:22**	**Dusk:**	**22:14:46**
Culmination:	**14:19:24**	Daylight duration:	**14h47m39s**

Table A. 2 SunCalc.org – Solar data in July at the working location

Figure A. 2 SunCalc.org - Sun path for July 2021 in Alcalá de Henares

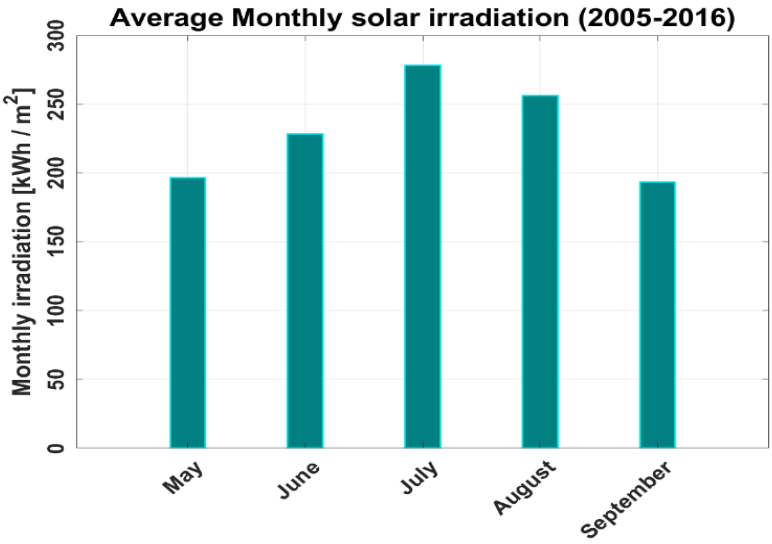

Figure A. 3 Average monthly solar irradiation (2005-2016)

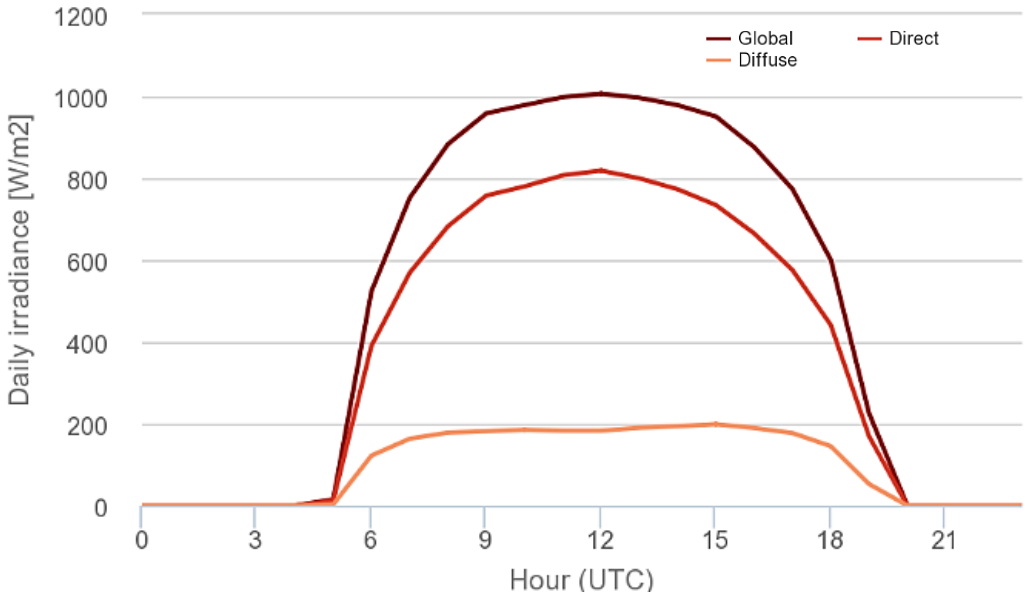

Figure 4.23 Daily irradiance profile for a 2-axis tracking in July at Alcalá de Henares (source PVGIS)

ANNEX IX Gant chart of the project

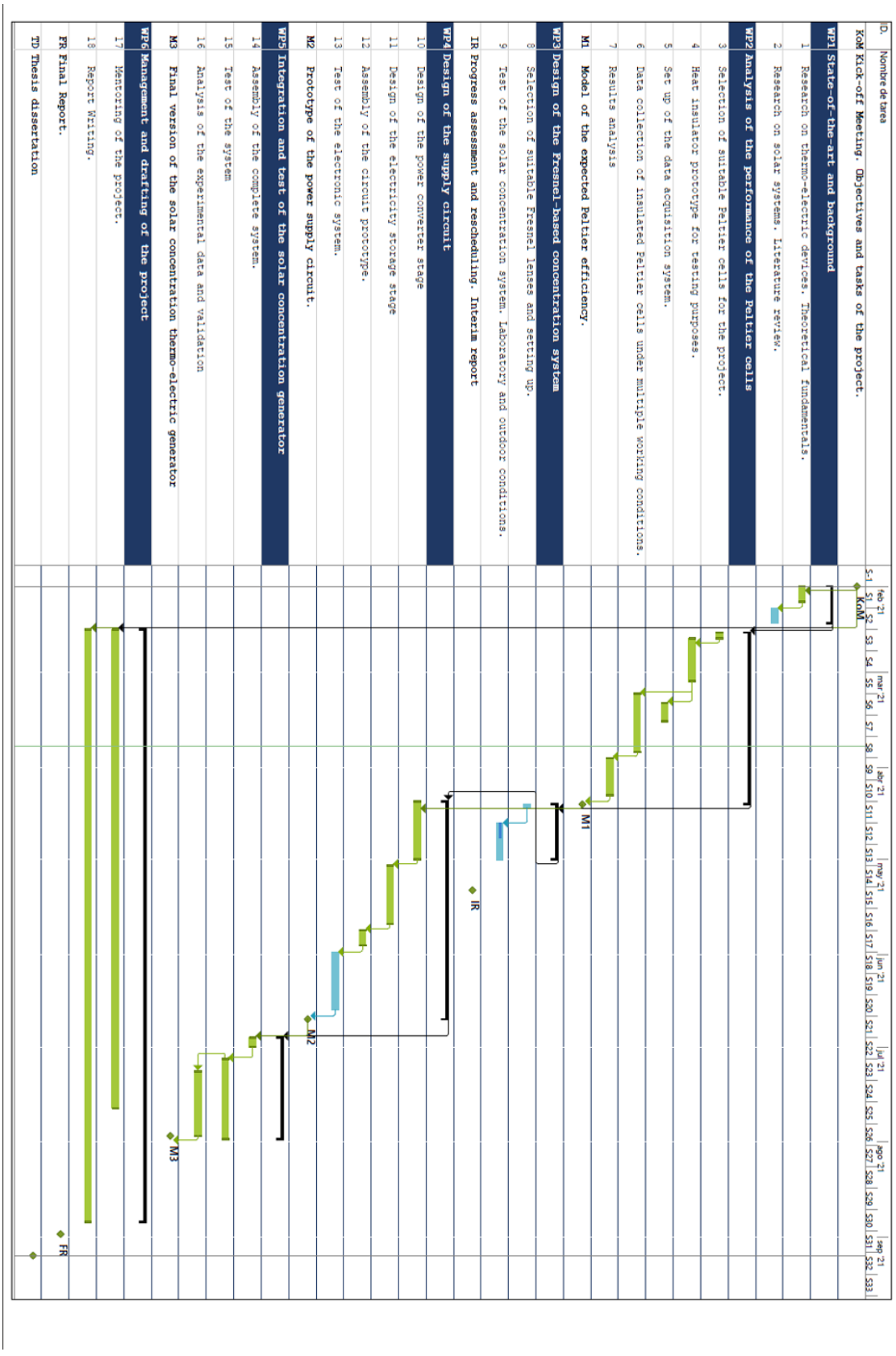

Universidad de Alcalá
Polytechnic School

Universidad de Alcalá